Image analysis in optical coherence tomography
Retinal layer segmentation

Novosel, Jelena

DOI
10.4233/uuid:067f2d6d-9391-403f-ae8c-11389f160d95

Publication date
2017

Document Version
Final published version

Citation (APA)
Novosel, J. (2017). *Image analysis in optical coherence tomography: Retinal layer segmentation*. [Dissertation (TU Delft), Delft University of Technology]. https://doi.org/10.4233/uuid:067f2d6d-9391-403f-ae8c-11389f160d95

Image analysis in optical coherence tomography

Retinal layer segmentation

Image analysis in optical coherence tomography

Retinal layer segmentation

Proefschrift

ter verkrijging van de graad van doctor
aan de Technische Universiteit Delft,
op gezag van de Rector Magnificus prof. ir. K.C.A.M. Luyben,
voorzitter van het College voor Promoties,
in het openbaar te verdedigen op
maandag 6 maart 2017 om 15:00 uur

door

Jelena NOVOSEL

Master of Science in Information and Communication Technology,
University of Zagreb, Zagreb, Croatia,
geboren te Zagreb, Kroatië.

Dit proefschrift is goedgekeurd door de

promotor: prof. dr. ir. L.J. van Vliet
copromotor: dr. ir. K.A. Vermeer

Samenstelling promotiecommissie:

Rector Magnificus,	voorzitter
Prof. dr. ir. L.J. van Vliet,	Technische Universiteit Delft, promotor
Dr. ir. K.A. Vermeer,	Rotterdam Opthmalmic Institute, copromotor
Onafhankelijke leden:	
Prof. dr. C.C.W. Klaver,	Erasmus Medisch Centrum
Prof. dr. W.J. Niessen,	Erasmus Medisch Centrum
Prof. dr. ir. N. de Jong,	Technische Universiteit Delft
Dr. C. I. Sánchez,	Radboud Universiteit Nijmegen
Prof. dr. A.M. Vossepoel,	Technische Universiteit Delft / Erasmus Medisch Centrum, reservelid
Overige leden:	
Dr. H. G. Lemij,	Oogziekenhuis Rotterdam

Printed by: PrintSupport4U

Front & Back: Bruno Arsenali

Financial support: ZonMw (grant number: 91212061), Stichting Combined Ophthalmic Research Rotterdam, Stichting Glaucoomfonds and Stichting voor Ooglijders.

Printing of this thesis was supported by De Landelijke Stichting voor Blinden en Slechtzienden (LBLS).

ISBN: 978-94-9259-701-4

Posvećeno mojim roditeljima

Contents

1

Introduction

How do we explain the world around us? Two wise men started the search for an answer thousands of years ago and became two of the most influential philosophers. Their debate still remains with us today. Plato believed true knowledge comes from the mind, which is rational, and not from the senses, which can be fooled. In contrast, Aristotle believed the senses allow us to learn and interact with the world around us. Despite this ongoing debate, we use our senses to experience the world around us. Of all our senses, the sense of sight contributes the most to our awareness. From the moment we wake up until the time we go to sleep; we use our sense of sight in almost everything we do. However, nowadays, 285 million people worldwide experience problems with visual perception and are either blind or have an impaired visual function [1]. This significantly influences their quality of life and creates problems in their daily activities. The number of people with visual problems is expected to grow even further as the population is ageing and many eye diseases are age related [2]. Furthermore, various eye diseases cause around 80 % of the existing visual impairment [1]. Many of them can be prevented, slowed down or cured by applying existing knowledge and technology [1, 2]. Hence, efficient ways to prevent, diagnose or cure eye diseases are required. This includes both the examination of the retina and the extraction of imaging biomarkers for disease diagnosis, prognosis and/or monitoring.

1.1. Human eye

Known as the most complex organ after the brain, our eyes are responsible for receiving 80 % of the information from the surrounding world that reaches us [3]. With only 2.5 cm in diameter and more than two million operational parts, the eyes allow us to sense shapes, colors, and dimensions of objects in the world around us. However, this would not be possible without light. To be able to see anything, the eyes first need to collect, focus and process light. Light is reflected from an object, moves through space and reaches our eyes. The light that enters the eye is projected onto the back of the eyeball and captured and processed by the retina after which the stimuli are being sent to our brain, which deciphers the information about the appearance, location and movement of the objects we are looking at.

1.2. Formation of an image and the anatomy of the eye

After reaching our eyes, light first passes through the transparent layer of tissue at the front of the eye, the cornea. The cornea is the eye’s main focusing element, responsible for transmitting and refracting the light into the eye. It is located on top of the iris, which with the pupil controls the amount of light that enters the eye. Afterwards, the light passes through another transparent structure, the lens, which focuses the light onto the retina. Before it reaches the retina, the light passes through a dense, transparent gel-like substance, called the vitreous that fills the eyeball and ensures the eye holds its spherical shape. Finally, the light hits the retina, which reacts to the presence and intensity of light by sending impulses to

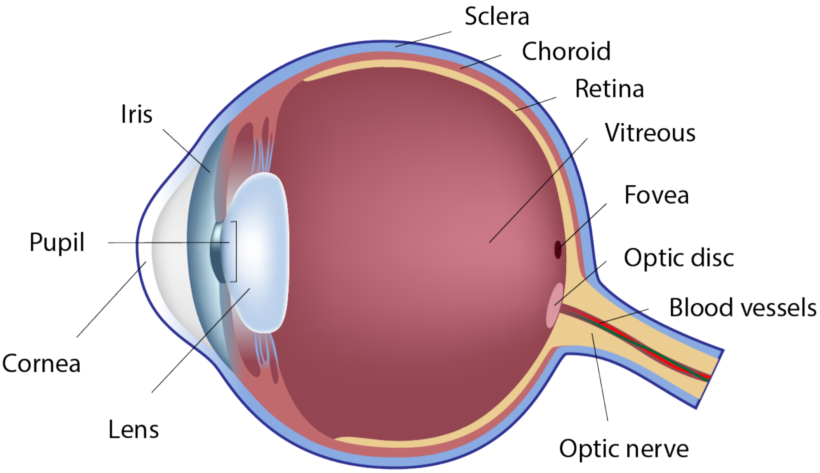

Figure 1.1: An illustration of a cross-section of a human eye with indications of its most important parts.

the brain via the optic nerve (a bundle of more than a million nerve fibers). Within the retina, the macula is the area that contains special light-sensitive cells allowing us to see fine details. Located behind the retina are the choroids, responsible to nourish the retina through the blood vessels, which grow in the choroid. Finally, the white outer coat surrounding the eye is the sclera. A schematic of the cross-section of the eye is shown in Figure 1.1.

1.3. The retina and retinal layers

The retina is a light-sensitive tissue structure located at the back of the eye. The inner (anterior) surface of the retina is adjacent to the vitreous of eye, whereas the outermost parts (superior) of the retina are tightly attached to the choroids. The retina is composed of various types of cells, illustrated in Figure 1.2, which form different layers as follows:

1. *The inner limiting membrane* (*ILM*) is the boundary between the retina and the vitreous.
2. *The retinal nerve fiber layer* (*RNFL*) consists of fibers from ganglion cells, which leave the retina through the optic nerve head.
3. *The ganglion cell layer* (*GCL*) contains the nuclei of the ganglion cells.
4. *The inner plexiform layer* (*IPL*) contains the axons of bipolar cells and amacrine cells and the dendrites of ganglion cells.
5. *The inner nuclear layer* (*INL*) contains the nuclei of horizontal cells, bipolar cells, amacrine cells, and Müller cells.
6. *The outer plexiform layer* (*OPL*) contains cone and rod axons, horizontal cell dendrites and bipolar dendrites.

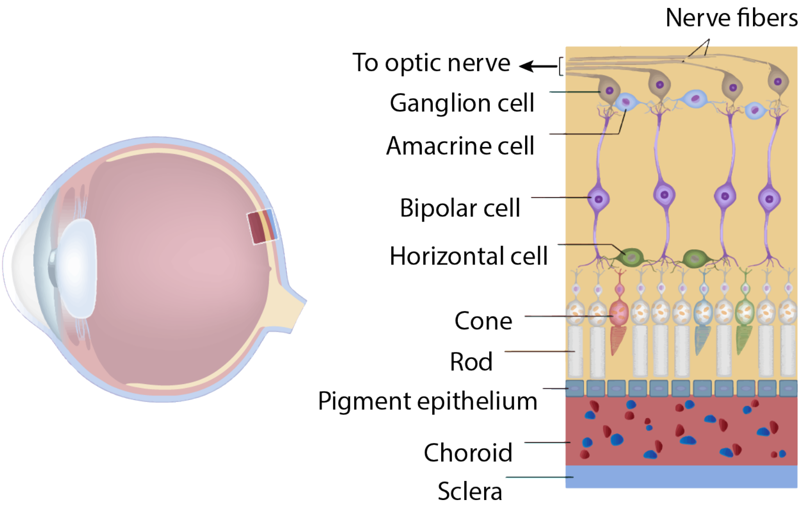

Figure 1.2: An illustration of a cross-section of the retina showing the organization of cells that compose the retinal tissue.

7. *The outer nuclear layer* (*ONL*) contains cell bodies of cones and rods.
8. *The external limiting membrane* (*ELM*) contains clusters of junctional complexes between the Müller cells and the photoreceptors.
9. *The ellipsoid zone* (*EZ*) is mainly formed by mitochondria.
10. *The integration zone* (*IZ*) corresponds to the contact cylinder which are formed from the tips of the RPE cells that encase part of the cone outer segments.
11. *The retinal pigment epithelium* (*RPE*) contains supporting cells for the neural portion of the retina.

1.4. Eye diseases

A healthy eye is essential for good vision. Thus, when vision starts to deteriorate, it is important to examine the eye as well as the retina. With this examination, it can be determined whether the cause of the change in vision is an eye disease because early diagnosis and treatment can help to preserve good vision and prevent vision loss. There are many types of eye diseases, however within this thesis, the focus is only on a few of them: glaucoma, age-related macular degeneration, central serous retinopathy and retinitis pigmentosa.

Glaucoma, known as ”the sneak thief of vision”, is a retinal eye disease which causes irreversible damage to the optic nerve head and is as such one of the leading causes of irreversible blindness in the world [3]. The disease is associated with an increased intra-ocular pressure and develops slowly without noticeable sight loss

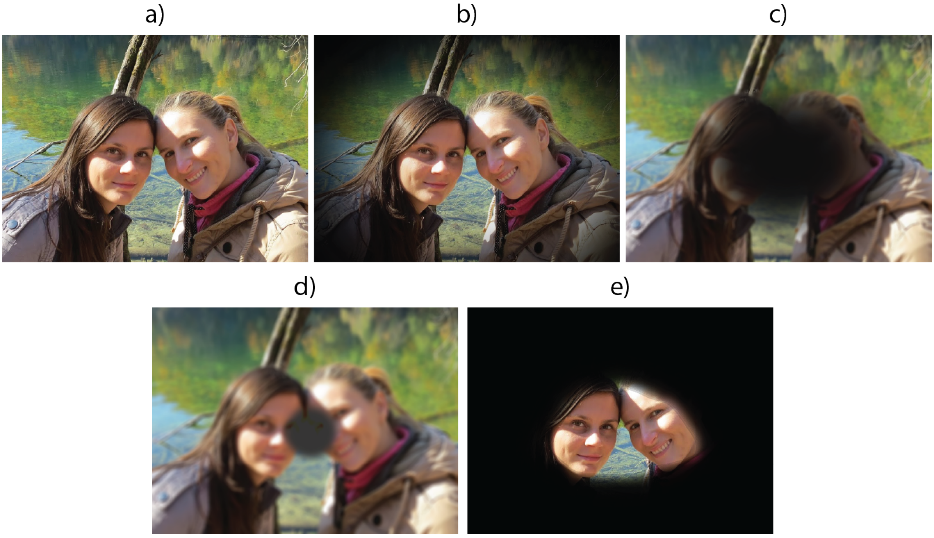

Figure 1.3: Images that simulate the effect that some eye diseases have on vision. a) A scene as viewed by a person without any visual impairment. The same scene as viewed by a patient suffering from glaucoma, AMD, CSR and RP is shown in b), c), d) and e), respectively.

for many years. If diagnosed early, the disease can be controlled and permanent vision loss can be prevented [4].

Age-related macular degeneration (AMD) is among the leading causes of vision loss in people of age 50 and older [3]. It causes damage to the macula, which results in a blurred area near the center of vision. Over time, the blurred area may grow larger or blank spots in the central vision may develop. By itself, it does not lead to complete blindness, however, the loss of central vision can interfere with simple everyday activities.

Central serous retinopathy (CSR) is a disorder causing temporary visual impairment. When active, it is characterized by a build up of fluid around the central macular area which results in blurred or distorted vision. The vast majority of fluid will resolve spontaneously within three to four months and vision usually returns to normal.

Finally, retinitis pigmentosa (RP) refers to a group of genetic disorders that affect the retina's ability to respond to light. The disease is inherited and causes slow vision loss, beginning with decreased night vision and loss of peripheral vision. Eventually, it leads to blindness. There is no cure for retinitis pigmentosa, however, there are treatments that have shown to slow down the disease progression [5].

All aforementioned eye diseases affect the retina in a different manner and, therefore are the cause of different types of vision loss. An example of how vision is affected by each of the mentioned diseases is shown in Figure 1.3. To further investigate the causes of these and other eye disease and their effect on the retina and its layers, an efficient way to examine the retina in vivo is needed.

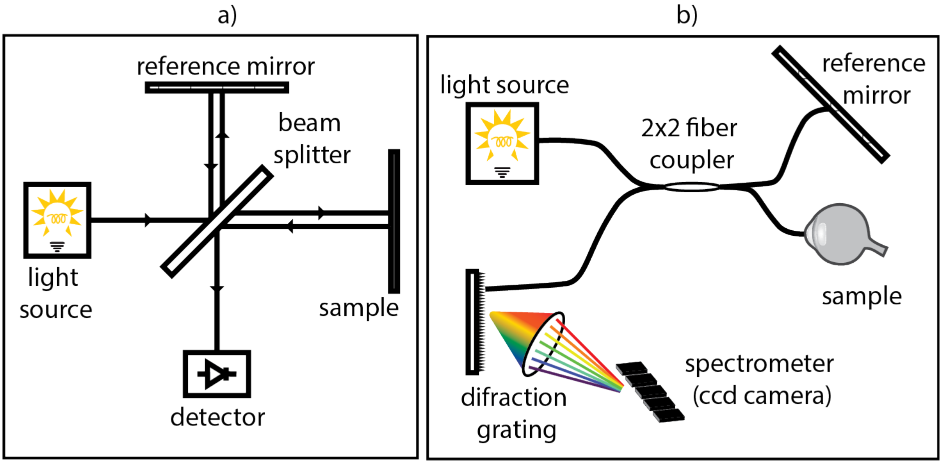

Figure 1.4: a) A schematic of the Michelson interferometer. A single ray of light is split into two rays by a beam splitter. Each of the two rays than travels along a different optical path (one to the reference mirror, the other to the sample). The rays are reflected back to the beam splitter where they are reunited to produce an interference pattern. The interference pattern depends on the difference in the path length of the two rays and will be imaged by the detectors. b) A schematic of the SD-OCT system. The system contains the interferometer, however the interference between the sample and reference beams is detected as a spectrum. The spectrum is spread out a grating and captured by a high-speed line camera. The resulting spectrum is then inverse Fourier transformed to provide a depth scan.

1.5. Optical coherence tomography

With the rapid development of imaging technologies in the last decade, 3D examination of the retina has become possible. By means of an imaging technology called optical coherence tomography (OCT), in vivo images of retinal structures with a high spatial resolution can be produced [6]. OCT operates similarly to ultrasound, but uses light instead of sound. The light of a low coherence light source is split, by a beam splitter, into the two arms of an interferometer: the sample arm and the reference arm. The light of the sample arm enters ones eye and a small fraction is reflected (back-scattered) from the retina. This small amount of the reflected light interferes with the light of the reference arm. The described principle is the basic of an OCT system and is often implemented via Michelson interferometer [7], which is illustrated in Figure 1.4a. In spectral domain OCT (SD-OCT), the length of the reference arm is kept fixed [8, 9]. The light passes through a spectrometer, that can reveal the depth from which the light was reflected. The spectrum is captured by a charge-coupled device (CCD) array and digitized. Dedicated signal processing of the recorded spectrum including a Fourier transform yields the reflected signal as a function of depth in the sample, often referred to as an A-line. Scanning the beam over the retina creates an image that shows the internal detail of the retina, including the retinal layers. The schematic drawing of a SD – OCT system is shown in Figure 1.4b.

In general, OCT provides a technique for fast, non-invasive and non-contact investigation of the retina as well as structural changes that occur as a result of

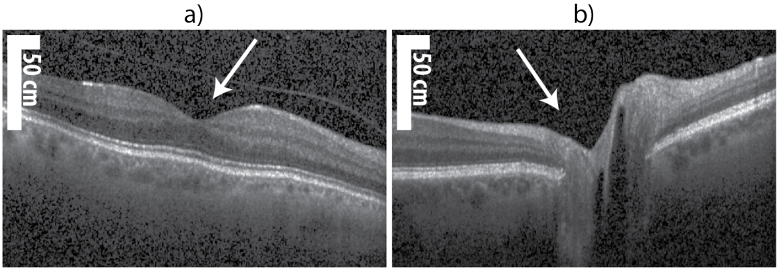

Figure 1.5: Typical example of a macular and peripapillary B-scan from a healthy subject is shown in a) and b), respectively. Arrows point to the fovea (center of the eye's sharpest vision) in the macular scan and optic disc (blind spot) in the peripapillary scan.

retinal diseases. Example of a slice (B-Scan) from the 3D volume of the macular (around the macula) and peripapillary (around the optic nerve head) region of the retina are shown in Figure 1.5.

1.6. Challenges for automatic segmentation of retinal structures

Accurate quantification of retinal structures in 3D scans as acquired with OCT systems provides clinically useful information about the retina. It enables valuable input for the diagnostics, prognostics and monitoring of retinal diseases. Extraction of quantitative image-based features that provide relevant biological information, referred to as imaging biomarkers, can also be performed. However, manual extraction of these imaging biomarkers is a potentially subjective and time-consuming job due to the required precision and large data size. Hence, an objective and automatic tool that extracts clinically useful information from OCT images, such as the thickness of layers or the presence and extent of emerging pathologies, is needed.

However, automatic segmentation of the retinal layers and pathologies remains a challenging task. First, OCT images suffer from speckle noise [10], which decreases the quality of an image and limits the contrast and thus complicates precise identification of boundaries of retinal layer. Second, thin layers in the outer retina are difficult to detect as their size is on the order of the axial resolution and their contrast can be similar to that of the noise [11]. Third, a single tissue layer, which is often considered as a homogeneous region, shows large intensity fluctuations. This is partially due to the decrease in sensitivity of the OCT system as a function of depth, which causes the intensity of a (tilted) homogeneous tissue layer to decrease with depth [12]. Further, abrupt intra-layer intensity variations can also be caused by a disease [13]. Fourth, the blood vessels in the anterior retina absorb a large amount of the incoming light and thereby cast a shadow onto the posterior layers. This creates large lateral discontinuities in signal intensity of these layers, which hamper an automatic segmentation task. Finally, large disruptions of the retina, called lesions, might occur as a result of a disease. This can affect both the topology and morphology of the retina. Further, lesion segmentation can be

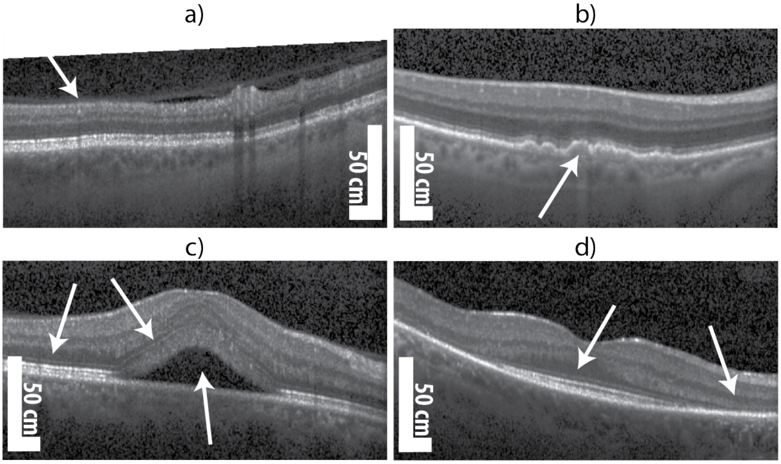

Figure 1.6: Typical examples of B-scans from diseased eyes with arrows pointing to some of the segmentation challenges present in these eyes. In glaucoma affected eye, shown in a), arrows point to the *RNFL*, whose thickness is reduced when compared to healthy eyes. In scan of patients suffering from AMD, shown in b), lesion called drusen appear underneath the retina, as indicated by the arrow. In OCT scans of eyes affected by CSR, shown in c), arrows point to areas which change in intensity as well as presence of fluid pockets. Finally, scans of eyes affected by RP, shown in d), reveal that several outer retinal layers are no longer visible. Arrows point to area where the visibility of retinal layers varies.

challenging as lesions can vary considerably in size, shape and location. Figure 1.6 shows examples of a typical B-scan of eyes affected by glaucoma, age-related macular degeneration, central-serous retinopathy and retinitis pigmentosa in which some of the segmentation challenges are indicated.

1.7. Attenuation coefficient

Image contrast in OCT images originates from variations in reflectivity of different structures. As many eye diseases are accompanied with cellular changes in the tissue, this is bound to induce changes to the reflectivity properties of the corresponding tissue. One example of this is glaucoma, a retinal disease characterized by the loss of ganglion cells and their axons (situated within the *RNFL*) [14]. As a results of this cell loss, the internal reflectivity of the *RNFL* was shown to be reduced in eyes affected by glaucoma when compared to healthy eyes [15]. However, interpretation of OCT signals is not straightforward as it depends on many other factors, such as the strength of the light beam and the scattering properties of tissue that light passes through before reaching a certain depth.

Hence, attenuation coefficients were proposed as a means to characterize the optical scattering properties of the tissue [16]. As a tissue property, attenuation coefficients are illumination invariant and many imaging artefacts are reduced. As such, the investigation of attenuation coefficient is more reliable that the raw OCT signal. The reduction in imaging artefacts can be observed from Figure 1.7 where

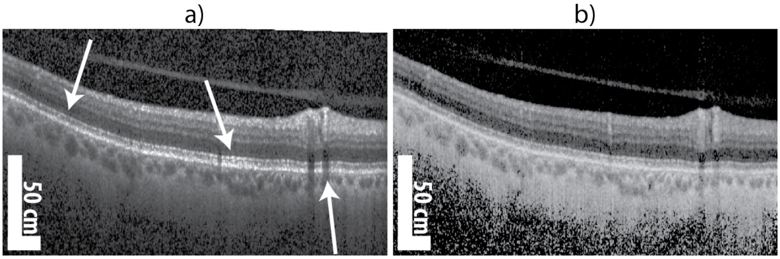

Figure 1.7: An example of the raw OCT B-scan (a)) and the corresponding attenuation coefficient image (b)). Arrows point some of the imaging artefacts that are present in the OCT data, variance in intensity of the *RPE* and gaps caused by blood vessels.

both a raw OCT and its attenuation coefficient image are shown.

The conversion of the raw OCT data to attenuation coefficients is based on the principle behind Beer-Lambert's law. This law relates the attenuation of light to the properties of the medium through which the light is travelling as follows:

$$L = L_0 e^{-A} \tag{1.1}$$

where A are the optical properties of the medium, L_0 and L are the power of light before and after traveling through a certain medium, respectively. In OCT, the light passes through the tissue, interacts with it and is reflected from a certain depth. This attenuated and back-reflected signal is picked-up by the systems' detector. Thus, by using Beer-Lambert's law under assumptions that almost all light is attenuated within the imaging depth of the OCT system and that the fixed fraction of the attenuated light is reflected back towards the OCT system's detectors, the detected OCT signal can be written as:

$$I(z) = \alpha\beta\mu(z)I_0 e^{-2\int_0^z \mu(u)\mathrm{d}u} \tag{1.2}$$

where α represent a fraction of attenuated light that is back scattered from a certain depth z, β is a conversion factor that accounts for the digitization of the signal, $\mu(z)$ is depth-dependent attenuation coefficient and I_0 is the irradiance of the incident light beam at depth $z = 0$ [15].

1.8. Thesis outline

The research project, described in this thesis, took place as part of a collaboration between Delft University of Technology and Rotterdam Ophthalmic Institute. The goal of the project was to develop an automatic segmentation framework for retinal layers and lesions in 3D peripapillary and macular SD-OCT scans, which allows extraction of clinically useful imaging biomarkers, such as the presence, thickness or attenuation coefficient of a certain layer and the presence and spatial extent of lesions.

Chapter 2 addresses retinal layer segmentation by introducing a loosely coupled level set framework. The framework operates on 3D OCT volumes after conversion into attenuation coefficients. All interfaces between retinal layers are segmented simultaneously by utilizing image data and anatomical knowledge about the retina. The performance of the method was evaluated on peripapillary and macular SD-OCT scans of healthy subjects and glaucoma patients by comparing manual annotations and results obtained from the automatic segmentation method.

Chapter 3 presents an extension of our original loosely coupled level sets framework to eyes suffering from two topology-disrupting retinal diseases: CSR and AMD. The main contributions are the introduction of auxiliary interfaces for pathologies, the ability to cope with abrupt local intensity variation within layers and robust initialization of the level sets. The approach was evaluated on eyes affected by CSR and AMD.

Chapter 4 presents a method for the segmentation of the outer retinal layers, which simultaneously determines the number of visible layers and segments them. The method is based on a model selection approach that balances the goodness of fit with the model complexity of competing models. The accuracy and reproducibility of the method were evaluated on healthy eyes, as well as its ability to segment eyes affected by RP.

Chapter 5 presents a clinical application of the method presented in **Chapter 2**. The presented method was utilized for a volume segmentation of the *RNFL*, after which attenuation and thickness maps of the *RNFL* were created. Afterwards, the correlation between local glaucomatous damage in both *RNFL* attenuation coefficients and *RNFL* thickness maps and areas of decreased retinal sensitivity in visual field maps was visually determined.

Chapter 6 presents the conclusion and outlook.

References

[1] S. West and A. Sommer, *Prevention of blindness and priorities for the future,* Bulletin of the World Health Organization **79**, 244 (2001).

[2] D. Pascolini and S. P. Mariotti, *Global estimates of visual impairment: 2010,* British Journal of Ophthalmology **96**, 614 (2012).

[3] J. Sardegna, S. Shelly, and S. Steidl, *The Encyclopedia of Blindness and Vision Impairment*, Facts on File Library of Health & Living (Facts On File, Incorporated, 2002).

[4] H. Neal, *Low Vision* (Touchstone, 1990).

[5] E. L. Berson, B. Rosner, M. A. Sandberg, K. C. Hayes, C. Weigel-DiFranco, and W. Willett, *A randomized trial of vitamin a and vitamin e supplementation for retinitis pigmentosa,* Archives of Ophthalmology **111**, 761 (1993).

[6] D. Huang, E. A. Swanson, C. P. Lin, J. S. Schuman, W. G. Stinson, W. Chang, M. R. Hee, T. Flotte, K. Gregory, and C. A. e. a. Puliafito, *Optical coherence tomography,* Science **254**, 1178 (1991).

[7] A. A. Michelson and E. W. Morley, *On the relative motion of the earth and the luminiferous ether,* American Journal of Science **34**, 333 (1887).

[8] G. Hausler and M. W. Lindner, *Coherence radar and spectral radar — new tools for dermatological diagnosis,* Journal of Biomedical Optics **3**, 21 (1998).

[9] T. Mitsui, *Dynamic range of optical reflectometry with spectral interferometry,* Japanese Journal of Applied Physics **38**, 6133 (1999).

[10] J. M. Schmitt, S. H. Xiang, and K. M. Yung, *Speckle in optical coherence tomography,* Journal of Biomedical Optics **4**, 95 (1999).

[11] R. F. Spaide and C. A. Curcio, *Anatomical correlates to the bands seen in the outer retina by optical coherence tomography: Literature review and model,* Retina **31**, 1609 (2011).

[12] B. Potsaid, I. Gorczynska, V. J. Srinivasan, Y. Chen, J. Jiang, A. Cable, and J. G. Fujimoto, *Ultrahigh speed spectral / fourier domain OCT ophthalmic imaging at 70,000 to 312,500 axial scans per second,* Optics Express **16**, 15149 (2008).

[13] C. Ahlers, W. Geitzenauer, G. Stock, I. Golbaz, U. Schmidt-Erfurth, and C. Prünte, *Alterations of intraretinal layers in acute central serous chorioretinopathy,* Acta Ophthalmologica **87**, 511 (2009).

[14] R. Susanna, *The Optic Nerve in Glaucoma* (Cultura Medica, 2005).

[15] M. E. Pons, H. Ishikawa, R. Gurses-Ozden, J. M. Liebmann, H. Dou, and R. Ritch, *Assessment of retinal nerve fiber layer internal reflectivity in eyes with and without glaucoma using optical coherence tomography,* Archives of Ophthalmology **118**, 1044 (2000).

[16] K. A. Vermeer, J. Mo, J. J. A. Weda, H. G. Lemij, and J. F. de Boer, *Depth-resolved model-based reconstruction of attenuation coefficients in optical coherence tomography,* Biomedical Optics Express **5**, 322 (2014).

2

Loosely coupled level sets for simultaneous 3D retinal layer segmentation in optical coherence tomography

This chapter is based on the manuscript:

J. Novosel, G. Thepass, H. G. Lemij, J. F. de Boer, K. A. Vermeer and Lucas J. van Vliet, *Loosely coupled level sets for simultaneous 3D retinal layer segmentation in optical coherence tomography*, Medical Image Analysis **26**, 1 (2015)

Abstract

Optical coherence tomography (OCT) yields high-resolution, three-dimensional images of the retina. Reliable segmentation of the retinal layers is necessary for the extraction of clinically useful information. We present a novel segmentation method that operates on attenuation coefficients and incorporates anatomical knowledge about the retina. The attenuation coefficients are derived from in-vivo human retinal OCT data and represent an optical property of the tissue. Then, the layers in the retina are simultaneously segmented via a new flexible coupling approach that exploits the predefined order of the layers. The accuracy of the method was evaluated on 20 peripapillary scans of healthy subjects. Ten of those subjects were imaged again to evaluate the reproducibility. An additional evaluation was performed to examine the robustness of the method on a variety of data: scans of glaucoma patients, macular scans and scans by a two different OCT imaging devices. A very good agreement on all data was found between the manual segmentation performed by a medical doctor and the segmentation obtained by the automatic method. The mean absolute deviation for all interfaces in all data types varied between 1.9 and 8.5 μm *(0.5-2.2 pixels). The reproducibility of the automatic method was similar to the reproducibility of the manual segmentation.*

2.1. Introduction

Today, 200 million people worldwide are either blind or have poor visual function which can significantly deteriorate their quality of life [1]. Around 80% of the existing visual impairment is caused by various eye diseases that can be prevented, slowed down or even cured by applying existing knowledge and technology [1]. Furthermore, since life expectancy is rising and many eye diseases are age-related, the number of people with reduced visual function and blindness is expected to increase by 1-2 million people per year [2]. To accommodate such a large number of people with visual problems, an efficient way to prevent or cure eye diseases is necessary. To diagnose and monitor many eye diseases, one needs to investigate the retina. With the rapid development of imaging technologies in the last decade, a three-dimensional examination of the retina has become possible.

Optical coherence tomography (OCT) provides a non-invasive, non-contact imaging technique that can be used to produce in vivo images of retinal structures with a high spatial resolution [3]. Accurate quantification of retinal structures in these 3D scans can be a very tedious job due to the required precision and large data size. Therefore, automatic extraction of clinically useful information from OCT scans, such as the thickness of a layer, is required. A critical step for quantifying the thickness of retinal layers is segmentation. To achieve reliable measurements of the thickness, the segmentation needs to be both reproducible and accurate. Furthermore, the segmentation method should perform well on a range of images as one would like to use one algorithm to segment peripapillary and macular scans obtained from different OCT systems. For screening purposes, the method should be able to pick up subtle differences between healthy and diseased eyes, whereas for disease staging and treatment monitoring small changes in diseased eyes must be detected.

Early work on segmentation of retinal layers included the analysis of intensity variations [4], intensity based Markov models [5] and adaptive thresholding [6]. These approaches suffered from intensity inconsistencies within the same layer and discontinuities in layers due to shadows caused by retinal blood vessels. As a consequence, more advanced methods were necessary which lead to the development of complex segmentation approaches. These approaches include active contours [7, 8], level sets [9–12], dynamic programming [13–17] and graph cuts [18–21]. Machine learning based approaches which rely on support vector machines [10, 22], cluster analysis [23, 24] and random forest classifiers [12, 20, 25] were also presented. Although most of the aforementioned methods perform reasonably well, they may yield anatomically incorrect results. Anatomical knowledge such as the order of the layers is exploited only when segmenting OCT data by using a hierarchical approach [8, 10, 14, 16, 17, 20, 24, 25]. However, the sequential segmentation of layers from the inside out may propagate errors to the next layer without the possibility to correct for them. A method that simultaneously segments multiple layers has been published recently [12]. In this method, a digital homeomorphisms constraint [26] is used to preserve the right relationship between layers. This constraint, although preserving the arrangement of the layers in the retina, lacks the ability to incorporate prior knowledge, e.g. thicknesses of

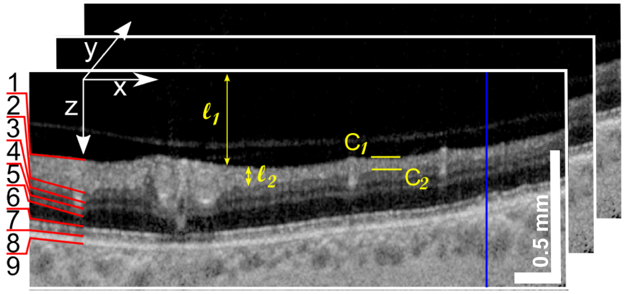

Figure 2.1: A few consecutive B-scans of attenuation coefficients comprising the 3D retina. The blue line indicates an A-scan. The 3D coordinate system is indicated with arrows in the top left corner. The full names of all retinal layers and their abbreviations are: 1) vitreous; 2) retinal nerve fiber layer (RNFL); 3) ganglion cell layer (GCL) with inner plexiform layer (IPL); 4) inner nuclear layer (INL); 5) outer plexiform layer (OPL); 6) outer nuclear layer (ONL); 7) inner segment (IS) with outer segment (OS); 8) retinal pigment epithelium (RPE); 9) choroid. Notations used for layers (l_1,l_2) and interfaces (C_1,C_2) in the segmentation framework are shown with yellow letters.

layers. Furthermore, this method is based on a random forest classifier which, like other machine learning approaches [10, 20, 22–25], may learn the changes in the appearance of the layers, but operates in a non-transparent manner. Hence, it is difficult to interpret how it works and how it can be further improved. Prior knowledge on thicknesses of layers has been used as minimum and maximum distances between two simultaneously segmented surfaces [18–20]. As a result, a specific shape was imposed on each surface. Further, most of the mentioned methods, with exception of [17, 20, 24], were evaluated only on healthy and/or diseased eyes of a particular area of the eye imaged with a single OCT device. Finally, a more detailed and complete review on recent research in retinal layer segmentation can be found elsewhere [27, 28].

This paper presents a new method for segmenting the retinal layers in OCT data. The method greatly extends our preliminary two-dimensional version [11]. It operates on the attenuation coefficients [29] derived from OCT data and incorporates anatomical knowledge about the retina. The attenuation coefficient is an optical property of the tissue, and as such is not affected by common imaging artefacts. A retinal layer's attenuation coefficient is therefore more uniform than its OCT signal. Hence, complex segmentation approaches that adapt to intensity variations are not needed and a method that operates in a transparent manner can be used. Anatomical knowledge about the retina such as the order of the layers is exploited. In addition, we can incorporate a priori knowledge about the attenuation coefficient and thickness for one or more layers. Simultaneous segmentation of the interfaces between the layers assures anatomically correct segmentation results, without error propagation as would occur in sequential processing. Interfaces are detected by using a level set approach, where prior knowledge about the retina and image data is incorporated in a probabilistic framework. An example of a few consecutive attenuation coefficients images of the retina with layer annotations is shown in Figure 2.1. Results on the following interfaces are presented: the *vitreous - RNFL*, the *RNFL - GCL*, the *IPL - INL*, the *INL - OPL* and the *OPL - ONL*, as well as the *IS ellipsoid* and the *RPE boundary*. The accuracy and reproducibility of the method is evaluated as well as the applicability to segment glaucoma affected eyes, different areas of the eye and two different OCT modalities (spectrometer based and experimental OFDI OCT system with a central wavelength of 870 nm and 1050 nm, respectively). Validation is performed by comparing the automatically and manually segmented interfaces.

2.2. Methods

Starting from the raw OCT data, a number of processing steps was performed to delineate the interfaces between the retinal layers. Figure 2.2 presents the flowchart of the developed segmentation method which consists of four main groups: pre-processing, retinal feature detection, noise suppression and the actual layer segmentation method. First, pre-processing transformed the intensities of the raw A-scans to attenuation coefficients. Then, registration was performed to re-align all B-scans. Second, we detected and segmented the optic nerve head (ONH), blood

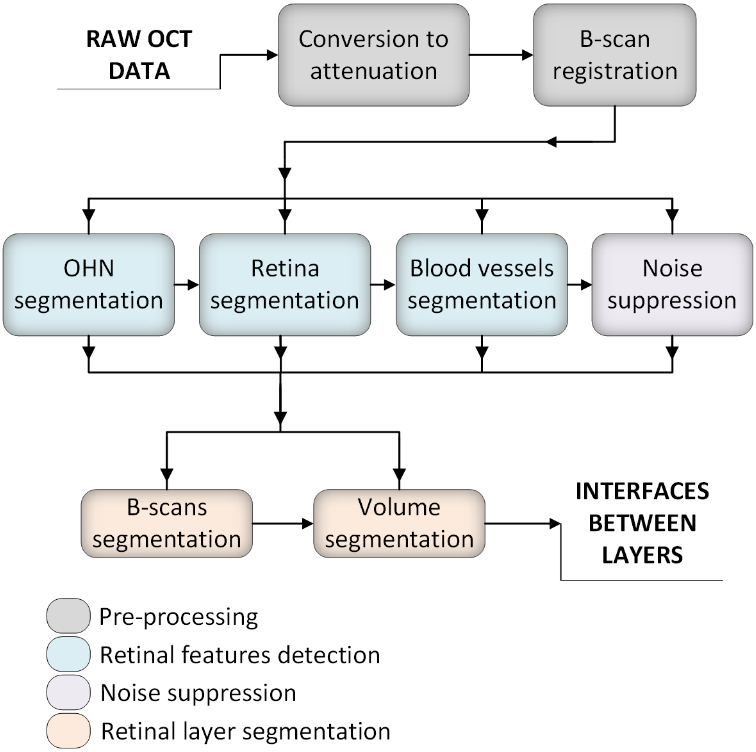

Figure 2.2: Flowchart of the presented retinal layer segmentation method comprised of four main stages indicated by different colors: pre-processing, segmentation of key retinal features, noise suppression, and the actual retinal layers segmentation.

vessels, and the retina. The ONH and blood vessels are structures that disturb the normal appearance of the layers in the retina and should therefore be addressed differently from the layers themselves. Furthermore, we provided a rough estimation of the inner and outer boundaries that surround the retina. Third, we applied a structure-driven anisotropic Gaussian filter to suppress noise in the data. Fourth, we applied the developed layer segmentation method, which simultaneously detected multiple interfaces that separate the retinal layers, to the filtered data. Within the method a novel coupling approach was used, which exploited anatomical knowledge of the retina to ensure anatomically correct results.

The pre-processing, retinal feature detection and noise suppression are described in 2.2.2, 2.2.3 and 2.2.4, respectively. The developed segmentation framework is described in 2.3, including the initialization (2.3.5) and a description of the selection of parameter values (2.3.6).

2.2.1. Data

The OCT data for this study was obtained from an ongoing study on glaucoma in the Rotterdam Eye Hospital (Rotterdam, the Netherlands). Both healthy subjects and glaucoma patients were randomly selected with the inclusion criteria of no ophthalmic disease for the healthy subjects and moderate glaucoma for the patient group. Moderate glaucoma was defined based on a visual field test (Humphrey Field Analyzer; Carl Zeiss Meditec, USA) with a mean deviation between -6 and -12 dB.

Peripapillary and macular scans were acquired with two imaging devices: the Spectralis OCT system (Heidelberg Engineering, Germany) and an experimental optical frequency domain imaging (OFDI) system [30]. The spectrometer-based Spectralis has a broadband light source with a central wavelength of 870 nm. The scan protocol for peripapillary scans combined 193 B-scans composed of 512 A-scans of 496 pixels into one volume. For macular scans the volume contained 143 B-scans composed of 384 A-scans of 496 pixels. The system employed an eye-tracker and was set to average five B-scans before moving to the next B-scan. The field-of-view was $20°$x$20°$ and $15°$x$15°$ for peripapillary and macular scans, respectively. The scanned data was strongly anisotropic with a voxel size of approximately 3.9x11.3x30 μm^3 in z, x and y direction which are the axial, the fast lateral and the slow lateral scanning axes, respectively.

The swept source based experimental OFDI system operated at a central wavelength of 1050 nm. The scan protocol acquired 1100 A-scans of 1024 pixels and

Table 2.1: Number and types of scans used in this study

Number of subjects	*Area of the retina*	*Imaging device*	*Condition*
20	Peripapillary	Spectralis	Normal
10	Macula	Spectralis	Normal
10	Peripapillary	Spectralis	Glaucoma
8	Peripapillary	1050 nm OFDI	Normal

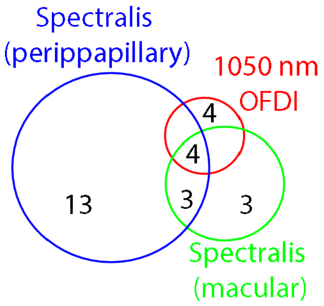

Figure 2.3: Venn diagram showing how the 27 healthy subjects are divided over the 38 ”normal” scans in the three groups (peripapillary and macular scans imaged with Spectralis and perippapillary scans imaged with 1050 nm OFDI).)

combined them into a B-scan. A full volumetric scan contained 200 B-scans. The system did not employ an eye tracker and no B-scan averaging was used. The field-of-view was 20°x20°. The voxel size was approximately 4.7x5.5x25 μm^3 in z, x and y direction.

Table 2.1 provides a summary on the number and type of subjects and scans used in this study and Figure 2.3 shows the intersection of healthy subjects between different types of scans. One B-scan was randomly selected from each volumetric scan for manual annotation. Manual segmentation was done on a slice-by-slice basis by a medical doctor using ITK-SNAP (publicly available at `http://www.itksnap.org`). The expert was asked to delineate all interfaces between the *vitreous-RNFL* and the *RPE boundary*. No special instructions were given how to handle the layers that encompass blood vessels and what to do near the ONH.

2.2.2. Pre-processing

Pre-processing comprised two consecutive steps. First, the intensities of the raw OCT data were compensated for noise and depth-dependent decay after which they were transformed into attenuation coefficients [29]. The noise floor was estimated from image data that did not contain any object. For the 1050 nm OFDI system, this resulted in a constant noise level. For the Spectralis data, however, a depth-dependent noise signal was found which may be caused by limitations of the spectrometer and post-processing of the spectra. Further, the signal decay was modelled as: $R(z) = \left(\frac{\sin(z_N)}{z_N}\right)^2 exp\left(\frac{\omega^2}{2\ln(2)} z_N^2\right)$, where z_N is the normalized depth and ω denotes the width of the Gaussian component of the decay [31]. The value for ω was determined from the signal that was generated by putting a constant scattering surface at different depths. It was estimated to be 0.81 and 2.1 for the 1050 nm OFDI and the Spectralis OCT, respectively. Newly acquired data was adjusted for noise and signal decay by subtracting the estimated noise level and dividing the results by the estimated signal decay. The corrected data was then transformed into attenuation coefficients. Being a tissue property, attenuation coefficient is illumination invariant and various artefacts such as intensity fluctuation within layers

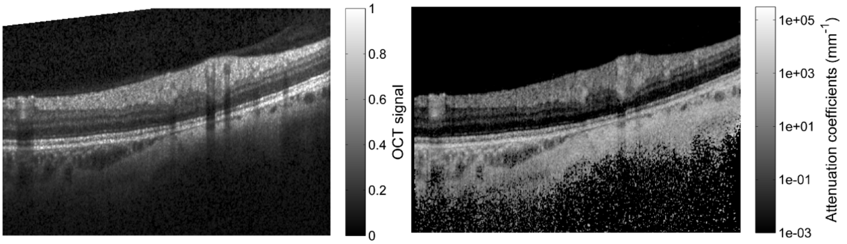

Figure 2.4: An example of the raw OCT B-scan (left), which was transformed according to the manufacturers recommendations for display purposes using $\sqrt[4]{(.)}$, and the corresponding attenuation coefficient image (right).

are therefore largely reduced. An example of the raw OCT B-scan, with clearly noticeable intensity fluctuations within the *RNFL*, and the corresponding attenuation coefficient image, with more homogeneous intensity within all layers, is shown in Figure 2.4.

Second, despite the integrated eye-tracking of the Spectralis OCT, some misalignment between consecutive B-scans remained. The misalignment violates the assumptions of spatial correlation between adjacent B-scans and continuity of the interfaces. As a result, the interfaces cannot be segmented correctly in and near misaligned scans. Therefore, a 2D cross-correlation was applied to adjacent pairs of B-scans to calculate the lateral and axial displacement. This information was then used to align all B-scans to the central frame to account for possible eye or head motion.

2.2.3. Segmenting retinal features: optic nerve head, retina and vasculature

The optic nerve head (ONH) is the location where ganglion cell axons exit the eye to form the optic nerve (the ”blind spot”). As a result, there are no retinal layers within the ONH area. Detection of the optic nerve head was done with a 3D structure tensor by using a measure of planarity defined as $\frac{\lambda_1-\lambda_2}{\lambda_1+\lambda_2}$, where λ_1 and λ_2 are the largest and the second largest eigenvalue, respectively [32]. The planarity measurement shows high values where the structure is planar and low values where it starts to become cylindrical, spherical or isotropic. In our data, the layers in the retina have a planar structure and the optic nerve head interrupts that planar structure. The Gaussian scales at which the gradient σ_g and smoothing σ_t of the structure tensor were computed corresponded to the smallest layer thickness ($\sigma_g = 20$ µm) and to the diameter of the optic cup ($\sigma_t = 575$ µm), respectively. The A-scans in which all pixels had a planarity measure smaller than 0.5 were considered to belong to the ONH area. The detected region was then expanded by including ten neighbouring A-scans from each side of the region.

The inner and outer boundaries of the retina are represented by respectively the *vitreous-RNFL* interface and the *RPE boundary*. A rough indication of these boundaries was found by using a minimum cost path search applied to individual

B-scans [33]. The cost function was computed from the Gaussian derivative in z-direction(g_z) by $1 + (g_z * I)/(\max(g_z * I))$. Two additional nodes with zero cost, that connect each pixel in the first and the last A-scans were added. These nodes acted as the source and sink, so no initial points needed to be selected. The *RPE boundary* was detected first and the area below it was excluded from the retina. Next, the *vitreous-RNFL* interface was detected.

The blood vessels in the retina, which provide a continuous blood supply to the inner retinal cells, interrupt the normal appearance of the layers and it is unclear to which layer these vessels belong to. Blood vessel detection was accomplished on a so called ”en-face image” which was created as an axial summation of the 3D-OCT data between the *vitreous-RNFL* interface and *RPE boundary* as retrieved in the aforementioned retina segmentation. Then, a vesselness enhancement filter [34] was applied to the en-face image using a Gaussian scale that corresponded to the smallest vessel width ($\sigma = 7$ µm). Finally, the vessels were segmented by thresholding the image and removing all connected objects that were smaller than 15 pixels.

2.2.4. Noise suppression

To suppress noise with a minimal increased blur, images were smoothed by using a steerable anisotropic Gaussian filter [35]. The filtering was applied to individual B-scans based on the orientation obtained from the 2D structure tensor. The scale of the Gaussian derivatives to compute the gradient corresponded to the smallest layer thickness ($\sigma_g = 20$ µm) and the Gaussian tensor smoothing corresponded to the smallest inner retina thickness ($\sigma_t = 120$ µm). The filtering was performed only along the estimated orientation with the anisotropic Gaussian filter size set to $\sigma = 32$ µm. This means that structures smaller than 32 µm will be suppressed. During the filtering, normalized convolution [36, 37] was used to avoid blurring across the blood vessels.

2.3. Segmentation framework

The presented level set framework simultaneously optimized the segmentation of all interfaces in the retina based on image information and anatomical knowledge about the properties of the layers. At each iteration of the optimization process, histograms of the attenuation coefficients were derived for each layer and the likelihood of all pixels along the interface belonging to the adjacent layers was determined. Then, prior information about the order of the layers and, if applicable, for one or more layers a prior for the attenuation coefficients and/or thickness was incorporated. Finally, geometric constraints were imposed on the solution to control the smoothness of the resulting interfaces and to prevent the interfaces from folding around noise structures.

To simultaneously segment all interfaces, loosely-coupled level sets were introduced. Image-based information and prior information were combined in a probabilistic framework and were used, together with the geometric constraints, to steer the level sets.

2.3.1. Representation of layers and interfaces

Before describing the segmentation method in more detail, some notation and definitions used throughout the paper are presented. As mentioned, the segmentation method detects the interfaces that separate the layers. One way of representing an interface is by using an implicit level set function (ϕ). Such function is then evolved by solving the partial differential equation: $\frac{\partial \phi}{\partial t} + F|\nabla\phi| = 0$, where F stands for the force acting on the level set [38]. In our application, an interface is defined as the zero level set $C = \{x, z, y | \phi(x, z, y, t) = 0\}$. The interfaces are numbered starting with the *vitreous-RNFL* interface and every interface C_i is represented by its own level set function ϕ_i. The i^{th} layer (l_i) is enclosed by two interfaces, C_{i-1} on top and C_i at bottom. The volume in-between those two interfaces is denoted with Ω_i. The (downward pointing) normal vector can be expressed as $\mathbf{n} = \frac{\nabla\phi}{|\nabla\phi|} = (n_x, n_z, n_y)$. Finally, the update of the level set, in our approach, is given as:

$$\frac{\partial \phi_i}{\partial t} = -\Delta t\left((Pr(l_i|\mu) - 0.5) + \alpha\kappa_i + \beta\zeta_i\right)|\nabla\phi_i| \tag{2.1}$$

where $Pr(l_i|\mu)$ is the probability of a voxel to belong to layer l_i, μ the attenuation coefficient of that voxel, and κ_i and ζ_i the geometric regularization terms. The weights of different terms are denoted by α and β, while Δt is the time step.

The probabilistic term expresses the posterior probability of pixels along an interface to belong to the adjacent layers as:

$$Pr(l_i|\mu) = \frac{Pr(\mu|l_i)Pr(l_i)}{\sum_{j\in\{i,i+1\}} Pr(\mu|l_j)Pr(l_j)} \tag{2.2}$$

where $Pr(\mu|l_i)$ is the likelihood based on the available image data and $Pr(l_i)$ the prior probability. Probabilities larger than 0.5 indicate that a voxel belongs to the layer before the interface, whereas probabilities smaller than 0.5 indicate that a voxel belongs to the layer after the interface. Since the volume of a layer l_i is represented by its voxels in the set Ω_i, the likelihood $Pr(\mu|l_i)$ is approximated by $Pr(\mu|\Omega_i)$. The prior probability, $Pr(l_i)$, combines prior knowledge on the attenuation coefficients values of layers ($Pr(\mu'|l_i)$) as well as prior knowledge on the order of the layers and their thicknesses ($Pr(D_i)$) as $Pr(l_i) = Pr(\mu'|l_i)Pr(D_i)$. During simultaneous detection, the probability $Pr(D_i)$ assures the correct ordering of layers, the probability $Pr(\mu|\Omega_i)$ allows adaptation to image data, whereas the probability $Pr(\mu'|l_i)$ makes the approach less sensitive to noise. To ensure resulting posterior probability remains between 0 and 1, $Pr(l_{i+1}) = (1 - Pr(\mu_i))(1 - Pr(D_i))$

Furthermore, probabilities larger than 0.5 should decrease the level set function and hence move the position of the interface downwards (in the positive z-direction), while probabilities smaller than 0.5 should increase the level set function and move the interface upwards. Since the probabilistic term returns values between 0 and 1 and the level set function is a signed distance function, a constant of 0.5 is subtracted from the probabilistic term to transform it into a suitable force that together with the regularization terms steers the level set function.

The ONH and blood vessels indicate areas where the normal appearance of the layers in the retina is interrupted and were therefore excluded from the segmenta-

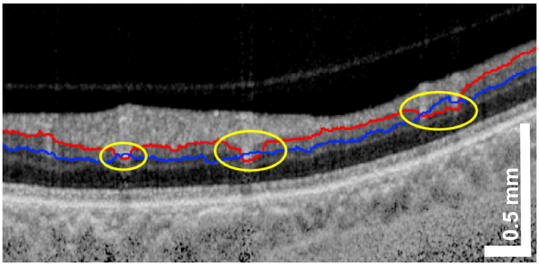

Figure 2.5: A typical example of an anatomically incorrect segmentation result. Areas where interfaces erroneously cross each other are marked with a yellow ellipses.

tion. This was done by setting the posterior probability to the non-informative value of 0.5 within the detected areas. As a result, the excluded areas were influenced only by the geometric terms in the equation 2.1.

2.3.2. Coupling through order of layers and thickness priors

Delineation of multiple interfaces in the retina using independently propagating level sets can be problematic as the detected interfaces can cross each other as shown in Figure 2.5. This is incorrect because the architecture, i.e. spatial organization, of the retina is fixed. Using this knowledge and incorporating it into a new segmentation method which optimizes a series of coupled level sets, the proper order of the layers will be assured. Furthermore, the information about the position of one interface can be used as an aid in correctly segmenting another. To fully exploit this anatomical knowledge, simultaneous detection of all interfaces is performed.

Coupling is used to allow simultaneous propagation of multiple level set functions. Most known coupling approaches concentrate on segmenting regions [26, 39–42] rather than on interfaces by avoiding overlap between the regions and allowing each pixel to be assigned to only one region. Further, through these approaches it is not possible to enforce relationships between regions, so anatomical knowledge such as the order of the layers or their thicknesses is not possible to incorporate. A concept of digital homeomorphism [12, 26] could be used to maintain proper order of the layers, but it lacks the ability to incorporate prior knowledge on thicknesses of layers. Furthermore, the complexity of known coupling approaches either increases with the number of regions [39, 40] or they cannot be extended to segment an arbitrary number of regions [41, 42]. Therefore, these approaches are neither applicable to ordered interfaces nor do they offer the flexibility we need, such as the ability to incorporate prior knowledge and the ability to simultaneously segment an arbitrary number of interfaces.

In our framework, a flexible coupling approach, which can be applied to any layered structure and extended to an arbitrary number of interfaces, is used. The idea behind the approach is to restrict the propagation of one interface C_i to the area between the two neighbouring interfaces C_{i-1} and C_{i+1}. This was modelled as the probability that a pixel at a certain depth (z-coordinate) belongs to the layer before the interface given the position of the two neighbouring interfaces and is

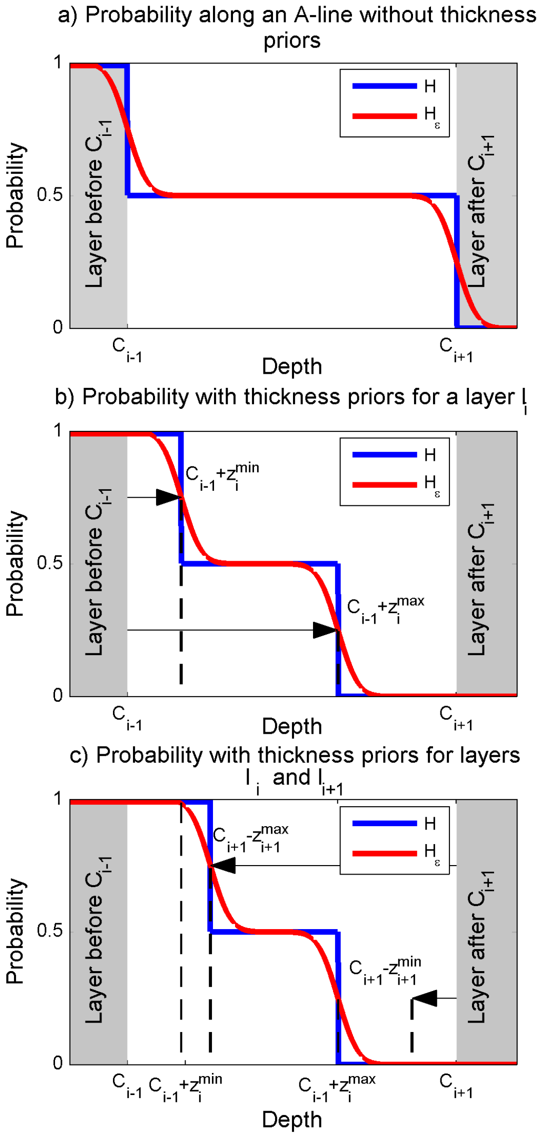

Figure 2.6: An illustration of the coupling probabilities (CP) to realize interface coupling for interface C_i along an A-scan based on the position of neighboring interfaces (C_{i-1}, C_{i+1}) and the thickness prior for a layer before (l_i) and after (l_{i+1}) the current interface. The possible positions of the current interface are those which receive a CP of 0.5. The blue curve is composed of shifted Heaviside functions (H), whereas the red curves correspond to the regularized Heaviside functions (H_ϵ). a) Without thickness priors imposed on the layer before and after the current interface, the CP of the current interface is non-descriptive, i.e. the probability is equal to 0.5 indicating that it can be positioned anywhere between the neighboring interfaces. b) Imposing a thickness prior (z_i^{min}, z_i^{max}) on the layer before the current interface restricts the position of the current interface to the region in which the CP is approximately 0.5. c) Adding a thickness constraint by the layer after the current interface $(z_{i+1}^{min}, z_{i+1}^{max})$ restricts the position of the current interface even further.

illustrated in Figure 2.6a. The probability function was set to 1 before the interface C_{i-1} which moved the position of the interface downwards. The probability after the interface C_{i+1} was set to 0 which moved the position of the interface upwards. Setting probabilities in this manner will preserve the order of the layers and ensures that the interfaces do not cross each other. Furthermore, the probability was set to the non-informative value of 0.5 for the interval between the two neighbouring interfaces (C_{i-1}, C_{i+1}). This ensures that the propagation of the level set function for the i-th interface will be based on other, image-based, information in that region.

Although a proper ordering was ensured, interfaces can get trapped in a local minimum due to a poor initialization or weak image-based information. To improve the robustness of the algorithm, prior knowledge on the minimal and maximal thicknesses of layers can be used. These thicknesses were then used as distances between interfaces. If a certain distance between interfaces was used, the probability changed such that the position of the interface moved in a way that ensured that distance is achieved. This is illustrated in Figure 2.6b, where prior knowledge on the thicknesses of a layer before an interface is used. The minimal and maximal thickness of a layer before an interface are denoted with z_i^{min} and z_i^{max}, respectively. The probability has a value of 1, not only before the interface C_{i-1} but also, for a distance z_i^{min} away from it. Defining probability in this manner moves the position of the interface downward to ensure that the minimal thickness is adhered to. To comply with the maximal thickness of a layer, the probability has a value of 0 after a distance z_i^{max} away from the interface C_{i-1}. Similarly, the minimal and maximal thickness of a layer after an interface can be added. This is illustrated in Figure 2.6c, where the minimal and maximal thickness are denoted with z_{i+1}^{min} and z_{i-1}^{max}. Additionally, to introduce more flexibility into the model, the probability for coupling can be represented with a smoother version as shown in Figure 2.6a. Finally, the coupling probability is defined for every A-scan as follows:

$$
\begin{aligned}
Pr(D_i) &= \\
&= 1 - 0.5\min(H_\epsilon(\phi_{i-1}(z - z_i^{min})), H_\epsilon(\phi_{i+1}(z + z_{i+1}^{max}))) \\
&\quad - 0.5\max(H_\epsilon(-\phi_{i-1}(z - z_i^{max})), H_\epsilon(-\phi_{i+1}(z + z_{i+1}^{min})))
\end{aligned}
\tag{2.3}
$$

where H_ϵ is the regularized Heaviside function, which is in our case based on the error function $H_\epsilon(z) = 0.5 + 0.5\,\mathrm{erf}(z/\epsilon)$.

2.3.3. Steering by attenuation coefficients

The coupling described in the previous section allowed simultaneous detection of multiple interfaces by limiting the propagation of the interface. However, other information was still needed to retrieve the correct segmentation of it. This was done by exploiting the differences in the attenuation coefficients between both sides of an interface.

Using tentatively segmented volumes of the layers, the normalized histograms of the layer before (h_i) and the layer after (h_{i+1}) an interface were computed. These histograms modelled the likelihoods for observing attenuation coefficients values in layers around the interface. The probability $Pr(\mu|\Omega_i)$ was therefore set to $h_i(\mu)$, whereas the probability $Pr(\mu|\Omega_{i+1})$ was equal to $h_{i+1}(\mu)$. These probability were further used in expression 2.2 to determine whether a pixel belongs to a layer before or after the interface based on the current positions of the interfaces.

Since layers in the retina interact differently with the incoming light, information about their optical properties was used to make the approach more robust. The (weak) prior probabilities on the attenuation coefficients of the layers that surround an interface was modelled as:

$$Pr(\mu'|l_i) = \gamma\,\mathrm{erf}\left(\frac{\log(\mu) - \log(\mu_c)}{\sigma}\right) + 0.5 \tag{2.4}$$

The values γ, μ_c and σ control the magnitude, threshold and slope of the probability, respectively. The magnitude controls the strength of the prior, the threshold indicates the attenuation value between that of the surrounding tissues, and the slope controls the smoothness of the transition between the surrounding tissue. Figure 2.7 shows an example of the probability of the attenuation coefficients with the parameters indicated. The values for the aforementioned parameters will be described in section 2.3.6.

2.3.4. Geometrical constraints on level sets

The geometric constraints on the resulting level set were imposed by two regularization terms. The conventional curvature term, defined as $\kappa_i = \nabla \cdot \mathbf{n_i}$, was used to penalize the length of the interface. This term imposes the necessary smoothness to avoid a heavily curved interface that closely follows the speckle noise pattern in the OCT data. An additional regularization term was implemented to prevent an interface to fold back on itself.

An example of an interface that folds back is depicted in Figure 2.8a. This behaviour is anatomically unlikely to occur and needs to be prevented. The non-folding constraint regulates the orientation of the normal vector to the level set function and thus prevents anatomically incorrect behaviour.

To prevent interfaces from folding back, the mean curvature and normal vectors to the level set function were used. Normal vectors with a negative component (upward pointing) in the z-direction were considered to violate the anatomically correct situation (depicted by red arrows in Figure 2.8b). The level set function in those areas was then updated based on the sign of the curvature and the projection of the level set normal onto the x-y plane. The sign of the curvature determined the sign of the update in the level set function, where a negative value will result in a decrease (negative update) of the level set function whereas a positive value will result in an increase (positive update) of the level set function. Furthermore, the projection of the normal onto the x-y plane controls the strength of the change. In Figure 2.8c, green arrows show the direction and strength of the force induced by this regularization term. The term is expressed by:

$$\zeta_i(\phi_i) = \left(1 - H(n_i^z)\right)\mathrm{sgn}(\kappa_i)\sqrt{(n_i^x)^2 + (n_i^y)^2} \tag{2.5}$$

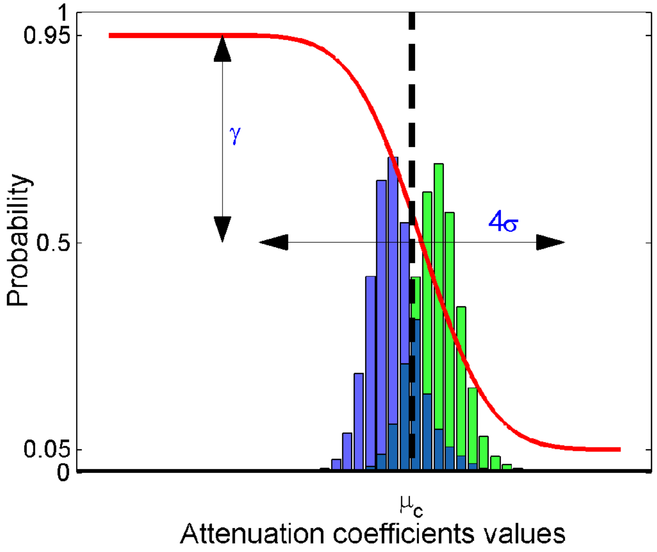

Figure 2.7: Example of prior probability of the attenuation coefficients (red curve) around the position of the interface (vertical dashed line). The normalized histogram of the layer before and after an interface are shown in blue and green, respectively. The values γ, μ_c and σ control the strength of the prior, the assumed attenuation value at the interface, and the slope of the probability as indicated on the figure. A smaller value of σ will result in a sharper slope of the probability. The sign of γ depends on whether the layer before an interface has a lower or a higher attenuation coefficient. In this figure, the layer before an interface is darker than the one after it ($\mu_{l_i} < \mu_{l_{i+1}}$), hence the sign of γ is negative.

where n_i^x, n_i^z and n_i^y are the x, z, y component of the normal vector, respectively. The effect of this regularization term on an interface is shown in Figure 2.8d.

2.3.5. Initialization

Propagation of the level set functions is done by simultaneously solving the set of partial differential equations that drive the current segmentation of the retinal interfaces to its minimum energy state. A rough indication of the inner and outer boundaries of the retina were estimated as described in section 2.2.3. Using the same cost function as in section 2.2.3, but considering only the area within the detected retina, the *INL-OPL* interface was initialized. The other interfaces were initialized based on fixed distances from either the *RPE boundary*, the *vitreous-RNFL* or the *INL-OPL* interface as follows. The *IS ellipsoid* was initialized to be 40 µm before the *RPE boundary*. Then, for peripapillary/macular scans, the *RNFL-GCL* interface was initialized to be 60/20 µm after the *vitreous-RNFL* interface; the *IPL-INL* interface was initialized to be 20/36 µm before the *INL-OPL*; the *OPL-ONL* interface was initialized to be 48/80 µm before the *IS ellipsoid*. A typical example of an initialization and the corresponding final segmentation results for all interfaces is

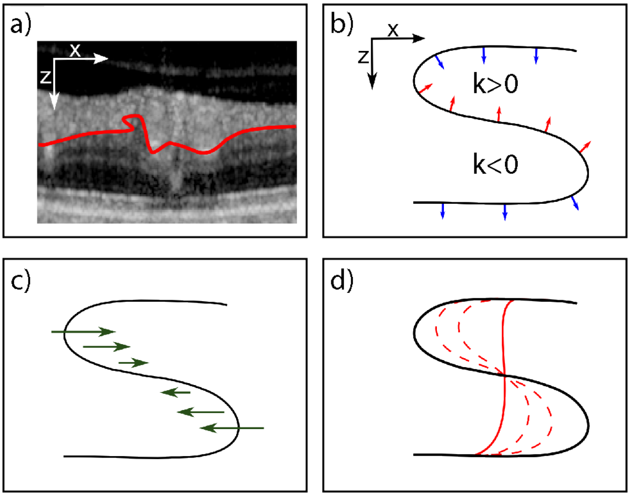

Figure 2.8: a) Example of an interface that folds back. b) Sketch of an interface that folds back with arrows indicating the normal vector to the level set function. Red arrows indicate vectors that violate the anatomical correctness. c) The interface of b) in which the arrows represent the correction force. The direction of the change is derived from the sign of the curvature, where negative curvature results in an negative update in the level set function. The length of the arrows correspond to the strength of the correction force which is derived from projection of the level set normal on the x-y plane. d) Evolution of the interface due to the correction term is shown with dashed red line. Final result is shown with solid red line.

Table 2.2: Minimum thickness priors per layers for the peripapillary and the macular scans

	Minimum thickness (μm)	
	Peripapillary	Macular
INL	12	12
OPL	12	16
ONL	20	12

presented in Figure 2.9. This example shows that only a coarse initialization of the interfaces is required and that correct segmentation results can be obtained with the developed method even if some of the interfaces are initialized wrongly (e.g. the *RPE boundary* which was initialized at the *IS ellipsoid* in the example).

After this coarse initialization, level set segmentation was performed on individual B-scans to get a better initialization for the full volume segmentation. First, every ninth B-scans was segmented after which the segmentation results were interpolated and used as an initialization for every third B-scan. Again, the results were interpolated and used as initialization for segmenting individual B-scans which became the initialization for the full volume segmentation.

2.3.6. Parameter selection

In the update equation for the level set function (equation 2.1), three parameters (α,β,Δt) need to be set. In addition, prior knowledge on thicknesses of layers and parameters in equation 2.4 need to be determined. All parameters were estimated from an additional dataset which was independent of those used for the assessment of the accuracy and reproducibility.

The time step was chosen as: $\Delta t = 1/2n$, where n represents the dimensionality of the data. This time step satisfies the Courant-Friedreichs-Lewy (CFL) condition [43] and ensures stability of the level set function. The smoothness of the interface was controlled by the parameter α, which was evaluated at 0.65, 1.25, 2.5 and 5. A good compromise between the smoothness/rigidness of the interface and ability to follow the subtle changes in the interface was found for $\alpha = 2.5$. The parameter β controlled the strength of the folding back correction and was set to the smallest value that ensured no folding back of the interface which was 1.

The stopping criteria for the level set propagation was a combination of the maximum number of iterations and a check if the solution is stationary. The solution was considered stationary if the root mean square difference between the last two updates of the level set function was smaller than 0.02 pixels for all interfaces. The maximum number of iterations was set to 300.

We used minimum thickness priors for three layers in the peripapillary and macular scans as reported in Table 2.2. The maximum thickness prior was used only for the *GCL-IPL* layer in peripapillary scans and was set to change spatially. The

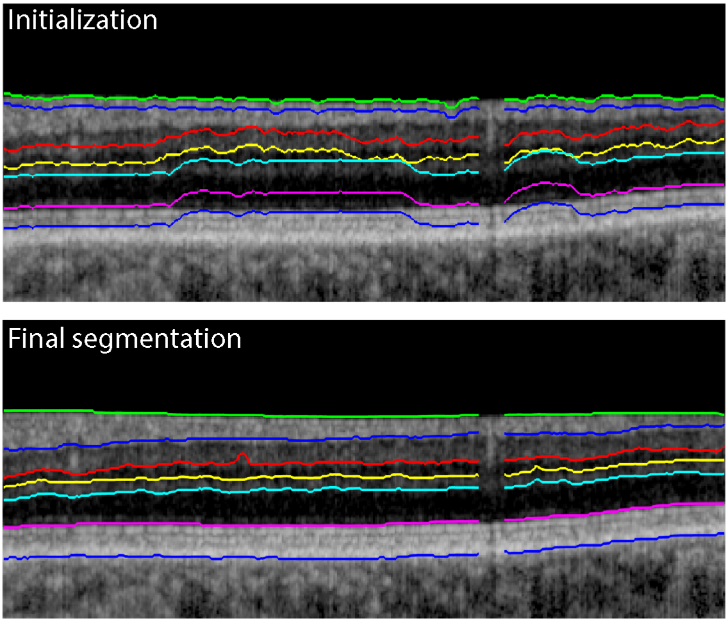

Figure 2.9: A typical example of an initialization (top) and the resulting final segmentation (bottom) for all interfaces.

Table 2.3: Values for the parameter μ_c of the attenuation prior per interface

	μ_c(mm^{-1})
Vitreous - RNFL	0.30
RNFL - GCL	1.35
IPL - INL	0.11
INL - OPL	0.18
OPL - ONL	0.08
IS ellipsoid	0.18
RPE boundary	12.75

equation for the maximum thickness prior for the left eye was determined experimentally and was set to: $z = 88 + 88exp(-\frac{x^2+(y-y_c)^2}{2*1000^2})$ µm, where y_c is the y coordinate of the central location of the ONH.

Since the assumed thickness priors are not applicable to the fovea, we detected in every macular scan the point with the smallest retinal thickness (i.e. the distance between the *vitreous-RNFL* and the *RPE boundary*). No thickness prior was imposed within a radius of 450 µm from the detected point.

The priors on the attenuation coefficients, given by equation 2.4, were different for every interface. Hence the values for γ, μ_c and σ needed to be adjusted accordingly. Parameter γ controlled the direction and the magnitude of the error function and was set to values ± 0.45 depending whether the layer before the interface is brighter or darker than the layer after the interface. The resulting prior probability ranged from 0.05 to 0.95. Further, the values for μ_c were determined experimentally. The normalized histograms of layers that surround an interface were examined and the value at which the two attenuation coefficient histograms cross was chosen as the value for μ_c. Table 2.3 provides information on the values used for the parameter μ_c. The slope of the error function was controlled by parameter σ and was chosen such that most of the points of the histograms that surround the interface lie within 2σ of μ_c. In this way, the influence of the prior probability on the final posterior probability was strong only for the attenuation coefficient values that were far away from the assumed attenuation value (more than $\mu_c \pm \sigma$). This stabilized the posterior probability in case of noisy data. For the attenuation values that were close to the assumed attenuation value (within $\mu_c \pm \sigma$), the prior probability had a weak influence and the posterior probability was driven by other information. Finally, the slope was set to a value 2 for all interfaces except for the *vitreous-RNFL* interface. There, the slope was set to 0.75 to assure the detached part of the *vitreous* was segmented as a part of the *vitreous*.

2.4. Experiments and results

A quantitative evaluation was performed to assess the accuracy and reproducibility of the presented method. Two sets of experiments were performed. The accuracy and reproducibility of the method was evaluated in the first experiment. In a

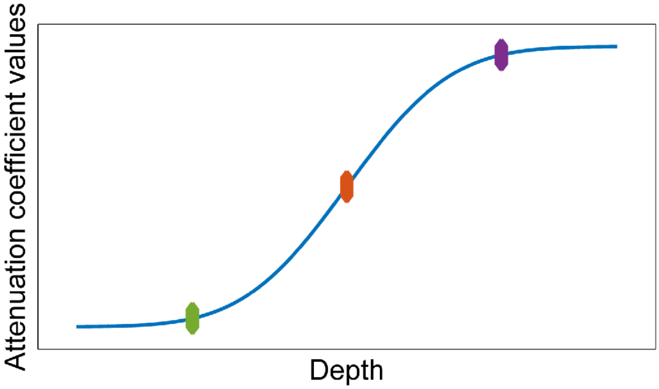

Figure 2.10: An illustration of an interface between two layers is depicted by the blue line. Three possible segmentation results of that interface are depicted by the green, orange and purple diamond. Although all three segmentations are correct, they vary in depth.

second experiment, the ability of the method to segment different data types was examined. In addition to the seven interfaces, the thickness of the *RNFL* was evaluated. Finally, an additional experiment was performed to evaluate the accuracy and reproducibility of ”The Iowa Reference Algorithms” [18, 21, 44] on our dataset.

For every interface, the accuracy was determined by comparing the results of the automatic algorithm with the manually segmented data. Manual segmentation was performed by a medical doctor. The root-mean-square error (RMSE) and the mean-unsigned-deviation (MUD) were considered. The errors were computed for every A-scan and then averaged. The reproducibility of manual and automatic segmentation was also evaluated by the same error measures. A-scans crossing either the retinal vasculature or the ONH were excluded in calculating the errors.

To eliminate a possible bias due to different criteria in automatic and manual segmentation, the systematic error was estimated as the mean difference between the manual and the automatic segmentation using five-fold cross validation. This systematic error represents a difference that may occur across all retinal images due to different criteria that a manual annotator and the automated method might have used to segment the interfaces. In other words, the error was used to adjust the automatic segmentation to resemble the implicit definition of an interface present in the manual annotations. To clarify this, an illustration of an interface between two layers with three possible segmentations is shown in Figure 2.10. Finally, the error was then subtracted from the automatic segmentation after which the RMSE and MUD were recomputed. The cross validation was repeated 10 times using different combination of subjects in the subgroups.

2.4.1. Accuracy and reproducibility evaluation

The main evaluation of the presented segmentation method was done on peripapillary scans of normal subjects scanned with Spectralis. The scans of 20 subjects (one eye per subject) were used to estimate the accuracy of the method. For 10

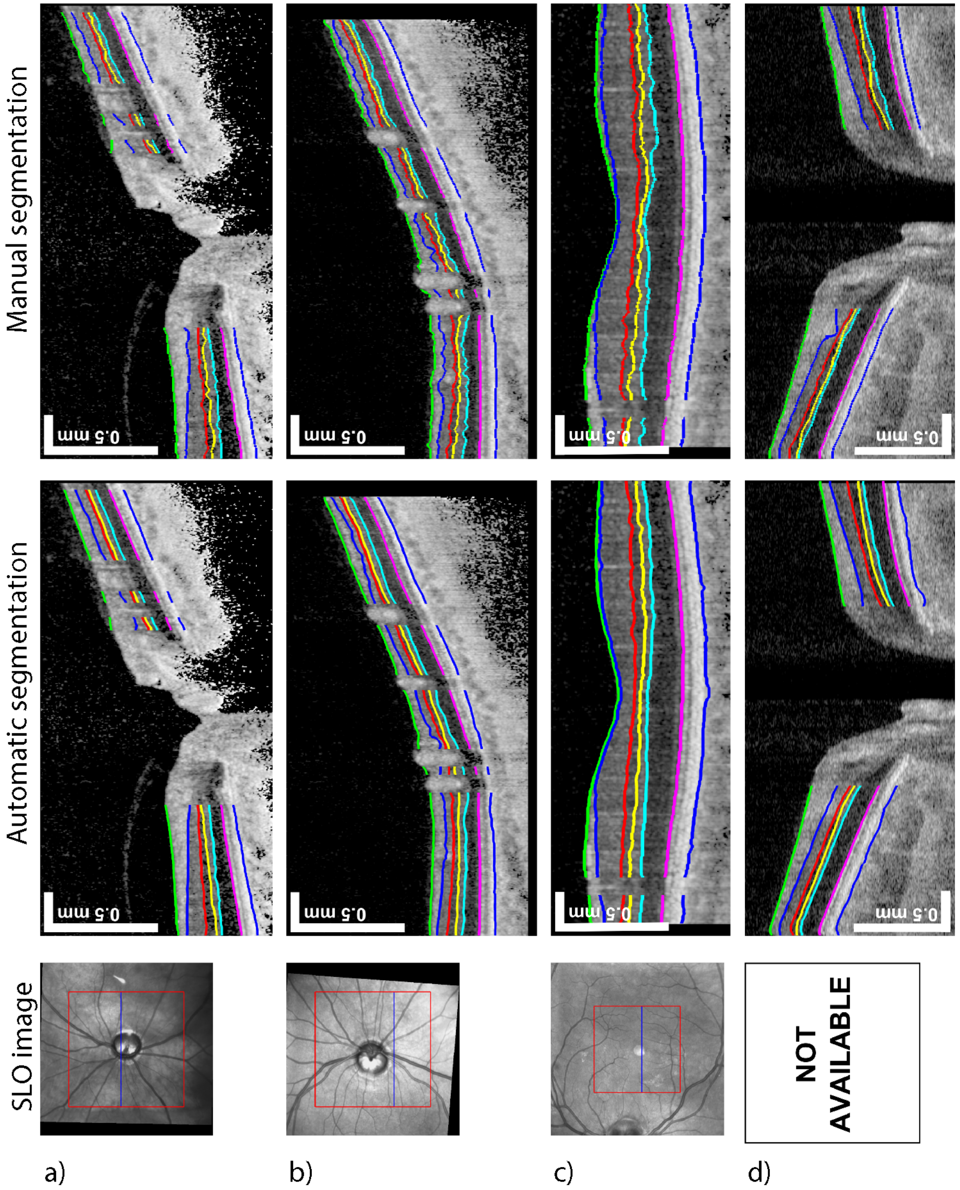

Figure 2.11: A scanning laser ophthalmoscopy (SLO) image of the retina where a red square indicates the scan area. Blue line on the SLO image indicates the B-scan for which both the automatic and manual segmentation results are shown. The reported images are: A) Peripapillary scan of normal retina by Spectralis, B) Peripapillary scan of glaucoma patient by Spectralis, C) Macular scan of normal subject by Spectralis, and D) Peripapillary scan of normal subject by 1050 nm OFDI. The gaps in the interfaces indicate either the areas of the blood vessels or the optic nerve head where most interfaces are ill-defined.

out of those 20 subjects the reproducibility of both the manual and automatic segmentation was estimated by comparing the results of two successive scans. Before a second scan was made, the subject was asked to stand up, after which the head and eyes were again realigned with the OCT system.

Figure 2.11 shows an example of the manual annotation and the segmentation results obtained with the described method. Using the segmentation results obtained with the developed method one can compute the thickness maps of different layers or examine attenuation coefficient values for different layers. Examples of the 2D thickness map of the *RNFL* and spatial map of attenuation coefficient values for the *RNFL* are shown in Figure 2.12.

Table 2.4 provides detailed results on the accuracy of the automatic method before and after bias correction as well as the reproducibility. An error of 3.9 µm corresponded to one pixel along the recorded A-scans. The accuracy evaluation, after bias correction, showed a RMSE ranging from 3.4 µm to 9.4 µm and a MUD ranging from 2.7 µm to 7.0 µm. The reproducibility of the automatic method had a RMSE between 2.7 µm and 6.7 µm, and a MUD ranging from 2.1 µm to 5.1 µm, whereas, the reproducibility of the manual annotations resulted in a RMSE between 4.2 µm and 10.6 µm and a MUD ranging from 3.1 µm to 7.4 µm.

The Wilcoxon signed test was used to compare the reproducibility of the manual annotations with the reproducibility of the automatic method and to compare the accuracy of the automatic method with the reproducibility of the manual annotation. This test was chosen because it allows a paired test without requiring that the samples are normally distributed. For all performed statistical test (both in the current and the following section), when applicable, only results after bias correction were considered. The resulting p-values are reported in Table 2.4.

2.4.2. Evaluation on various types of data

The second set of experiments was performed to assess the applicability of the method for a variety of data. Ten macular scans of healthy subject and 10 peri-paripally scans of glaucoma subjects imaged with Spectralis were considered. In addition, 8 peripapillary scans of healthy subject were imaged with the 1050 nm OFDI system.

Table 2.5 reports the accuracy of the automatic method on the aforementioned data categories before and after bias correction. For glaucoma affected eyes, the systematic error was estimated from all healthy subjects (from section 2.4.1). An error of 4.7 µm corresponded to one pixel along the A-scans of the 1050 nm OFDI system.

Examples of the manual annotations and the segmentation results obtained with the described method for all three groups are shown in Figure 2.11. In addition, examples of spatial maps of attenuation coefficient values for the *RNFL* and the thickness map of the *RNFL* for each group are shown in Figure 2.12.

Segmentation of macular scans showed a RMSE between 2.7 µm and 7.6 µm and a MUD between 1.9 µm and 5.9 µm after bias correction. For segmentation of the glaucoma affected peripapillary scans, the RMSE and MUD after bias correction ranged from 3.6 µm to 11.4 µm and from 2.9 µm to 8.5 µm, respectively. Scans

Table 2.4: Accuracy evaluation before (within parentheses) and after bias correction. Reproducibility evaluation of the automatic and manual segmentation

	Accuracy				*Reproducibility*					
					Automatic				*Manual*	
	RMSE (µm)	p - value*	**MUD** (µm)	p - value*	**RMSE** (µm)	p - value**	**MUD** (µm)	p - value**	**RMSE** (µm)	**MUD** (µm)
Vit.-RNFL	4.3 (4.3)	0.01	3.4 (3.5)	0.01	3.0	0.04	2.3	0.04	5.9	4.8
RNFL-GCL	9.4 (9.8)	0.03	7.0 (7.1)	> 0.05	6.7	> 0.05	5.1	> 0.05	10.6	7.4
IPL-INL	6.6 (6.7)	> 0.05	5.1 (5.2)	> 0.05	6.0	> 0.05	4.5	> 0.05	6.8	5.0
INL-OPL	7.5 (7.5)	> 0.05	5.8 (5.9)	0.01	4.8	> 0.05	3.5	> 0.05	7.6	5.9
OPL-ONL	5.6 (5.6)	0	4.5 (4.7)	0.01	5.1	0	4.2	0.03	7.6	5.6
IS ellip.	3.4 (3.4)	0	2.7 (2.7)	0	2.7	0	2.1	> 0.05	4.2	3.1
RPE boun.	4.9 (5.3)	> 0.05	3.8 (4.3)	> 0.05	5.4	> 0.05	4.3	> 0.05	5.3	4.0
RNFL th.	10.2 (10.3)	0.01	7.5 (7.5)	0.01	6.3	0	4.6	0.04	12.2	9.1

*Accuracy compared to manual reproducibility; **Automatic reproducibility compared to manual reproducibility acquired with the 1050 nm OFDI system had a RMSE of 3.2 - 8.4 μm and a MUD between 2.6 μm and 5.7 μm after bias correction. Finally, for all data types, individual unsigned errors per A-scan were collected and the 95 percentile error was found to be 13.7 μm.

The Mann-Whitney test was performed to compare the accuracy of each of the different data types with the accuracy evaluation for the same interface from the previous section. This test was chosen as it allows comparison of unpaired groups without requiring that the samples in groups are normally distributed. The resulting p-values are reported in Table 2.5.

2.4.3. The Iowa Reference Algorithms

We compared our results with those of the publicly available ”The Iowa Reference Algorithms” (Retinal Image Analysis Lab, Iowa Institute for Biomedical Imaging, Iowa City, IA). The provided version segments four interfaces: the *vitreous-RNFL*, the *RNFL-GCL*, the *IPL-INL* and the *RPE boundary*. However, it marks some areas of the volume scan as undefined and does not provide any segmentation results in those areas. On our data sets, the average size of the undefined regions corresponded to 11% of the field of view, but ranged up to 62%.

The Iowa Reference Algorithms were applied to all data and the errors were analysed excluding the undefined regions. Additionally, the errors of our method were re-estimated excluding the same regions. All details, including results before and after bias correction, can be found in Appendix 2.A. In summary, the accuracy evaluation of The Iowa Reference Algorithms showed a RMSE ranging from 4.1 μm to 11.8 μm and a MUD ranging from 3.3 μm to 8.5 μm for all data types. The reproducibility of The Iowa Reference Algorithms had a RMSE between 4.6 μm and 7.8 μm, and a MUD ranging from 3.4 μm to 5.6 μm. These results are similar to the accuracy and reproducibility of the proposed method.

2.5. Discussion and conclusion

This paper presents a new method to simultaneously segment interfaces between the layers of the retina in 3D OCT data. The method is based on a novel level set approach which uses Bayesian inference. The approach incorporates anatomical knowledge about the retina and enforces anatomically correct segmentation results. Both accuracy and reproducibility of the method were evaluated, as well as the robustness to segment different data types. A good agreement between the segmentation performed manually by a medical doctor and results obtained from the automatic segmentation was found (the MUD for all interfaces in all data types varied between 1.9 and 8.5 μm (0.5-2.2 pixels)).

Statistical analysis performed on the automatic and manual reproducibility indicates that automatic segmentation is more consistent than manual annotation for the *vitreous-RNFL*, and *OPL-ONL* interface. For other interfaces both the segmentation done automatically and manually are equally good. Furthermore, a paired comparison between the accuracy of the automatic method and the reproducibility of the manual annotator shows a statistically significant difference for three inter-

Table 2.5: Accuracy evaluation before (within parentheses) and after bias correction on different data categories

	Macula				*Glaucoma*				*1050 nm OFDI system*			
	RMSE (µm)	p - value*	**MUD** (µm)	p - value*	**RMSE** (µm)	p - value*	**MUD** (µm)	p - value*	**RMSE** (µm)	p - value*	**MUD** (µm)	p - value*
Vit.-RNFL	3.3 (3.3)	0.03	2.7 (2.7)	0.04	4.6 (4.7)	> 0.05	3.7 (3.7)	> 0.05	3.3 (4.2)	0.01	2.5 (3.4)	0.01
RNFL-GCL	6.0 (6.9)	0.01	4.7 (5.5)	0	11.4 (11.5)	> 0.05	8.5 (8.8)	> 0.05	8.4 (8.4)	0.03	5.7 (5.7)	0.01
IPL-INL	7.4 (7.4)	> 0.05	5.9 (5.9)	> 0.05	5.6 (6.0)	> 0.05	4.3 (4.6)	> 0.05	5.5 (5.5)	0	4.3 (4.3)	0
INL-OPL	7.3 (7.4)	> 0.05	5.7 (5.7)	> 0.05	6.5 (6.7)	> 0.05	5.1 (5.2)	> 0.05	6.0 (6.1)	0	4.9 (4.9)	0.01
OPL-ONL	7.6 (7.6)	> 0.05	5.6 (5.6)	> 0.05	5.3 (5.4)	> 0.05	4.1 (4.2)	> 0.05	5.0 (5.3)	0.01	4.0 (4.1)	0.04
IS ellip.	2.7 (3.5)	0.03	1.9 (2.9)	0.002	3.6 (3.7)	> 0.05	2.9 (3.1)	> 0.05	3.2 (4.4)	0	2.6 (3.8)	0
RPE bou.	5.2 (5.2)	> 0.05	4.0 (4.1)	> 0.05	6.0 (6.5)	> 0.05	4.6 (5.2)	> 0.05	5.4 (5.4)	> 0.05	3.9 (3.9)	> 0.05
RNFL th.	6.8 (7.6)	0	5.3 (5.9)	0	12.0 (12.1)	> 0.05	9.2 (9.2)	> 0.05	9.5 (9.4)	0.01	7.0 (7.0)	0

*Accuracy of individual groups compared to the accuracy in table 2.4

faces (the *vitreous-RNFL*, the *OPL-ONL* and the *IS ellipsoid*) and no statistically significant difference for other interfaces, leading to the conclusion that the developed segmentation method is performing at least as good as the manual annotator.

As there was no reproducibility evaluation on the individual groups in section 2.4.2, additional statistical analysis was performed to compare the accuracy of these groups with the accuracy reported in section 2.4.1. This was important as the accuracy in section 2.4.1 is compared against the performance of the manual annotator.

This additional statistical analysis showed that the developed method works equally good on glaucoma subjects. More specifically, there was no statistical difference in the segmentation of the *vitreous-RNFL* and the *RNFL-GCL* interface between healthy and glaucoma affected eyes. This indicates the possibility to use the developed framework for clinical purposes in the context of glaucoma diagnosis and management.

The accuracy evaluation and performed statistical analysis shows that the method can be used to segment scans of different area of the eye. The only parameter values that needed to be adjusted to segment the macular scans were the thickness priors (Table 2.2). In addition, for some interfaces (the *vitreous-RNFL*, the *RNFL-GCL* interface and the *IS ellipsoid*) the method performs better on the macular scans than on the peripapillary scans. This could be due to the fact that the macular scans often seem more uniform than the peripapillary scans.

The developed method may be applied to scans obtained with different OCT devices, without any adjustments to the method. Also, statistical analysis showed that the segmentation performed on scans obtained with the 1050 nm OFDI system is better for all interfaces except the *RPE boundary*. This could be a result of the age difference in the two groups: the average age of the subjects imaged with the 1050 nm OFDI system was 42 years, whereas the average age of the subjects imaged with the Spectralis was 64 years.

Comparison between our method and other retinal segmentation methods found in the literature is difficult as every method is evaluated on data acquired with a different OCT device or on different types of retinal images. In addition, there is no single standard for performing manual annotations or for reporting the accuracy or reproducibility, so they may vary from method to method. Therefore, we also segmented our data with the publicly available ”The Iowa Reference Algorithms” and evaluated its accuracy and reproducibility. The accuracy and reproducibility of the presented method is comparable to that of ”The Iowa Reference Algorithms”, indicating that our algorithm performs similar to the current state-of-the-art software for retinal layer segmentation. An advantage of our method is that it provides segmentation results over the whole volume. Furthermore, use of prior knowledge in our approach is limited to only a few layers, whereas ”The Iowa Reference Algorithms” uses prior knowledge on the minimal and maximal thickness for all layers [18] thus making the method more difficult to adapt to diseased eyes.

Further comparison with other segmentation methods is done only in a qualitative manner. Some of the most recent published work [12, 16, 19, 24, 25], performed a 3D segmentation on macular scans of healthy subjects and reported a MUD between 3-7 µm. This result is comparable to our MUD for segmenting

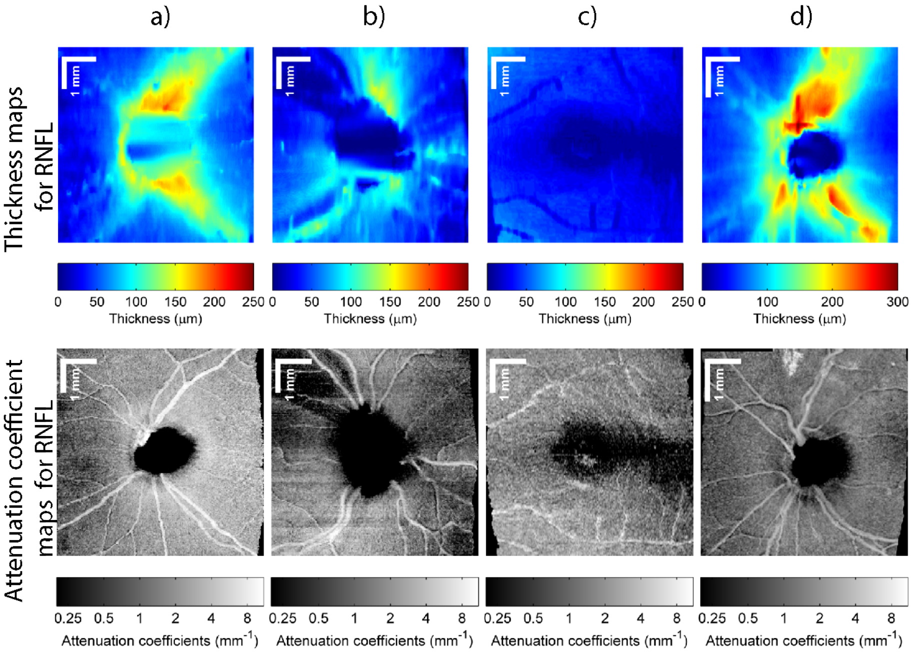

Figure 2.12: Examples of the generated spatial map of the attenuation coefficient values for the RNFL and the thickness map of the RNFL from different data types: A) Peripapillary scan of normal retina by Spectralis, B) Peripapillary scan of glaucoma patient by Spectralis, C) Macular scan of normal subject by Spectralis, and D) Peripapillary scan of normal subject by 1050 nm OFDI. Spatial maps of attenuation coefficients for the RNFL were created as an axial mean of the 3D-OCT data between the vitreous-RNFL and RNFL-GCL interface, whereas the thickness maps of the RNFL were created by measuring the distance along each A-scan from the vitreous-RNFL interface to the RNFL-GCL interface.

the macular scans (Table 2.5) indicating that we are performing similarly. A mean absolute deviation between 3-10 μm was reported when segmenting peripapillary scans of glaucoma subject [20, 24]. Our MUD for segmenting the glaucoma scans (Table 2.5) ranged between 3 and 9 μm indicating similar accuracy. Furthermore, some of the previously mentioned methods were evaluated only on healthy and diseased subjects [12, 19, 25], whereas ours also considers different areas of the eye and two different OCT devices and thus provides a method more suitable for segmenting OCT data due to a wider range of evaluated types. Data from different OCT devices was considered in [17], but only mean retinal thickness was reported. Other mentioned methods were also evaluated on data from different OCT devices, but these methods are based on a machine learning approach [20, 24]. As such, the final result is largely dependent on the number of examples included in the training set. This can be a limiting factor for adaptation of the method to different data types [20]. With our method, to segment data from the two different imaging devices, no changes were needed.

In Figure 2.12, some of the possible applications of the developed method are presented. Using 3D segmentation of the retina, one can easily create and examine thickness maps or spatial maps of attenuation coefficients for different layers in the retina. Analysis of attenuation coefficients maps could be of a particular interest, as it was shown that there is a difference between attenuation coefficient values of healthy eyes and glaucoma affected eyes [45]. Finally, although the approach operates on attenuation coefficient data, one can use the obtained segmentation results of the interfaces and map them to the original OCT data.

There are several potential limitations of the presented work. Although the developed method performs well on glaucoma affected eyes, we expect that some modifications are necessary to handle topology-disrupting pathologies. However, we believe some of these pathologies, yielding the accumulation of fluids and microcysts, can be addressed by pre-segmenting and masking, as was done for the blood vessels and optic nerve head in the current framework. Furthermore, the imposed prior knowledge about a layer's thickness and attenuation coefficient values may not be valid in all other diseases. Despite differences in *RNFL* attenuation coefficients between normal and glaucomatous eyes [45], we were able to segment both normal and glaucoma subjects equally well using the same prior on the attenuation coefficients. Prior knowledge on the layer thickness is limited to only a few layers and could easily be adjusted to incorporate other knowledge if required. Further, the level set method, unlike graph cuts for retinal layer segmentation [18–21], cannot guarantee a globally optimal solution. However, our framework contains several adaptations to reduce the chances of an interface getting stuck in a local minimum. Simultaneous segmentation of all interfaces and coupling between the level set functions allows correction for most of the possible errors that may occur during initialization. Additionally, to reduce the sensitivity of the method to speckle noise, an adaptive noise suppression step was added, which further reduces the chances of the segmentation getting stuck in a local minimum. An example that illustrates the robustness of the proposed framework and its capability to generate a correct segmentation from an erroneous initialization is shown in Figure 2.9. Finally, from a computational point of view, the presented method is computationally expensive and takes on average 1 hour and 56 minutes to process a full 3D OCT scan. However, the computation time has not yet been optimized and could be substantially improved by sub-sampling, parallelization or improving the stopping criterion.

Overall, our method provides a flexible, accurate and robust solution in segmenting layered structure in the retina. We showed how it can be applied to various data types (healthy and glaucoma subject; different area of the eye; two different OCT devices) where it produces similar results. The developed framework allows simple and intuitive modification of prior knowledge. Our model included prior knowledge on the attenuation coefficients and thicknesses of the layers, but it could easily be extended to include other sources of information. Furthermore, we believe that the presented coupling approach could be applied to any other structure with a predefined order of the layers and extended to an arbitrary number of interfaces.

Future work will include extension of the method to segment thin membranes in the outer retina and an evaluation on larger dataset of glaucoma affected eyes to investigate if the method could be used as an aid to diagnose and monitor glaucoma in a clinical setting.

2.A. Appendix

The segmentation results obtained with ”The Iowa Reference Algorithms” were compared with our manual annotations. For error calculations, undefined regions and the A-scans crossing either the retinal vasculature or the ONH were excluded. To compare these results with the results obtained by using our segmentation algorithm, the accuracy and reproducibility of our method were recomputed excluding the A-scans marked as undefined by ”The Iowa Reference Algorithms”. Table 2.6 and 2.7 provides detailed results on the accuracy of the two automated methods before and after bias correction and the reproducibility of ”The Iowa Reference Algorithms” for four interfaces.

Table 2.6: Accuracy evaluation before (within parentheses) and after bias correction and reproducibility evaluation of our method and The Iowa Reference Algorithms excluding A-scans crossing blood vessels, ONH and undefined regions produced by The Iowa Reference Algorithms

	Accuracy			
	Iowa		*Our*	
	RMSE (µm)	**MUD** (µm)	**RMSE** (µm)	**MUD** (µm)
Vitre.-RNFL	5.2 (6.1)	4.1 (4.6)	4.0 (4.1)	3.3 (3.4)
RNFL-GCL	11.8 (12.7)	8.5 (8.9)	8.9 (9.6)	6.7 (7.0)
IPL-INL	8.3 (8.3)	6.3 (6.3)	6.4 (6.4)	5.0 (5.0)
RPE bound.	5.7 (6.1)	4.4 (4.5)	5.0 (5.2)	3.9 (4.2)
RNFL thick.	12.2 (13.4)	8.7 (10.0)	9.9 (10.2)	7.5 (7.5)
	Reproducibility			
	Iowa		*Our*	
	RMSE (µm)	**MUD** (µm)	**RMSE** (µm)	**MUD** (µm)
Vitre.-RNFL	5.1	3.8	3.0	2.3
RNFL-GCL	7.8	5.6	6.5	5.0
IPL-INL	6.0	4.3	5.9	4.4
RPE bound.	4.6	3.4	5.3	4.2
RNFL thick.	6.1	4.4	6.2	4.6

Table 2.7: Accuracy evaluation before (within parentheses) and after bias correction of our method and The Iowa Reference Algorithms on macular scans of healthy subjects and peripapillary scans of glaucomatous subjects excluding A-scans crossing blood vessels, ONH and undefined regions produced by The Iowa Reference Algorithms

	Macular scans			
	Iowa		*Our*	
	RMSE (µm)	**MUD** (µm)	**RMSE** (µm)	**MUD** (µm)
Vitre.-RNFL	4.1 (4.4)	3.3 (3.4)	3.2 (3.2)	2.7 (2.7)
RNFL-GCL	5.8 (6.5)	4.6 (5.0)	6.0 (6.9)	4.7 (5.5)
IPL-INL	5.8 (6.9)	4.6 (5.5)	7.4 (7.4)	5.8 (5.8)
RPE bound.	5.2 (6.7)	3.5 (5.1)	5.2 (5.2)	4.0 (4.1)
RNFL thick.	6.9 (8.3)	5.6 (6.7)	6.8 (7.6)	5.3 (5.9)
	Peripapillary scans			
	Iowa		*Our*	
	RMSE (µm)	**MUD** (µm)	**RMSE** (µm)	**MUD** (µm)
Vitre.-RNFL	4.5 (6.7)	3.5 (5.0)	4.7 (4.7)	3.2 (3.7)
RNFL-GCL	8.6 (10.6)	6.5 (7.7)	8.5 (11.5)	6.2 (8.6)
IPL-INL	9.2 (9.4)	5.9 (6.3)	5.3 (5.7)	4.5 (4.5)
RPE bound.	5.1 (5.6)	3.8 (4.0)	5.2 (5.2)	4.2 (4.2)
RNFL thick.	9.1 (11.9)	7.0 (9.1)	9.7 (11.9)	7.2 (9.1)

References

[1] D. Pascolini and S. P. Mariotti, *Global estimates of visual impairment: 2010,* British Journal of Ophthalmology **96**, 614 (2012).

[2] S. West and A. Sommer, *Prevention of blindness and priorities for the future,* Bulletin of the World Health Organization **79**, 244 (2001).

[3] D. Huang, E. A. Swanson, C. P. Lin, J. S. Schuman, W. G. Stinson, W. Chang, M. R. Hee, T. Flotte, K. Gregory, C. A. Puliafito, and et al., *Optical coherence tomography,* Science **254**, 1178 (1991).

[4] Y. Huang, A. V. Cideciyan, G. I. Papastergiou, E. Banin, S. L. Semple-Rowland, A. H. Milam, and S. G. Jacobson, *Relation of optical coherence tomography to microanatomy in normal and rd chickens,* Investigative Ophthalmology and Visual Science **39**, 2405 (1998).

[5] D. Koozekanani, K. Boyer, and C. Roberts, *Retinal thickness measurements from optical coherence tomography using a Markov boundary model,* IEEE Transactions on Medical Imaging **20**, 900 (2001).

[6] H. Ishikawa, D. M. Stein, G. Wollstein, S. Beaton, J. G. Fujimoto, and J. S. Schuman, *Macular segmentation with optical coherence tomography,* Investigative Ophthalmology and Visual Science **46**, 2012 (2005).

[7] M. Mujat, R. Chan, B. Cense, B. Park, C. Joo, T. Akkin, T. Chen, and J. de Boer, *Retinal nerve fiber layer thickness map determined from optical coherence tomography images,* Optics Express **13**, 9480 (2005).

[8] A. Mishra, A. Wong, K. Bizheva, and D. A. Clausi, *Intra-retinal layer segmentation in optical coherence tomography images,* Optics Express **17**, 23719 (2009).

[9] A. Yazdanpanah, G. Hamarneh, B. R. Smith, and M. V. Sarunic, *Segmentation of intra-retinal layers from optical coherence tomography images using an active contour approach,* IEEE Transactions on Medical Imaging **30**, 484 (2011).

[10] K. A. Vermeer, J. van der Schoot, H. G. Lemij, and J. F. de Boer, *Automated segmentation by pixel classification of retinal layers in ophthalmic OCT images,* Biomedical Optics Express **2**, 1743 (2011).

[11] J. Novosel, K. A. Vermeer, G. Thepass, H. G. Lemij, and L. J. van Vliet, *Loosely coupled level sets for retinal layer segmentation in optical coherence tomography,* 2013 IEEE 10th International Symposium on Biomedical Imaging (ISBI) , 1010 (2013).

[12] A. Carass, A. Lang, M. Hauser, P. A. Calabresi, H. S. Ying, and J. L. Prince, *Multiple-object geometric deformable model for segmentation of macular OCT,* Biomedical Optics Express **5**, 1062 (2014).

[13] Q. Yang, C. A. Reisman, Z. Wang, Y. Fukuma, M. Hangai, N. Yoshimura, A. Tomidokoro, M. Araie, A. S. Raza, D. C. Hood, and K. Chan, *Automated layer segmentation of macular OCT images using dual-scale gradient information,* Optics Express **18**, 21293 (2010).

[14] O. Tan, G. Li, A. T. Lu, R. Varma, and D. Huang, *Mapping of macular substructures with optical coherence tomography for glaucoma diagnosis,* Ophthalmology **115**, 949 (2008).

[15] M. Baroni, P. Fortunato, and A. La Torre, *Towards quantitative analysis of retinal features in optical coherence tomography,* Medical Engineering and Physics **29**, 432 (2007).

[16] S. J. Chiu, X. T. Li, P. Nicholas, C. A. Toth, J. A. Izatt, and S. Farsiu, *Automatic segmentation of seven retinal layers in SD-OCT images congruent with expert manual segmentation,* Optics Express **18**, 19413 (2010).

[17] J. Y. Lee, S. J. Chiu, P. P. Srinivasan, J. A. Izatt, C. A. Toth, S. Farsiu, and G. J. Jaffe, *Fully automatic software for retinal thickness in eyes with diabetic macular edema from images acquired by Cirrus and Spectralis systems,* Investigative Ophthalmology and Visual Science **54**, 7595 (2013).

[18] M. K. Garvin, M. D. Abramoff, X. Wu, S. R. Russell, T. L. Burns, and M. Sonka, *Automated 3D intraretinal layer segmentation of macular spectral-domain optical coherence tomography images,* IEEE Transactions on Medical Imaging **28**, 1436 (2009).

[19] P. A. Dufour, L. Ceklic, H. Abdillahi, S. Schroder, S. De Dzanet, U. Wolf-Schnurrbusch, and J. Kowal, *Graph-based multi-surface segmentation of OCT data using trained hard and soft constraints,* IEEE Transactions on Medical Imaging **32**, 531 (2013).

[20] B. J. Antony, M. D. Abramoff, M. M. Harper, W. Jeong, E. H. Sohn, Y. H. Kwon, R. Kardon, and M. K. Garvin, *A combined machine-learning and graph-based framework for the segmentation of retinal surfaces in SD-OCT volumes,* Biomedical Optics Express **4**, 2712 (2013).

[21] K. Li, X. D. Wu, D. Z. Chen, and M. Sonka, *Optimal surface segmentation in volumetric images - A graph-theoretic approach,* IEEE Transactions on Pattern Analysis and Machine Intelligence **28**, 119 (2006).

[22] A. Fuller, R. Zawadzki, S. Choi, D. Wiley, J. Werner, and B. Hamann, *Segmentation of three-dimensional retinal image data,* IEEE Transactions on Visualization and Computer Graphics **13**, 1719 (2007).

[23] M. A. Mayer, J. Hornegger, C. Y. Mardin, and R. P. Tornow, *Retinal nerve fiber layer segmentation on FD-OCT scans of normal subjects and glaucoma patients,* Biomedical Optics Express **1**, 1358 (2010).

[24] R. Kafieh, H. Rabbani, M. D. Abramoff, and M. Sonka, *Intra-retinal layer segmentation of 3D optical coherence tomography using coarse grained diffusion map,* Medical Image Analysis **17**, 907 (2013).

[25] A. Lang, A. Carass, M. Hauser, E. S. Sotirchos, P. A. Calabresi, H. S. Ying, and J. L. Prince, *Retinal layer segmentation of macular OCT images using boundary classification,* Biomedical Optics Express **4**, 1133 (2013).

[26] J. A. Bogovic, J. L. Prince, and P. L. Bazin, *A multiple object geometric deformable model for image segmentation,* Computer Vision and Image Understanding **117**, 145 (2013).

[27] R. Kafieh, H. Rabbani, and S. Kermani, *A review of algorithms for segmentation of optical coherence tomography from retina,* Journal of Medical Signals and Sensors **3**, 45 (2013).

[28] D. C. DeBuc, *A review of algorithms for segmentation of retinal image data using optical coherence tomography,* in *Image Segmentation*, edited by P.-G. Ho (2011) pp. 15–54.

[29] K. A. Vermeer, J. Mo, J. J. Weda, H. G. Lemij, and J. F. de Boer, *Depth-resolved model-based reconstruction of attenuation coefficients in optical coherence tomography,* Biomedical Optics Express **5**, 322 (2013).

[30] B. Braaf, K. A. Vermeer, V. A. Sicam, E. van Zeeburg, J. C. van Meurs, and J. F. de Boer, *Phase-stabilized optical frequency domain imaging at 1-micron for the measurement of blood flow in the human choroid,* Optics Express **19**, 20886 (2011).

[31] S. H. Yun, G. J. Tearney, B. E. Bouma, B. H. Park, and J. F. de Boer, *High-speed spectral-domain optical coherence tomography at 1.3 mu m wavelength,* Optics Express **11**, 3598 (2003).

[32] G. M. P. van Kempen, N. van den Brink, L. J. van Vliet, M. van Ginkel, P. W. Verbeek, and H. Blonk, *The application of a local dimensionality estimator to the analysis of 3D microscopic network structures,* in *in: SCIA'99, Proceedings of the 11th Scandinavian Conference on Image Analysis* (1999) pp. 447–455.

[33] E. W. Dijkstra, *A note on two problems in connexion with graphs,* Numerische Mathematik **1**, 269 (1959).

[34] A. F. Frangi, W. J. Niessen, K. L. Vincken, and M. A. Viergever, *Multiscale vessel enhancement filtering,* in *Medical Image Computing and Computer-Assisted Interventation — MICCAI'98*, Lecture Notes in Computer Science, Vol. 1496, edited by W. Wells, A. Colchester, and S. Delp (Springer Berlin Heidelberg, 1998) Chap. 14, pp. 130–137.

[35] P. Bakker, L. J. van Vliet, and P. W. Verbeek, *Edge preserving orientation adaptive filtering,* in *Computer Vision and Pattern Recognition, 1999. IEEE Computer Society Conference on.*, Vol. 1 (1999) pp. 535–540.

[36] H. Knutsson and C. F. Westin, *Normalized and differential convolution,* in *Computer Vision and Pattern Recognition, 1993. Proceedings CVPR '93., 1993 IEEE Computer Society Conference on* (1993) pp. 515–523.

[37] C. van Wijk, R. Truyen, R. E. van Gelder, L. J. van Vliet, and F. M. Vos, *On normalized convolution to measure curvature features for automatic polyp detection,* Medical Image Computing and Computer-Assisted Intervention - Miccai 2004, Pt 1, Proceedings **3216**, 200 (2004).

[38] S. Osher and J. A. Sethian, *Fronts propagating with curvature-dependent speed - Algorithms based on Hamilton-Jacobi formulations,* Journal of Computational Physics **79**, 12 (1988).

[39] H. K. Zhao, T. Chan, B. Merriman, and S. Osher, *Variational level set approach to multiphase motion,* Journal of Computational Physics **127**, 179 (1996).

[40] T. Brox and J. Weickert, *Level set segmentation with multiple regions,* IEEE Transactions on Image Processing **15**, 3213 (2006).

[41] A. R. Mansouri, A. Mitiche, and C. Vazquez, *Multiregion competition: A level set extension of region competition to multiple region image partitioning,* Computer Vision and Image Understanding **101**, 137 (2006).

[42] L. A. Vese and T. F. Chan, *A multiphase level set framework for image segmentation using the Mumford and Shah model,* International Journal of Computer Vision **50**, 271 (2002).

[43] R. Courant, K. Friedrichs, and H. Lewy, *On the partial difference equations of mathematical physics,* IBM Journal of Research and Development **11**, 215 (1967).

[44] M. D. Abramoff, M. K. Garvin, and M. Sonka, *Retinal imaging and image analysis,* Biomedical Engineering, IEEE Reviews in **3**, 169 (2010).

[45] K. A. Vermeer, J. van der Schoot, H. G. Lemij, and J. F. de Boer, *RPE-normalized RNFL attenuation coefficient maps derived from volumetric OCT imaging for glaucoma assessment,* Investigative Ophthalmology and Visual Science **53**, 6102 (2012).

3

Joint segmentation of retinal layers and focal lesions in 3D OCT data of topologically disrupted retinas

This chapter is based on the manuscript:

J. Novosel, K. A. Vermeer, J. H. de Jong, Z. Wang and L. J. van Vliet, *Joint segmentation of retinal layers and focal lesions in 3D OCT data of topologically disrupted retinas*, IEEE Transactions on Medical Imaging, accepted (2017).

Abstract

Accurate quantification of retinal structures in 3D optical coherence tomography data of eyes with pathologies provides clinically relevant information. We present an approach to jointly segment retinal layers and lesions in eyes with topology-disrupting retinal diseases by a loosely coupled level set framework. In the new approach, lesions are modelled as an additional space-variant layer delineated by auxiliary interfaces. Furthermore, the segmentation of interfaces is steered by local differences in the signal between adjacent retinal layers, thereby allowing the approach to handle local intensity variations. The accuracy of the proposed method of both layer and lesion segmentation has been evaluated on eyes affected by central serous retinopathy and age-related macular degeneration. Additionally, layer segmentation of the proposed approach was evaluated on eyes without topology-disrupting retinal diseases. A good agreement between the segmentation performed manually by a medical doctor and results obtained from the automatic segmentation was found for all data types. The mean unsigned error for all interfaces varied between 2.3 and 11.9 μm *(0.6 - 3.1 pixels). Furthermore, lesion segmentation showed a Dice coefficient of 0.68 for drusen and 0.89 for fluid pockets. Overall, the method provides a flexible and accurate solution to jointly segment lesions and retinal layers.*

3.1. Introduction

Optical coherence tomography (OCT) is a non-invasive, non-contact imaging technique that can be used to acquire in-vivo images of retinal structures [1]. Its high resolution enables the investigation of the retinal tissue layers and pathological changes. In various eye diseases, the thickness of one or more retinal layers is affected. For example, degeneration of the *retinal nerve fiber layer* (*RNFL*) occurs in glaucoma patients [2], whereas the *ganglion cell complex* (*GCC*) gets thinner in patients with age-related macular degeneration (AMD) [3]. Furthermore, changes in the properties of a tissue that composes a layer occur. For example, in patients with glaucoma, the OCT signal and OCT derived attenuation coefficient values of the *RNFL* were shown to be reduced when compared to healthy subjects [4], whereas in patients with central serous retinopathy (CSR), changes in reflectivity of the *outer nuclear layer* (*ONL*) were encountered [5, 6]. Finally, certain pathologies may give rise to additional structures that are not present in the retinas of healthy subjects. In dry AMD, small deposits of extracellular tissue, called drusen, form within the retina. In CSR, the build-up of fluid in the sub-retinal space creates a fluid pocket that disrupts the outer retinal layers. In diabetic macular edema (DME), retinal cysts may form inside inner and outer retinal layers.

Accurate quantification of retinal structures, both layers and lesions, provides clinically relevant information about the retina. Extraction of these imaging biomarkers has become an important task as it enables valuable input for diagnostics, prognostics, and monitoring of retinal diseases. When done manually, this is a potentially subjective and time-consuming job due to the required precision and large data volumes. Hence, an objective and automated tool that extracts clinically useful information, such as the thickness of layers and the presence or extent of emerging pathologies, is needed.

This need for segmentation of retinal layers and lesions has been recognized before. However, most existing approaches focus either on extracting information about a specific lesion in the diseased retina [7–12] or on segmenting the retinal layers in healthy retinas [13–19] and retinas affected by a disease such as glaucoma that merely results in thinning of a certain layer without any serious layer deformation [20–27]. By segmenting only retinal lesions without retinal layer segmentation, other potentially valuable clinical information about the retina is ignored.

Automatic segmentation of the both retinal layers and lesions that may exist in pathological retinas, such as sub-retinal fluid, drusen and cysts, remains a challenging task as the presence of lesions can cause large disruptions of the retina. First, the topology and morphology of the retina may be affected. Second, the lesions vary largely in size, shape and location. Third, the OCT intensity of one or more layers may vary considerably within a scan. Some of the mentioned segmentation challenges are indicated in Figure 3.1, where a typical B-scan of an eye affected by CSR and one of an eye affected by AMD are shown. Finally, all the aforementioned changes in the retina may violate the use of strong prior knowledge on the intensity and thickness of the layers.

A few approaches have been presented to segment both the retinal layers and lesions [11, 17, 28–37], but only three of these approaches have evaluated the

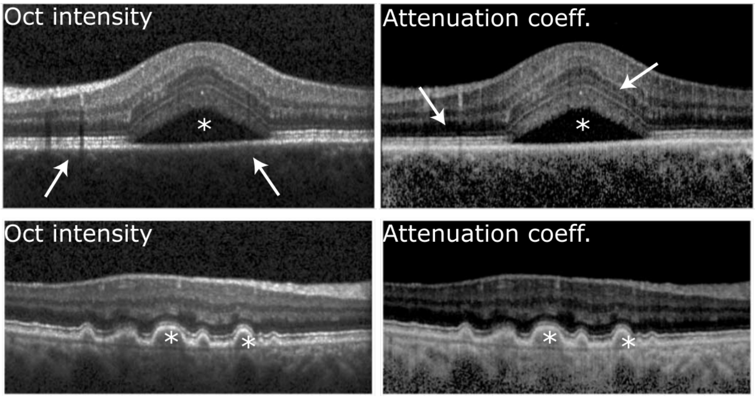

Figure 3.1: The intensity of a retinal OCT B-scan and the estimated attenuation coefficient of a patient suffering from CSR (top row) and AMD (bottow row). The arrows point to areas where variations in either the layer's intensity or the attenuation coefficients occur. The asterisks mark the location of the lesions, i.e. the fluid pocket in CSR and drusen in AMD.

accuracy of both layer and lesion segmentation [29, 31, 32]. Quellec et al. and Chiu et al. employed a machine learning approach to segment layers and lesions in exudative AMD [31] and DME data [29], respectively. Because these two methods are based on a machine learning approach, they might be difficult to interpret and improve as well as adapt to other retinal diseases. Indeed, the extension of machine learning approaches for retinal layer segmentation to other types of retinal diseases were already reported to be highly dependent on the training dataset [13]. Furthermore, Shi et al. searched for a disease specific footprint by utilizing the distance between two retinal surfaces and several empirically determined thresholds [32] to segment lesions and retinal layers in data of retinas affected by serous pigment epithelium detachment. Finally, in all three approaches, the lesion and layers are segmented in a sequential manner. Thus, segmentation errors that occur in the first step may propagate into the second step without the possibility to correct them.

In this paper, we present an approach to jointly segment retinal layers and lesions in eyes with topology-disrupting retinal diseases. The problem is expressed in the framework of loosely coupled level set (LCLS), previously developed for the simultaneous segmentation of interfaces between retinal layers in macular and peripapillary scans of healthy subjects and glaucoma patients [27]. The new approach extends and generalizes the existing one, as it can handle local intensity variations as well as the presence or absence of pathological structures in the retina [38],[39]. In our framework, lesions are modelled as an additional space-variant layer delineated by auxiliary interfaces. When a lesion is not present, these additional layer will have (near) zero thickness. Furthermore, the segmentation of interfaces is steered by local differences in signal between adjacent retinal layers thereby allowing the approach to handle local intensity variations. The method was evaluated on patients suffering from either CSR or AMD: two topology-disrupting retinal diseases. The results of both layer and lesion segmentation are presented. Seven interfaces were considered: the *vitreous - RNFL*, the *RNFL - GCL*, the *IPL - INL*, the *INL - OPL*, the *OPL - ONL*, the *IS ellipsoid* and the *posterior RPE boundary*. In AMD patients, in addition to the aforementioned interfaces, *Bruch's membrane* was segmented. A complete description of the layers and their definitions is given in Figure 3.2.

3.2. Method for joint retinal layer and lesion segmentation

The proposed segmentation framework performs the joint segmentation of interfaces between retinal layers and lesions. It operates on attenuation coefficient maps, which are derived from in-vivo human retinal OCT data [40]. The interfaces are simultaneously segmented by utilizing image data and anatomical knowledge about the retina, such as the predefined order of its layers. The framework consists of several processing steps including conversion to attenuation coefficients, retinal feature detection, noise suppression as well as the actual joint layer and lesion segmentation method. First, we briefly introduce the conversion to attenuation coefficients (3.2.1) and the LCLS framework (3.2.2). Then, we present generalizations to the framework to deal with segmentation challenges present in the eyes of CSR and AMD patients such as the local variation in estimated attenuation coefficients within layers (3.2.3) and the presence of space-variant lesions (3.2.4). Finally, we provide implementation details on the segmentation of lesions (3.2.5) as well as on the initialization of the joint segmentation approach (3.2.6), the selection of parameter values (3.2.7) and the dataset that was used in the evaluation (3.2.8).

3.2.1. Attenuation coefficient

The intensities of the raw OCT data were transformed into attenuation coefficients [40]. The attenuation coefficient is an optical property of a tissue and as such illumination invariant. Therefore, various artefacts that are common in OCT images, such as intensity fluctuation within layers, are largely reduced. Examples of B-scans from eyes affected by CSR and AMD before and after conversion to attenuation coefficients are shown in Figure 3.1. As can be seen from the Figure, the eye affected by CSR shows large local changes in the estimated attenuation coefficients of several layers in the area of the fluid pocket.

Afterwards, retinal features (blood vessels and rough estimation of the inner and outer boundaries that surround the retina) were detected and a structure-driven anisotropic Gaussian filter, to suppress the noise in the data, was applied. Finally, the developed layer segmentation method, was applied to the filtered data.

3.2.2. Loosely coupled level sets

The LCLS framework employs a probabilistic approach, which incorporates image data and prior knowledge of the retina to segment the interfaces between retinal layers. Every interface C_i is represented by its own level set function ϕ_i, which is propagated according to:

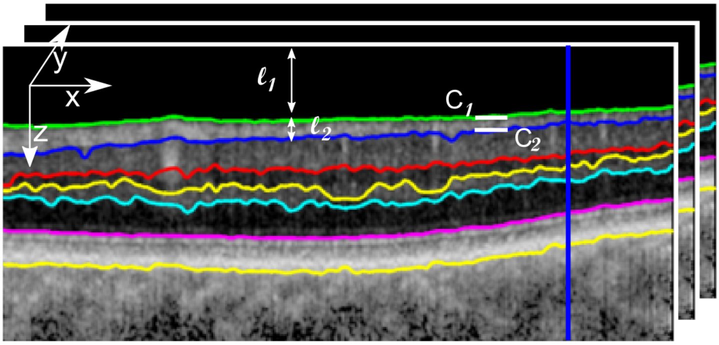

Figure 3.2: The segmentation results obtained with the LCLS method on a 3D retina composed of consecutive B-scans of attenuation coefficients. The full names of the segmented retinal layers and their abbreviations are as follows (from the top of the image): *vitreous*; *retinal nerve fiber layer* (*RNFL*); *ganglion cell layer* (*GCL*) with *inner plexiform layer* (*IPL*); *inner nuclear layer* (*INL*); *outer plexiform layer* (*OPL*); *outer nuclear layer* (*ONL*); *inner segment* (*IS*) with *outer segment* (*OS*); *retinal pigment epithelium* (*RPE*); *choroid*. The blue line indicates an A-scan. The 3D coordinate system is indicated with arrows in the top left corner. Notations used for layers (l_1,l_2) and interfaces (C_1,C_2) in the segmentation framework are shown with white letters.

$$\frac{\partial \phi_i}{\partial t} = -\Delta t \left((Pr(l_i|\mu) - 0.5) + \alpha \kappa_i + \beta \zeta_i \right) |\nabla \phi_i|, \tag{3.1}$$

where $Pr(l_i|\mu)$ is the probability of a pixel belonging to layer l_i given the attenuation coefficient μ of that pixel, and κ_i and ζ_i the geometric regularization terms. The weights of the terms are denoted by α and β, while Δt is the time step.

The probabilistic term expresses the posterior probability of pixels along an interface belonging to the retinal layer above the interface (l_i) as:

$$Pr(l_i|\mu) = \frac{Pr(\mu|l_i)Pr(l_i)}{\sum_{j\in\{i,i+1\}} Pr(\mu|l_j)Pr(l_j)} \tag{3.2}$$

where $Pr(\mu|l_i)$ is the likelihood based on the available image data inside the set Ω_i containing all pixels assigned to layer l_i, and $Pr(l_i)$ is the prior for layer l_i. The prior probability combines prior knowledge on the attenuation coefficient values and on the order of the layers and their thickness. Finally, the probability density function $Pr(\mu|l_i)$ can be approximated by the normalized histogram $Pr(\mu|\Omega_i)$ of all pixels assigned to layer l_i.

Figure 3.2 shows an example of the segmentation results obtained with our original approach on the scan of a healthy subject as well as some used terminology including the coordinate system composed of the axial, the fast lateral and the slow lateral scanning axes in the z, x and y direction, respectively. Although our original approach performed well on healthy and glaucoma affected eyes, some of its assumptions are problematic when applied to eyes with topology-disrupting pathologies. In some cases, the layers are no longer homogeneous but show large attenuation coefficient variations, which affects both the likelihood estimation as

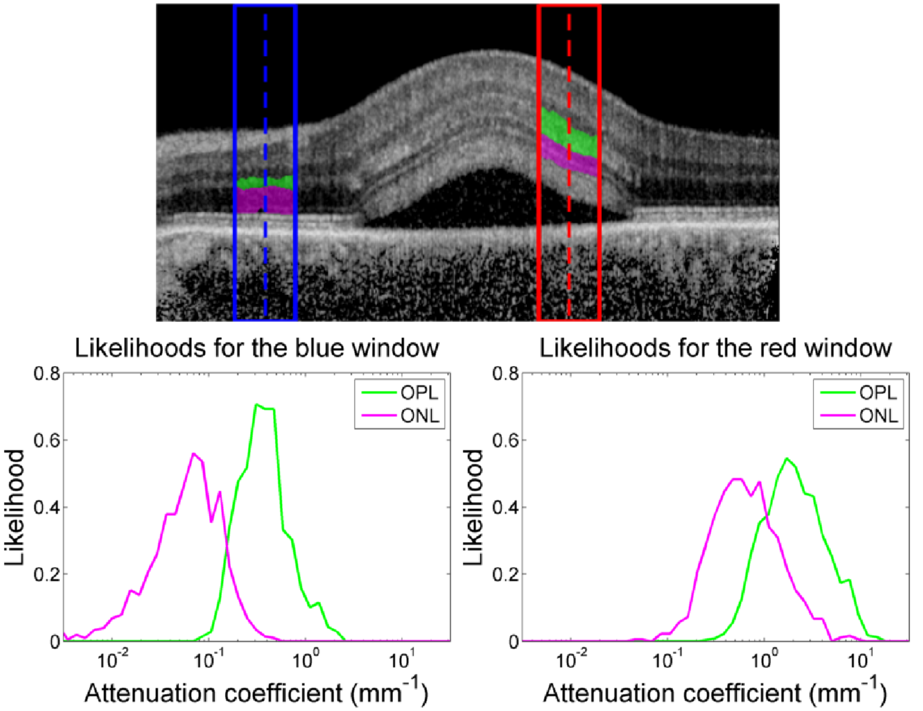

Figure 3.3: An example of a difference in the estimated attenuation coefficient values within layers by examination of the local likelihoods (window width set to 565 μm, i.e. 50 pixels) for layers surrounding the *OPL-ONL* interface at two different locations. Although the likelihoods of the two layers vary considerably for different locations, the contrast remains present (the *OPL* remains brighter than the *ONL*).

well as the use of prior knowledge. Furthermore, the presence of lesions impacts both the topology and morphology of the retina.

3.2.3. Locally adaptive likelihood

The original LCLS framework globally optimizes the segmentation of all interfaces by exploiting the differences in the attenuation coefficients between both sides of an interface across the whole volume. At every iteration of the level set propagation, histograms of the attenuation coefficients are derived for each layer and from them the likelihood of pixels along an interface belonging to each of the adjacent layers is determined.

As already mentioned, some eyes with pathologies show abrupt local changes in the estimated attenuation coefficients within a layer. This clearly violates the assumption of homogeneous layers and makes a global approach no longer viable. However, differences in the estimated attenuation coefficients between both sides of an interface remain largely preserved on a local scale. Figure 3.3 shows an example of variations in the estimated attenuation coefficient within layers for two different locations in a B-scan image.

Hence, we propose to exploit these local differences by setting a window of interest around every A-scan and computing normalized histograms from values within that window instead of considering entire layers. For every A-scan, a rectangular window, as indicated in Figure 3.3, with a certain width (described in more details in section 3.2.7) and a height that extends over the entire image height was taken. The window then slides from one side of an image to the other side. To compute the local histogram of a certain layer for a specific A-scan, only data points that belong to that layer and are within the window of interest are considered.

The computed local histograms now model the likelihoods for observing certain attenuation coefficient values within layers surrounding an interface, but are constrained to the region of interest. This is achieved by making the probability $Pr(\mu|\Omega_i)$ dependent on the lateral position within a volume and by replacing it with $Pr(\mu|\Omega_i, x, y)$. Similarly, the probability $Pr(\mu|\Omega_{i+1})$ also becomes location dependent $Pr(\mu|\Omega_{i+1}, x, y)$. This enables the calculation of the posterior probability in equation 3.2, which is replaced by $Pr(l_i|\mu, x, y)$, on a local scale.

3.2.4. Lesion modeling

Lesions, can be contained within a single layer, such as abnormal fluid pockets (e.g. subretinal fluid in CSR), and drusen in dry AMD, or can extend over multiple retinal layers, such as retinal cysts (e.g. intra-retinal cysts in CME). If lesions are contained within a certain layer they could be regarded as an additional layer present within the retina. As the LCLS framework allows segmentation of an arbitrary number of layers, we propose to model lesions as an additional layer.

Auxiliary interfaces are introduced to delineate the top and bottom boundary of the lesion if it is contained within a certain layer. If one of the boundaries of the lesion coincides with an interface between retinal layers, then a single auxiliary interface is introduced. These auxiliary interfaces are then propagated according to equation 3.1 based on image data and anatomical knowledge about the retina. Although the topology of the retina has changed in these eyes, if lesions are contained within another retinal layer, the anatomical knowledge about the predefined order of the retinal layers can still be utilized in the same way as in the original framework.

From the auxiliary interfaces, the segmentation of the lesion is obtained. In the absence of a lesion, the additional layer will have a near-zero thickness. As such, the proposed approach provides information about the presence of a lesion as well as its spatial extent.

3.2.5. Lesion segmentation

In CSR, fluid accumulates above the *RPE* and creates a subretinal fluid pocket. In our framework, this fluid is modelled as an additional layer present within another retinal layer surrounded by the *IS ellipsoids* and the *posterior RPE boundary*. Hence, two auxiliary interfaces are introduced. These auxiliary interfaces are propagated according to equation 3.1 by utilizing the difference in the estimated attenuation coefficient values of the surrounding layers and prior knowledge. Prior knowledge about the order of layers was enforced such that the fluid is contained between the

IS ellipsoids and the *posterior RPE boundary*. However, no prior knowledge on the thickness of the fluid pocket was imposed. Furthermore, prior knowledge about the attenuation coefficient values on either side an the auxiliary interface is described in section 3.2.7. As mentioned, in areas and scans without lesions, the additional layer may shrink to a near zero thickness. In practice, the layer had a thickness varying between 0 - 3.9 µm, i.e. less than one pixel. Therefore, a thickness of less than 3.9 µm was interpreted to indicate that no lesion was present at that location.

In AMD, disruption of the *RPE* occurs and extracellular material starts to accumulate resulting in the formation of drusen. As a result of this disruption, *Bruch's membrane* becomes separated from the *posterior RPE boundary*. However, the membrane is only visible below the drusen, whereas in areas and eyes without drusen it remains adjacent to the *posterior RPE boundary* and cannot be discerned. Therefore, drusen can be considered as a layer between the *posterior RPE boundary* and *Bruch's membrane*. As one of the boundaries of drusen coincides with an interface between retinal layers, only one auxiliary interface is introduced which corresponds to the *Bruch's membrane*. The segmentation of *Bruch's membrane* is frequently obtained by taking a convex envelope of the *posterior RPE boundary* [7, 9, 41]. All elevation of the *posterior RPE boundary* higher that 20 µm [42, 43] and larger than 25 µm in diameter (as determined by the age-related eye disease study [44]) are regarded as drusen.

3.2.6. Initialization

Propagation of the level set functions is done by simultaneously solving the set of partial differential equations that drive the current segmentation of the retinal interfaces to its minimum energy state. The initialization stage of the segmentation framework, that isbased on a minimum cost path search [45] and that is applied to individual B-scans, was adapted to accommodate the possible presence of lesions. The cost function for the *posterior RPE boundary* was modified and instead of initializing the *OPL-ONL* interface, the *IS ellipsoid boundary* was initialized. Two additional nodes with zero cost, that connect each pixel in the first and the last A-scans were added, to make the initialization process fully automatic.

The *RPE* is primarily a horizontal layer. However, in eyes affected by dry AMD, drusen appear as vertical elevations of the *posterior RPE boundary* and the *RPE* is no longer approximately horizontal. Our previously used cost function for the *posterior RPE boundary* was based on the derivative in the z-direction (as the *RPE* was horizontal). Due to vertical changes in the *RPE*, our new approach also included the derivative in x-direction in the cost function (f_c), which was defined as follows:

$$f_c = \left(1 - \frac{g_z * I}{\max(g_z * I)}\right) + \left(1 - \frac{\mathrm{abs}(g_x * I)}{\max(\mathrm{abs}(g_x * I))}\right) \tag{3.3}$$

where I stand for a B-scan, g_z and g_x are Gaussian derivatives in the z- and x-direction, respectively. For other interfaces (the *vitreous-RNFL* and *IS ellipsoid boundary*), only the derivative in the z-direction is considered and the cost function is defined as follows: $f_c = 1 - \frac{g_z * I}{\max(g_z * I)}$. The initialization was performed in a sequential manner, by first initializing the *posterior RPE boundary*. Then, the *vitreous-RNFL* interface was initialized by limiting the search region to the area above the *posterior RPE boundary*. Finally, the *IS ellipsoid boundary* was found by limiting the search area to the region bounded by the *vitreous-RNFL* interface and the *posterior RPE boundary*.

The rest of the retina was initialized based on reported population-average thicknesses of retinal layers [46]. Furthermore, the two auxiliary interfaces around the lesions in CSR data were initialized to be 20 μm below the *IS ellipsoid boundary* and 20 μm above the *posterior RPE boundary*.

3.2.7. Parameter selection

As mentioned before, our LCLS approach combines a data-driven segmentation with prior knowledge about the retina. The prior knowledge on the thickness of layers remains the same as in our original approach, whereas the prior knowledge on the attenuation coefficients was changed for three interfaces.

The priors on the estimated attenuation coefficients were modelled as an error function ($Pr(\mu'|l_i) = \gamma\,\mathrm{erf}\left(\frac{\log(\mu)-\log(\mu_c)}{\sigma}\right) + 0.5$) governed by three parameters that controlled the threshold (μ_c), slope (σ) and magnitude (γ) of the prior probability. As some of the layers showed large variations in their estimated attenuation coefficients, the imposed prior was relaxed by reducing the slope of the prior probability. The parameter that controlled the slope was changed from a value of 2 mm to a value of 4 mm for the *OPL-ONL* interface and the *IS ellipsoids*. Additionally, two priors on attenuation coefficients were introduced for the two auxiliary interfaces. The slope of these priors was set to 1 mm, the threshold to 0.4 mm^{-1} and the magnitude to 0.45 and -0.45 for the top and bottom boundary of the lesion, respectively. Finally, in the used publicly available dataset of retinal scans of AMD patient [47], the *RPE* was shown to have lower attenuation coefficient values. Therefore, the threshold on the *posterior RPE boundary* for the scans from the publicaly available dataset was changed to 5.0 mm^{-1}. For the rest of the data (obtained in Rotterdam Eye Hospital), this lower threshold caused parts of the *choroid* to be segmented as part of the *RPE*, thus the threshold remained as it was in our original approach (12.75 mm^{-1}).

Another parameter that needed to be set was the window size for the local histogram calculation. The size of the window needs be large enough to provide sufficient data points for a reliable likelihood estimation and small enough to adapt to changes in the attenuation coefficients. Window sizes up to 565 μm (i.e., 50 pixels) were small enough to capture changes occurring in the estimated attenuation coefficient values of the *ONL* and *IS ellipsoids* (the two layers with the largest variation in the estimated attenuation coefficients). As a smaller window size might not provide meaningful data, a window size of 565 μm was used.

Finally, in the noise suppression step, images were smoothed by using an adaptive 1D Gaussian filter [48] along the orientation obtained from the 2D structure tensor [49]. The previously used scale for filtering was $\sigma = 32$ μm. As this scale may smooth away small drusen, it was reduced to $\sigma = 16$ μm. The smaller scale is in accordance with the standard drusen classification (according to the age-related eye disease study, drusen are all elevation of *RPE* larger than 25 μm in diameter) and will ensure that such structures will not be suppressed.

3.2.8. Data

Volumetric macular OCT scans from 25 patients (one eye per patient) suffering from CSR were obtained from an ongoing CSR study in the Rotterdam Eye Hospital (Rotterdam, the Netherlands). The scans of this dataset were acquired with a Spectralis SD-OCT system (Heidelberg Engineering, Germany) with a field of view of $20°\text{x}20°$. The scan protocol combined 97 B-scans composed of 512 A-scans of 496 pixels into one volume. The recorded data was strongly anisotropically sampled with a voxel spacing of approximately 3.9 x 11.3 x 60.2 mm^3 in the z, x and y direction, respectively. The system employed an eye-tracker and was set to average 5 B-scans before moving to the next B-scan.

Volumetric macular OCT scans from ten patients (one eye per patient) suffering from AMD were obtained from a publicly available dataset [47]. The scans were also acquired with a Spectralis OCT system, however the raw OCT was not available. Instead, the dataset contained images exported in a tagged image file format. It remains unclear what causes the lower attenuation coefficients of the *RPE* within this dataset. For more details on the used scan protocols, we refer the reader to [47].

For the AMD patients and five CSR patients, two B-scans with lesions were randomly selected from each volumetric scan for manual annotation. For the remaining CSR patients, one B-scan with lesions was randomly selected. Manual segmentation was done on a slice-by-slice basis by a medical doctor using ITK-SNAP (publicly available at `http://www.itksnap.org`). In data from CSR patients, the expert was asked to delineate the fluid boundaries and the following interfaces: the *vitreous - RNFL*, *RNFL - GCL*, *IPL - INL*, *INL - OPL* and *OPL - ONL* interface as well as the *IS ellipsoids* and *posterior RPE boundary* in data from CSR patients. In data from AMD patients, in addition to the aforementioned interfaces, the expert was asked to delineate *Bruch's membrane*.

3.3. Experiments and results

A quantitative evaluation was done to assess the accuracy of the presented method. Four sets of experiments were performed. In the first experiment, the accuracy of the method to segment eyes with topology disrupting pathologies was evaluated on data described in section 3.2.8. In the second experiment, the accuracy of the presented method was evaluated on the same dataset that was used in the original LCLS paper [27] to assess the performance of the proposed method on eyes without topologically disrupting pathologies. In the third experiment, we illustrate how the proposed framework could be applied to obtain segmentation of retinal layers and cysts in a patient suffering from DME and present the obtained results. The final experiment was performed to evaluate the accuracy of ”The Iowa Reference Algorithms” [28, 50, 51] on our dataset.

For every interface, the accuracy was determined by measuring the distance between manually and automatically segmented interfaces. Both signed and un-

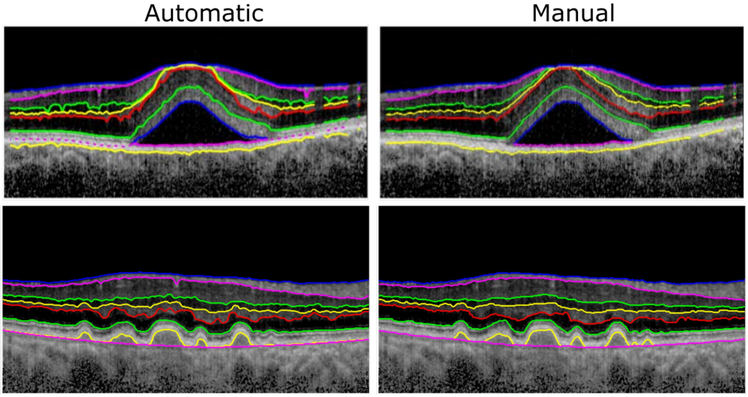

Figure 3.4: Examples of automatic and manual layer and lesion segmentation on a B-scan from a patient suffering from CSR (top row) and AMD (bottom row).

signed distances were computed for every A-scan and then averaged, resulting in the mean-signed-error (MSE) and the mean-unsigned-error (MUE). The accuracy of lesion segmentation was determined by examining the overlap between manually and automatically segmented lesions. The Dice coefficient, true positive rate (TPR) and false positive rate (FPR) were considered. These measurements were computed for every lesion. A-scans crossing the retinal vasculature were excluded in calculating the errors as the blood vessels interrupt the normal appearance of the layers and it is unclear to which layer these vessels belong to.

Table 3.1: Accuracy evaluation of the automatic layer segmentation in diseased eyes. Mean signed (MSE) and unsigned error (MUE) with corresponding standard deviations are reported.

	CSR		*AMD*	
	MSE (μm)	**MUE** (μm)	**MSE** (μm)	**MUE** (μm)
Vit.-RNFL	-3.4 ± 3.6	3.9 ± 3.0	-2.6 ± 9.3	4.2 ± 8.7
RNFL-GCL	-0.0 ± 12.0	6.5 ± 10.1	-3.7 ± 13.1	6.9 ± 11.7
IPL-INL	2.9 ± 14.8	10.1 ± 11.3	-1.1 ± 17.4	9.0 ± 14.9
INL-OPL	-9.4 ± 16.6	11.8 ± 15.0	-3.9 ± 14.8	9.3 ± 12.1
OPL-ONL	-4.9 ± 19.9	11.9 ± 16.8	-9.4 ± 17.1	11.5 ± 15.7
IS ellip.	0.8 ± 14.5	7.4 ± 12.5	1.9 ± 15.3	4.9 ± 14.5
RPE bou.	2.9 ± 8.1	6.2 ± 5.9	3.6 ± 19.6	8.3 ± 18.2
Bruch m.	n/a	n/a	1.8 ± 11.3	7.9 ± 8.1

3.3.1. Accuracy evaluation on retinas with topology-disrupting pathologies

The main evaluation of the presented segmentation method was done on macular scans of eyes affected by CSR and AMD. The scans of 25 subjects for CSR and 10 subjects for AMD (one eye per subject) were used to estimate the accuracy of the method.

Examples of a manual annotation and an automatic segmentation of both layers and lesions obtained on a CSR and an AMD patient are shown in Figure 3.4. Further, Table 3.1 provides detailed results on the accuracy of the automatic method for layer segmentation. An error of 3.9 µm corresponds to one pixel along the recorded A-scans. The accuracy of layer segmentation showed a MSE ranging from -9.4 µm to 3.6 µm and a MUE ranging from 3.9 µm to 11.9 µm. The accuracy of the lesion segmentation is given in Table 3.2. The Dice coefficient was 0.89 for fluid segmentation in CSR patients and 0.68 for drusen segmentation in AMD patients.

Additionally, Figure 3.5 shows a more detailed evaluation of the accuracy of drusen segmentation with respect to the drusen height (as determined from manual annotations). As can be seen from the figure, a good correspondence for drusen with a height larger than 60 µm is generally found. With respect to drusen with a height between 35 and 60 µm, some appear to be difficult to detect. Further, drusen with a height smaller than 35 µm are systematically missed by the automated method. Figure 3.6 shows B-scans with the best and the worst automatic drusen segmentation results when compared to manual annotation. In both images several small elevations of the *RPE*, indicated by white arrows, are missed by the automatic method. Further, in the image with the best segmentation result, although the

Table 3.2: Accuracy evaluation of the lesion segmentation.

	CSR	*AMD*
TPR	0.93	0.69
FPR	0.12	0.02
Dice	0.89	0.68

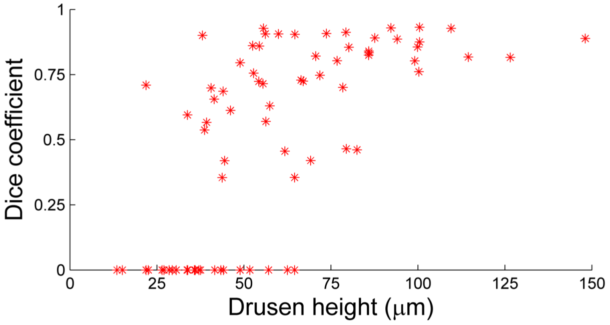

Figure 3.5: Dice coefficient of similarity with respect to the drusen height.

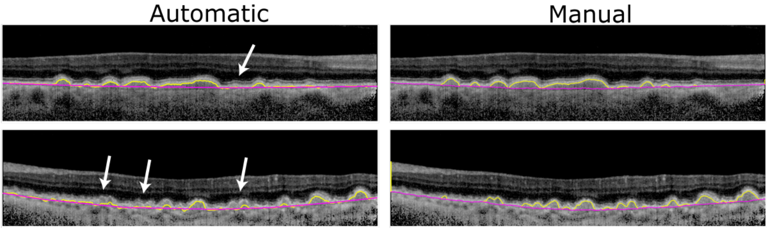

Figure 3.6: Two B-scans from different subjects with manual and automatic segmentation of boundaries defining drusen. Top row: One of the best automatic segmentation results of drusen as obtained by visual inspection. Bottom row: Visually the worst automatic segmentation result of drusen in our dataset in which some small and medium sized drusen are missed. White arrow indicate drusen missed by the automatic segmentation.

manual and automated segmentation for large drusen appear to be very similar, the Dice coefficient of similarity for these drusen is not very high, and shows an overlap of around 80%.

Finally, the obtained segmentation results could be used for visualization of retinal surfaces and 3D renderings of the retina with highlighted areas with lesions. Additional processing of the segmentation results could also be performed which offers many possibilities to show relevant clinical information in the easy to interpret method. An example are thickness maps of different layers as well as en-face images of the detected lesions. For CSR, an example of a 2D thickness map of the *ONL*, which was shown to be reduced in eyes affected by CSR, and the fluid pocket are shown in Figure 3.7. For AMD, an example of a 2D thickness map of the *GCC*, which was shown to have a reduced thickness in eyes affected by AMD, and the drusen height map are shown in Figure 3.7.

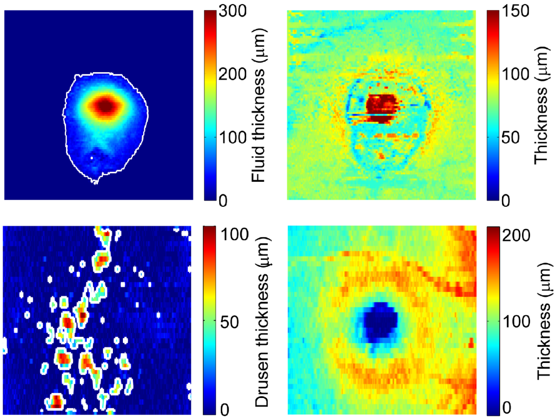

Figure 3.7: A fluid and an *ONL* thickness map for an eye suffering from CSR (top row) and a drusen and a *GCC* thickness map for an eye suffering from AMD (bottom row). Detected lesions are outlined in white.

3.3.2. Accuracy evaluation on retinas without topology-disrupting pathologies

Although the proposed method is designed for retinas with a topology-distributing pathology, it can also be applied to segment normal retinas. To test the method's performance on data without topology-distributing pathologies, we applied the proposed method to the data of healthy (20 peripapillary and 10 macular scans) and glaucoma affected eyes (10 peripapillary scans). Additionally, the Wilcoxon signed test with a Bonferroni correction was used to compare the accuracy of the proposed approach with the accuracy of the original method.

Table 3.3 provides detailed results on the accuracy of the proposed method and the original LCLS method on these data. Errors are expressed as MUE. The accuracy of the proposed approach, showed a MUE ranging from 2.3 to 9.5 μm, 2.9 to 8.4 μm and 2.8 to 8.5 μm for the healthy macular scans, healthy peripapillary scans and glaucoma peripapillary scans, respectively. On the other hand, the MUE of the original approach ranged from 2.7 to 5.9 μm, 2.7 to 7.1 μm and 3.1 to 8.8 μm for the healthy macular scans, healthy peripapillary scans and glaucoma peripapillary scans, respectively.

3.3.3. Segmentation of lesion on a retina affected by DME

To further illustrate the generalization of the proposed framework for joint segmentation of retinal layers and lesion, it was applied to a retinal scan of an eye affected by DME. To obtain the retinal cysts and layer segmentation, the framework described in section 3.2 was applied. The only two required changes were the introduction of two auxiliary interfaces for cysts segmentation within the *OPL* and two priors on their attenuation coefficients. Figure 3.8 shows examples of the obtained automatic segmentation of both retinal layers and cysts. Additionally, an en-face image of the auxiliary layer which contains the cyst segmentation is presented.

3.3.4. The Iowa Reference Algorithms

We segmented our dataset with the publicly available ”The Iowa Reference Algorithms” (Retinal Image Analysis Lab, Iowa Institute for Biomedical Imaging, Iowa City, IA) for retinal layer segmentation (version 3.6.0). The provided version segments eleven interfaces of which seven interfaces are considered within this paper: *vitreous - RNFL*, the *RNFL - GCL*, the *IPL - INL*, the *INL - OPL*, the *OPL - ONL*, the *IS ellipsoid* and *RPE* boundary. The software was applied to data from CSR and AMD patients and MSE and MUE were calculated. All details can be found in Appendix 3.A. In summary, the accuracy evaluation of The Iowa Reference Algorithms showed a MSE ranging from -15.3 μm to 40.2 μm and a MUE ranging from 11.6 μm to 55.9 μm for all data types. Overall, the software performed poorly when segmenting the CSR data and fails to segment some of the AMD scans. The large error terms for the CSR data seem to be due to the fact that software imposes rather strict priors on the overall shape of the macula. The fluid region largely corrupts the normal shape of retinal layers making the use of such prior knowledge difficult. In the AMD data, drusen do not affect the shape of the inner retinal layers

Table 3.3: Accuracy evaluation of the automatic layer segmentation in eyes without topology-disrupting pathology of the proposed and the original LCLS approach. Errors are expressed as MUE (μm).

	Proposed approach						*Original (LCLS) approach*		
	Healthy macula	p value*	Healthy peripapillary	p value*	Glaucoma peripapillary	p value*	Healthy macula	Healthy peripapillary	Glaucoma peripapillary
Vit.-RNFL	3.3	>0.05	2.9	0.02	4.7	>0.05	2.7	3.5	3.7
RNFL-GCL	4.5	>0.05	8.5	>0.05	8.8	>0.05	5.5	7.1	8.8
IPL-INL	9.5	0.03	7.1	>0.05	7.1	0.01	5.9	5.2	4.6
INL-OPL	6.7	>0.05	8.4	0.001	7.8	0.001	5.7	5.9	5.2
OPL-ONL	6.6	>0.05	4.9	>0.05	5.9	>0.05	5.6	4.7	4.2
IS ellip.	2.3	>0.05	3.1	0.001	2.8	>0.05	2.9	2.7	3.1
RPE bou.	3.8	>0.05	6.5	>0.05	5.5	>0.05	4.1	4.3	5.2

*Accuracy of the proposed approach compared to the accuracy of the original approach

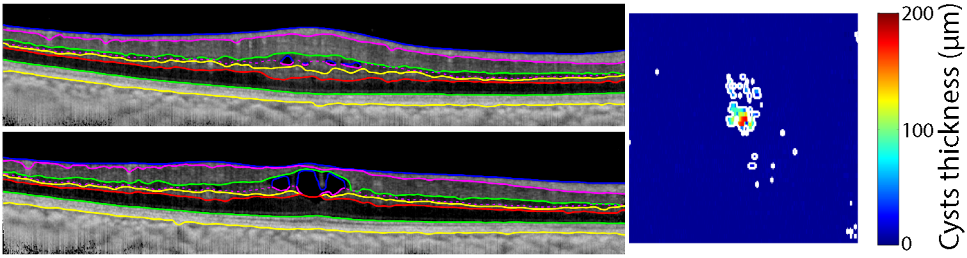

Figure 3.8: Examples of automatic layer and lesion segmentation on B-scans from a patient suffering from DME. A cysts thickness maps with the detected lesions outlined in white.

so extensively resulting in a considerably smaller error terms.

3.4. Discussion and conclusion

This paper presents a method to jointly segment retinal layers and lesions in eyes with topology-disrupting retinal diseases. The method utilizes the local attenuation coefficient differences between layers surrounding the interfaces and introduces auxiliary interfaces to segment lesions. Thus, the proposed method can handle local intensity variation and the presence or absence of pathological structures in the retina. The accuracy of both layer and lesion segmentation has been evaluated on eyes affected by CSR and AMD.

A good agreement between the segmentation performed manually by a medical doctor and results obtained from the automatic segmentation was found (the MUE for all interfaces in eyes affected by CSR and AMD varied between 3.9 and 11.9 µm (1 - 3.1 pixels)). Furthermore, lesion segmentation showed a Dice coefficient of 0.68 for drusen segmentation and 0.89 for fluid segmentation. Although the obtained values for drusen and fluid segmentation both indicate a good overlap between manual and automatic segmentation, results for fluid segmentation have a higher Dice coefficient. This result is expected as drusen and fluid pockets vary largely in size and spatial extent. If small errors occur in the segmentation of a fluid pocket, they hardly affect the Dice coefficient as a fluid pocket is usually very large. However, if small errors occur in the segmentation of an individual druse, whose volume can be very small, they will have a large impact on the Dice coefficient.

Additionally, layer segmentation was also evaluated on healthy (peripapillary and macular scans) and glaucoma affected eyes (peripapillary scans). The MUE for all interfaces ranged between 2.3 and 9.5 µm. The obtained results of layer segmentation on data without topology-disrupting pathology are similar to those obtained in our original approach [27]. This indicates that the proposed approach performs well on data without topology-disrupting pathologies. As such, the new method generalizes the previously presented method since it can handle both eyes with and without topology-disruptive pathologies.

In Figure 3.8, preliminary results of the segmentation of retinal layers and cysts in an eye affected by DME are shown. Although the segmentation was not evaluated, the preliminary results are encouraging. They show the flexibility of the proposed framework to be easily extended to another type of lesion.

Comparing our method with other retinal segmentation methods found in the literature is difficult. Every method was evaluated on different types of retinal images and using a different reference standard to report the accuracy. Therefore, we applied ”The Iowa Reference Algorithms”, publicly available software for retinal layer segmentation, to our dataset and evaluated its accuracy. The software performed poorly and even failed to segment some of the volumetric scans used within this paper. Our method achieve much better accuracy than the ”The Iowa Reference Algorithms”. Comparison with other segmentation methods is done only in a qualitative manner. In recent work, TPR of fluid lesions were reported ranging between 86 and 96% [7, 28, 30, 35, 36]. Furthermore, techniques for drusen segmentation reported an overlap ratio of 67% [11], an interclass correlation coefficient of 0.64 [12] and a MUE for the interfaces that surround the drusen ranging between 3 and 6 µm [7, 17]. The aforementioned approaches either focused on segmentation of a specific lesion or evaluated only the accuracy of lesion segmentation without evaluating the segmentation of retinal layers. Our method achieved similar results to those of the existing methods (TPR of 93% for fluid segmentation, Dice coefficient of 68% for drusen segmentation, MUE for the interfaces that surround the drusen ranging from 4.9 to 8.3 µm). However, our method also jointly segmented layers and lesion which is beneficial for clinical applications where one interprets the lesion within the context of retinal layers. In addition, several other approaches also segmented lesions and retinal layers and evaluated the accuracy of both [29, 31, 32]. These approaches reported an accuracy of layer segmentation, expressed as MUE, between 3 and 8 µm in exudative AMD patients [31], between 4 and 13 µm in serous pigment epithelium detachment patients [32] and between 3 and 8 µm in DME patients [29]. These results are comparable to our MUE (3.9 - 11.9 µm). However, these earlier reported approaches required training [29, 31] or were dependent on empirically determined thresholds [32], which is not required by the proposed framework.

In Figure 3.7, some of the possible applications of the developed method are presented. Using 3D segmentation of the retina, one can easily create and examine en face thickness maps of different layers in the retina or examine the presence, spatial distribution and extent of a lesion. Additionally, analysis of attenuation coefficient maps could be of interest. Our experiments showed that eyes affected by CSR show large variation in the estimated attenuation coefficient values. The variation could reflect a real change in optical properties of the layers in question or could be an artifact due to the assumptions of the model for transformation of the raw OCT data to attenuation coefficients. Further investigation of the cause of these variations is beyond the scope of this paper.

Overall, our method provides a flexible and accurate solution to jointly segment lesions and retinal layers. Similar performance of the proposed method was achieved on eyes with and without topology-disrupting pathologies. Thus, the approach show potential for clinical use as it is capable to handle both normal and topology-disrupting retinas. Future work could include a more extensive evaluation on eyes with lesions or extension to other retinal diseases.

3.A. Appendix

The segmentation results obtained with ”The Iowa Reference Algorithms” were compared with our manual annotations. The accuracy was determined by measuring the distance between manually and automatically segmented interfaces. For every interface, signed and unsigned distances were computed for every A-scan and then averaged. Table 3.4 provides detailed results on the accuracy of the of ”The Iowa Reference Algorithms” for seven interfaces. The software hardly provided any segmentation results for 2 out of 10 volume scans of AMD patients (B-scans used for accuracy evaluation in both volumes were marked as undefined and no segmentation results were given). Overall, 95 % of one volume and 85 % of the second volume was marked as undefined region. The rest of the AMD and CSR data did not have undefined regions and performed segmentation successfully. Finally, for comparison purposes, the results of our method on the same dataset are given in Table 3.1.

Table 3.4: Accuracy evaluation of ”The Iowa Reference Algorithms” in diseased eyes. Mean signed (MSE) and unsigned error (MUE) with corresponding standard deviations are reported. The error terms for AMD dataset were evaluated on 8 out of 10 volume scans.

	CSR		*AMD*	
	MSE (μm)	**MUE** (μm)	**MSE** (μm)	**MUE** (μm)
Vit.-RNFL	-2.7 ± 33.9	21.5 ± 26.6	-8.6 ± 24.0	14.0 ± 21.3
RNFL-GCL	14.5 ± 48.7	32.7 ± 38.8	-9.1 ± 24.9	16.3 ± 21.0
IPL-INL	28.5 ± 64.8	45.3 ± 54.4	-6.8 ± 20.1	13.7 ± 16.4
INL-OPL	39.1 ± 77.1	53.4 ± 67.8	-1.5 ± 19.3	11.6 ± 15.5
OPL-ONL	40.2 ± 79.7	55.9 ± 69.5	-6.0 ± 26.1	17.3 ± 20.4
IS ellip.	41.1 ± 74.4	53.7 ± 65.8	-0.5 ± 25.5	13.1 ± 22.0
RPE bou.	-15.3 ± 31.5	23.8 ± 25.6	-7.0 ± 32.2	19.4 ± 26.7

References

[1] D. Huang, E. A. Swanson, C. P. Lin, J. S. Schuman, W. G. Stinson, W. Chang, M. R. Hee, T. Flotte, K. Gregory, C. A. Puliafito, and et al., *Optical coherence tomography,* Science **254**, 1178 (1991).

[2] C. Bowd, R. N. Weinreb, J. M. Williams, and L. M. Zangwill, *The retinal nerve fiber layer thickness in ocular hypertensive, normal, and glaucomatous eyes with optical coherence tomography,* Archives of Ophthalmology **118**, 22 (2000).

[3] E. Yenice, A. Sengun, G. Soyugelen Demirok, and E. Turacli, *Ganglion cell complex thickness in nonexudative age-related macular degeneration,* Eye **29**, 1076 (2015).

[4] J. van der Schoot, K. A. Vermeer, J. F. de Boer, and H. G. Lemij, *The effect of glaucoma on the optical attenuation coefficient of the retinal nerve fiber layer in spectral domain optical coherence tomography images,* Investigative Ophthalmology and Visual Science **53**, 2424 (2012).

[5] C. Ahlers, W. Geitzenauer, G. Stock, I. Golbaz, U. Schmidt-Erfurth, and C. Prünte, *Alterations of intraretinal layers in acute central serous chorioretinopathy,* Acta Ophthalmologica **87**, 511 (2009).

[6] M. E. Pons, H. Ishikawa, R. Gurses-Ozden, J. M. Liebmann, H. Dou, and R. Ritch, *Assessment of retinal nerve fiber layer internal reflectivity in eyes with and without glaucoma using optical coherence tomography,* Archives of Ophthalmology **118**, 1044 (2000).

[7] S. J. Chiu, J. A. Izatt, R. V. O'Connell, K. P. Winter, C. A. Toth, and S. Farsiu, *Validated automatic segmentation of AMD pathology including drusen and geographic atrophy in SD-OCT images,* Investigative Ophthalmology and Visual Science **53**, 53 (2012).

[8] A. Lang, A. Carass, E. K. Swingle, O. Al-Louzi, P. Bhargava, S. Saidha, H. S. Ying, P. A. Calabresi, and J. L. Prince, *Automatic segmentation of microcystic macular edema in OCT,* Biomedical Optics Express **6**, 155 (2015).

[9] J. Y. Lee, S. J. Chiu, P. P. Srinivasan, J. A. Izatt, C. A. Toth, S. Farsiu, and G. J. Jaffe, *Fully automatic software for retinal thickness in eyes with diabetic macular edema from images acquired by cirrus and spectralis systems,* Investigative Ophthalmology and Visual Science **54**, 7595 (2013).

[10] S. Roychowdhury, D. D. Koozekanani, S. Radwan, and K. K. Parhi, *Automated localization of cysts in diabetic macular edema using optical coherence tomography images,* in *Engineering in Medicine and Biology Society (EMBC), 2013 35th Annual International Conference of the IEEE*, pp. 1426–1429.

[11] Q. Chen, T. Leng, L. Zheng, L. Kutzscher, J. Ma, L. de Sisternes, and D. L. Rubin, *Automated drusen segmentation and quantification in SD-OCT images,* Medical Image Analysis **17**, 1058 (2013).

[12] M. G. Nittala, H. Ruiz-Garcia, and S. R. Sadda, *Accuracy and reproducibility of automated drusen segmentation in eyes with non-neovascular age-related macular degeneration,* Investigative Ophthalmology and Visual Science **53**, 8319 (2012).

[13] B. J. Antony, M. D. Abramoff, M. M. Harper, W. Jeong, E. H. Sohn, Y. H. Kwon, R. Kardon, and M. K. Garvin, *A combined machine-learning and graph-based framework for the segmentation of retinal surfaces in SD-OCT volumes,* Biomedical Optics Express **4**, 2712 (2013).

[14] D. Cabrera DeBuc, G. M. Somfai, S. Ranganathan, E. Tatrai, M. Ferencz, and C. A. Puliafito, *Reliability and reproducibility of macular segmentation using a custom-built optical coherence tomography retinal image analysis software,* Journal of Biomedical Optics **14**, 064023 (2009).

[15] D. Cabrera Fernandez, H. M. Salinas, and C. A. Puliafito, *Automated detection of retinal layer structures on optical coherence tomography images,* Optics Express **13**, 10200 (2005).

[16] S. J. Chiu, X. T. Li, P. Nicholas, C. A. Toth, J. A. Izatt, and S. Farsiu, *Automatic segmentation of seven retinal layers in SD-OCT images congruent with expert manual segmentation,* Optics Express **18**, 19413 (2010).

[17] P. A. Dufour, L. Ceklic, H. Abdillahi, S. Schroder, S. De Dzanet, U. Wolf-Schnurrbusch, and J. Kowal, *Graph-based multi-surface segmentation of OCT data using trained hard and soft constraints,* Medical Imaging, IEEE Transactions on **32**, 531 (2013).

[18] H. Ishikawa, D. M. Stein, G. Wollstein, S. Beaton, J. G. Fujimoto, and J. S. Schuman, *Macular segmentation with optical coherence tomography,* Investigative Ophthalmology and Visual Science **46**, 2012 (2005).

[19] M. Mujat, R. C. Chan, B. Cense, B. Hyle Park, C. Joo, T. Akkin, T. C. Chen, and J. F. de Boer, *Retinal nerve fiber layer thickness map determined from optical coherence tomography images,* Optics Express **13**, 9480 (2005).

[20] A. Carass, A. Lang, M. Hauser, P. A. Calabresi, H. S. Ying, and J. L. Prince, *Multiple-object geometric deformable model for segmentation of macular OCT,* Biomedical Optics Express **5**, 1062 (2014).

[21] M. K. Garvin, M. D. Abramoff, R. Kardon, S. R. Russell, X. Wu, and M. Sonka, *Intraretinal layer segmentation of macular optical coherence tomography images using optimal 3D graph search,* IEEE Transactions on Medical Imaging **27**, 1495 (2008).

[22] R. Kafieh, H. Rabbani, M. D. Abramoff, and M. Sonka, *Intra-retinal layer segmentation of 3D optical coherence tomography using coarse grained diffusion map,* Medical Image Analysis **17**, 907 (2013).

[23] A. Lang, A. Carass, M. Hauser, E. S. Sotirchos, P. A. Calabresi, H. S. Ying, and J. L. Prince, *Retinal layer segmentation of macular OCT images using boundary classification,* Biomedical Optics Express **4**, 1133 (2013).

[24] M. A. Mayer, J. Hornegger, C. Y. Mardin, and R. P. Tornow, *Retinal nerve fiber layer segmentation on FD-OCT scans of normal subjects and glaucoma patients,* Biomedical Optics Express **1**, 1358 (2010).

[25] A. Mishra, A. Wong, K. Bizheva, and D. A. Clausi, *Intra-retinal layer segmentation in optical coherence tomography images,* Optics Express **17**, 23719 (2009).

[26] K. A. Vermeer, J. van der Schoot, H. G. Lemij, and J. F. de Boer, *Automated segmentation by pixel classification of retinal layers in ophthalmic OCT images,* Biomedical Optics Express **2**, 1743 (2011).

[27] J. Novosel, G. Thepass, H. G. Lemij, J. F. de Boer, K. A. Vermeer, and L. J. van Vliet, *Loosely coupled level sets for simultaneous 3D retinal layer segmentation in optical coherence tomography,* Medical Image Analysis **26**, 146 (2015).

[28] X. Chen, M. Niemeijer, L. Zhang, K. Lee, M. D. Abramoff, and M. Sonka, *3D segmentation of fluid-associated abnormalities in retinal OCT: Probability constrained graph-search graph-cut,* IEEE Transactions on Medical Imaging **31**, 1521 (2012).

[29] S. J. Chiu, M. J. Allingham, P. S. Mettu, S. W. Cousins, J. A. Izatt, and S. Farsiu, *Kernel regression based segmentation of optical coherence tomography images with diabetic macular edema,* Biomedical Optics Express **6**, 1172 (2015).

[30] X. Xiayu, L. Kyungmoo, Z. Li, M. Sonka, and M. D. Abramoff, *Stratified sampling voxel classification for segmentation of intraretinal and subretinal fluid in longitudinal clinical OCT data,* Medical Imaging, IEEE Transactions on **34**, 1616 (2015).

[31] G. Quellec, K. Lee, M. Dolejsi, M. K. Garvin, M. D. Abramoff, and M. Sonka, *Three-dimensional analysis of retinal layer texture: Identification of fluid-filled regions in SD-OCT of the macula,* IEEE Transactions on Medical Imaging **29**, 1321 (2010).

[32] F. Shi, X. Chen, H. Zhao, W. Zhu, D. Xiang, E. Gao, M. Sonka, and H. Chen, *Automated 3D retinal layer segmentation of macular optical coherence tomography images with serous pigment epithelial detachments,* Medical Imaging, IEEE Transactions on **34**, 441 (2015).

[33] S. Niu, Q. Chen, L. de Sisternes, D. L. Rubin, W. Zhang, and Q. Liu, *Automated retinal layers segmentation in SD-OCT images using dual-gradient and spatial correlation smoothness constraint,* Computers in Biology and Medicine **54**, 116 (2014).

[34] M. Pilch, K. Stieger, Y. Wenner, M. N. Preising, C. Friedburg, E. Meyer zu Bexten, and B. Lorenz, *Automated segmentation of pathological cavities in optical coherence tomography scanspathological cavities in OCT scans,* Investigative Ophthalmology and Visual Science **54**, 4385 (2013).

[35] H. Bogunovic, M. D. Abramoff, and M. Sonka, *Geodesic graph cut based retinal fluid segmentation in optical coherence tomography,* In: Chen X., Garvin M. K., Liu J., Trucco E., Xu Y., editors. Proceedings of the Ophthalmic Medical Image Analysis Second International Workshop (OMIA 2015) , 49 (2015).

[36] B. J. Antony, A. Lang, E. K. Swingle, O. Al-Louzi, A. Carass, S. Solomon, P. A. Calabresi, S. Saidha, and J. L. Prince, *Simultaneous segmentation of retinal surfaces and microcystic macular edema in SD-OCT volumes,* Proceedings of SPIE **9784**, 97841C (2016).

[37] I. Oguz, L. Zhang, M. D. Abramoff, and M. Sonka, *Optimal retinal cyst segmentation from OCT images,* Proceedings of SPIE **9784**, 97841E (2016).

[38] J. Novosel, Z. Wang, H. de Jong, K. A. Vermeer, and L. J. van Vliet, *Loosely coupled level sets for retinal layers and drusen segmentation in subjects with dry age-related macular degeneration,* Proceedings of SPIE **9784**, 97842P (2016).

[39] J. Novosel, Z. Wang, H. de Jong, M. van Velthoven, K. A. Vermeer, and L. J. van Vliet, *Locally-adaptive loosely-coupled level sets for retinal layer and fluid segmentation in subjects with central serous retinopathy,* Proceedings of ISBI, IEEE International Symposium on Biomedical Imaging , 702 (2016).

[40] K. A. Vermeer, J. Mo, J. J. A. Weda, H. G. Lemij, and J. F. de Boer, *Depth-resolved model-based reconstruction of attenuation coefficients in optical coherence tomography,* Biomedical Optics Express **5**, 322 (2014).

[41] V. Kajic, M. Esmaeelpour, B. Považay, D. Marshall, P. L. Rosin, and W. Drexler, *Automated choroidal segmentation of 1060 nm OCT in healthy and pathologic eyes using a statistical model,* Biomedical Optics Express **3**, 86 (2012).

[42] J. Rogala, B. Zangerl, N. Assaad, E. L. Fletcher, M. Kalloniatis, and L. Nivison-Smith, *In vivo quantification of retinal changes associated with drusen in age-related macular degeneration,* Investigative Ophthalmology and Visual Science **56**, 1689 (2015).

[43] Z. Yehoshua, G. Gregori, S. R. Sadda, F. M. Penha, R. Goldhardt, M. G. Nittala, R. K. Konduru, W. J. Feuer, P. Gupta, Y. Li, and P. J. Rosenfeld, *Comparison of drusen area detected by spectral domain optical coherence tomography and*

color fundus imaging, Investigative Ophthalmology and Visual Science **54**, 2429 (2013).

[44] NEI, *Age-related eye disease study–results,* (2015).

[45] E. W. Dijkstra, *A note on two problems in connexion with graphs,* Numerische Mathematik **1**, 269 (1959).

[46] R. Kafieh, H. Rabbani, F. Hajizadeh, M. D. Abramoff, and M. Sonka, *Thickness mapping of eleven retinal layers segmented using the diffusion maps method in normal eyes,* Journal of Ophthalmology **2015**, 14 (2015).

[47] P. P. Srinivasan, L. A. Kim, P. S. Mettu, S. W. Cousins, G. M. Comer, J. A. Izatt, and S. Farsiu, *Fully automated detection of diabetic macular edema and dry age-related macular degeneration from optical coherence tomography images,* Biomedical Optics Express **5**, 3568 (2014).

[48] P. Bakker, L. J. van Vliet, and P. W. Verbeek, *Edge preserving orientation adaptive filtering,* in *Computer Vision and Pattern Recognition, 1999. IEEE Computer Society Conference on.*, Vol. 1, p. 540.

[49] H. Knutsson, C.-F. Westin, and M. Andersson, *Representing local structure using tensors ii,* in *Image Analysis*, Lecture Notes in Computer Science, Vol. 6688, edited by A. Heyden and F. Kahl (Springer Berlin Heidelberg, 2011) Chap. 51, pp. 545–556.

[50] M. K. Garvin, M. D. Abramoff, X. Wu, S. R. Russell, T. L. Burns, and M. Sonka, *Automated 3D intraretinal layer segmentation of macular spectral-domain optical coherence tomography images,* IEEE Transactions on Medical Imaging **28**, 1436 (2009).

[51] M. D. Abramoff, M. K. Garvin, and M. Sonka, *Retinal imaging and image analysis,* IEEE Reviews in Biomedical Engineering **3**, 169 (2010).

4

Segmentation of locally varying numbers of outer retinal layers in OCT images

This chapter is based on the manuscript:

J. Novosel, S. Yzer, K. A. Vermeer and L. J. van Vliet, *Segmentation of locally varying numbers of outer retinal layers in OCT images*, IEEE Transactions on Medical Imaging, accepted (2017).

Abstract

Extraction of image-based biomarkers, such as the presence, visibility or thickness of a certain layer, from 3D optical coherence tomography data provides relevant clinical information. We present a method to simultaneously determine the number of visible layers in the outer retina and segment them. The method is based on a model selection approach with a special attention given to the balance between the quality of a fit and model complexity. This will ensure that a more complex model is selected only if this is sufficiently supported by the data. The performance of the method was evaluated on healthy and retinitis pigmentosa (RP) affected eyes. Additionally, the reproducibility of automatic method and manual annotations was evaluated on healthy eyes. A good agreement between the segmentation performed manually by a medical doctor and results obtained from the automatic segmentation was found. The mean-unsigned deviation for all outer retinal layers in healthy and RP affected eyes varied between 2.6 and 4.9 µm*. The reproducibility of the automatic method was similar to the reproducibility of the manual segmentation. Overall, the method provides a flexible and accurate solution for determining the visibility and location of outer retinal layers and could be used as an aid for the disease diagnosis and monitoring.*

4.1. Introduction

Optical coherence tomography (OCT) is a non-invasive, non-contact, optical imaging technique that can be used to acquire in-vivo images of retinal structures [1]. Due to its high axial resolution and sensitivity, different cell layers that compose the retina, can be visualized by differences in backscattering, as is shown in Figure 4.1a. Hence, the effect of retinal diseases on both the inner, anterior and the outer, posterior retinal layers can be investigated.

Retinitis pigmentosa (RP), age-related macular degeneration (AMD) and Stargardt disease (SD) are among those eye diseases that cause anatomical changes in the outer retinal layers. Retinal OCT images of RP subjects show that the *external limiting membrane* (*ELM*) and the *ellipsoid zone* (*EZ*) become dimmer or even completely disappear [2–4], whereas OCT scans of SD show that *ELM* and the *retinal pigment epithelium* (*RPE*) change in thickness [5, 6]. Therefore, presence, visibility and thickness of these outer retinal layers are potential biomarkers that can aid in the diagnosis and monitoring of retinal diseases. Manual annotations and extraction of these image-based biomarkers can be tedious, time consuming and subjective.

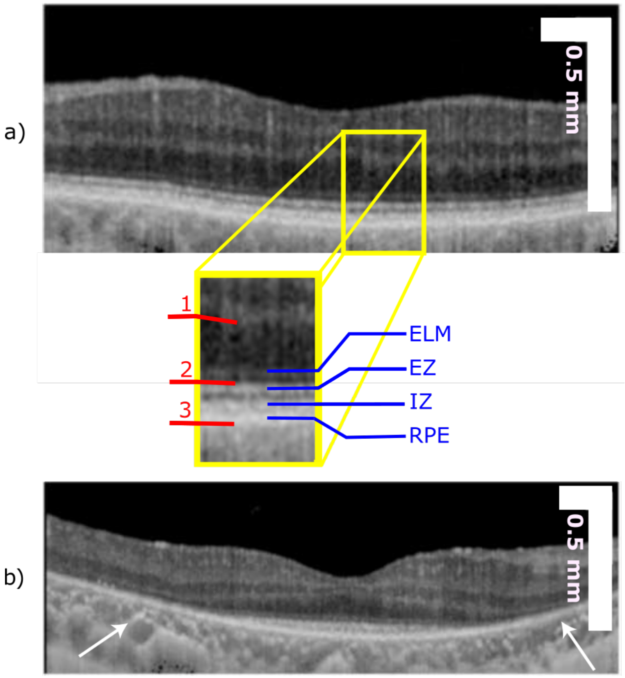

Figure 4.1: An OCT B-scan of a healthy (a) and RP (b) affected retina after conversion to attenuation coefficient (see section 4.3.1). The arrows point to areas where several outer retinal layers are no longer visible. Boundaries marked with red lines are obtained with our previously proposed method (see section 4.3.1) and are used to define the region of interest (the outer retina). The abbreviations of these interfaces are as follows: 1. *OPL - ONL* interface, 2. *anterior EZ boundary* and 3. *posterior RPE boundary*. The outer retinal layers and their abbreviations are indicated with blue lines.

To provide an objective assessment of the relevant retinal layers and thereby an objective quantification of the biomarkers, automatic segmentation methods are required.

Automatic segmentation of the layers in the outer retina can be challenging for the following two reasons. First, the layers are often indiscernible due to the limited resolution of the eye's optics and the OCT system [7]. Second, layers may deteriorate as a result of a disease [2, 6, 8]. Indeed, Lang et al. reported that segmentation of missing layers might be problematic [9]. Although many automatic algorithms for the segmentation of retinal layers have been developed [10–20], only three addressed the problem of vanishing layers [21–23]. First, Yang et al. [21] segmented the layers of the outer retina in a sequential manner by using a dual gradient and shortest path search in which some of the layers were allowed to overlap. However, in their approach the *ELM*, was not segmented, although it is of interest in both RP and SD. Second, Kafieh et al. [22] developed a cluster based approach to detect the "proper number of layers to be segmented" in retinas of healthy and glaucoma subjects. However, the approach considered only the visibility of the *ELM* and the *GCL - IPL* interface. Based on the detected visibility the data was placed into three groups with either 6, 7 or 12 interfaces between the retinal layers. The framework was tested only on healthy and glaucoma subjects, thus it remains unclear how it would perform on eyes where several retinal layers are missing. Finally, Srinivasan et al. [23] used a support vector machine prior to the actual segmentation ,to divide individual B-scans of mice retinas into two groups with either eight or ten layers present. However, the number of layers can change even within a single B-scan, as is shown in Figure 4.1b. Therefore, this method lacks flexibility since it relies on the strong and sometimes incorrect assumption that the same number of layers is present across the entire B-scan.

We present a method to simultaneously and locally determine the number of visible layers in the outer retina and segment them. The method operates on attenuation coefficient images, which represent an optical property of the tissue [24], and is based on a model selection approach. Standard model selection methods were applied in our previous work [25], in which no evaluation on the accuracy or reproducibility of the approach was performed. Here, we propose a modified measure of information complexity to account for parameter interdependencies and scaling. Within the model selection procedure specific attention is given to balance the quality of a fit with the model complexity. Each layer is modelled as a Gaussian function and several models of the outer retina, each with different number of layers, are considered. The different models are based on previously reported work on the visibility of layers and their deterioration [2, 4]. Finally, model parameters are estimated and the model that best supports the data is selected. The winning model provides not only the number of visible layers, but also their visibility, position and identification. Within this paper, the performance and reproducibility of the method is evaluated on healthy subjects, as well as its ability to segment eyes affected by RP. Results on the following layers will be presented: the *external limiting membrane* (*ELM*), the *ellipsoid zone* (*EZ*), the *integration zone* (*IZ*), and the *retinal pigment epithelium* (*RPE*) [26] (each layer is represented by the center line that passes through that layer as indicated in Figure 4.1).

The outline of this paper is as follows. Section 4.2 presents the methods for model selection and parameter estimation. Section 4.3 describes how the presented methods are applied to solve the outer retinal layer segmentation problem. In Section 4.4, the performance of the methods on healthy and RP affected retinas is evaluated as well as the reproducibility of both manual and automatic segmentation. Additionally, we show some examples of possible applications, such as the projection of the number of visible layers for every A-scan onto a 2D en face image. Finally, the presented methods and the results are discussed in Section 4.5.

4.2. Methods: Model selection and fitting

4.2.1. Model selection

Model selection is the task of choosing from a set of candidate models, the model that is best supported by the available data. Two properties are commonly used in model selection approaches: the goodness of a fit and the model complexity. The goodness of fit describes how well a model represents the set of observations, whereas complexity is a property of a model. Often, a more complex model has more parameters and will therefore result in a better goodness of a fit. However, the added complexity might not capture the signal, but merely describe noise. When this occurs, a more complex model over-fits the data. To reduce the possibility of over-fitting, information about the complexity of a model should be weighted against the goodness of a fit. Various criteria for model selection have been proposed. In these criteria, the goodness of fit is commonly represented by the likelihood associated with the maximum likelihood estimation (MLE) [27]. However, they differ in terms of how the model complexity is incorporated.

The likelihood ratio test (LRT) provides a widely used basis for model selection [28]. It is generally used to compare two nested models (i.e., one of the models is a special case of the other model). The performance of the two models is evaluated by looking at the ratio of their goodness of fit. The test expresses how much more likely it is that the data comes from the more complex model rather than the simpler one. As such, LRT does not incorporate any information about model complexity.

The Akaike information criterion (AIC) is another widely used criterion [29]. It balances the complexity and goodness of fit, where model complexity is represented by the number of model parameters. The expression for AIC is as follows:

$$\mathrm{AIC} = -2\ln(L) + 2p \tag{4.1}$$

where L is the likelihood and p the number of parameters associated with a certain model. AIC was shown to perform poorly if the sample size was small [30], hence a corrected Akaike information criterion was proposed as follows: $AIC_c = -2\ln(L) + (2pn)/(n - p - 1)$, where n is the sample size [30]. Several other variations of the Akaike criterion were proposed, such as Quasi-AIC (QAIC) and Takeuchi's Information Criterion (TIC). These criteria are beyond the scope of this paper and not as commonly used as AIC.

The Bayesian information criterion (BIC) appears to be similar to AIC [31]. They share the same likelihood term, but differ in the way they penalize a model based on the number of model parameters. The expression for BIC is as follows:

$$\mathrm{BIC} = -2\ln(L) + 2p\ln(n). \tag{4.2}$$

As can be seen from the equations, the difference between BIC and AIC is in the assignment of a weight for complexity with respect to the sample size. However, both criteria and their extensions represent complexity as the number of parameters and do not fully take into account information concerning parameter redundancy, accuracy and interdependence [32].

The information complexity criterion (ICOMP) is a model selection criterion that includes information about interdependencies of model parameters and their stability [32]. The model complexity is based on calculation of the degree of interdependence between the parameters through the inverse Fisher matrix. The inverse Fisher matrix provides a measure of accuracy of the parameter estimation over the entire parameter space and can be viewed as the curvature of the likelihood function. The diagonal elements of the matrix contain information about the variance of the estimated parameters, whereas the off-diagonal elements contain their covariances. By including information about the interdependence, ICOMP provides a more judicious penalty term than either AIC or BIC [32]. The expression for calculating the ICOMP value for a certain model is as follows:

$$\mathrm{ICOMP} = -2\ln(L) + 2C(\mathcal{F}^{-1}) \tag{4.3}$$

where $\mathcal{F}$ is the Fisher information matrix and C denotes the complexity measurement as:

$$C(\mathcal{F}^{-1}) = \frac{s}{2}\left(\log\left(\frac{\mathrm{tr}(\mathcal{F}^{-1})}{s}\right) - \frac{1}{2}\log|\mathcal{F}^{-1}|\right) \tag{4.4}$$

where s is the rank of $\mathcal{F}^{-1}$.

Although the parameter stability and orthogonality are taken into account by the ICOMP measure, the criterion is not scale-invariant. Furthermore, when performing model selection with ICOMP, it is recommended to specify the model such that each model parameter is not affected by changes in the remaining model parameters [32]. If a model is specified such that it does not satisfy this recommendation or if a parameter scaling could play an important role in ensuring parameter stability, one could use a modified correlation form of ICOMP:

$$\mathrm{ICOMP}_R = -2\ln(L) + 2C(\mathcal{F}_R^{-1}) \tag{4.5}$$

where the inverse Fisher matrix is replaced by its normalized version as follows:

$$\mathcal{F}_R^{-1} = \mathrm{diag}\left(\mathcal{F}^{-1}\right)^{-1/2}\mathcal{F}^{-1}\mathrm{diag}\left(\mathcal{F}^{-1}\right)^{-1/2} \tag{4.6}$$

where $\mathrm{diag}\left(\mathcal{F}^{-1}\right)$ is a diagonal matrix containing the diagonal elements of $\mathcal{F}^{-1}$ [32]. This normalized form of the ICOMP criterion is scale-invariant and less affected by improper model specification [32].

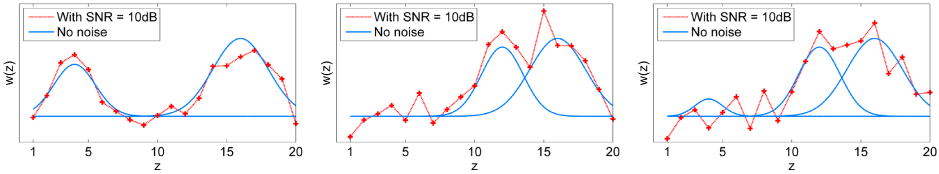

Figure 4.2: Illustration of simulated data for three examples used in section 4.2.3. The simulated Gaussians are shown in blue. The values used to generate these Gaussians were $\boldsymbol{\theta} = (3, 4, 1.5, 4.5, 16, 2)$, $\boldsymbol{\theta} = (4, 12, 1.5, 4.5, 16, 2)$, and $\boldsymbol{\theta} = (1, 4, 1, 4, 12, 1.5, 4.5, 16, 2)$ for the first, second and third example, respectively. Noise was added to these signals (shown in red) after which the model fitting and selection procedure was performed.

Finally, when performing model selection with each of the aforementioned criteria, the model that yields the smallest criterion value is selected as the model that is best supported by the data.

4.2.2. Model fitting and parameter estimation

Before the correct model can be selected, the potential models need to be fitted to the data to find the best model parameters according to the fitting procedure. The estimation of the model parameters was done by MLE.

Several assumptions were made in estimating the model parameters with MLE. First, a sequence of observations $(w_1, z_1), \dots (w_N, z_N)$ can be represented with a certain model $(M(\boldsymbol{\theta}, z))$ and additive measurement noise (ϵ) as $w = M(\boldsymbol{\theta}, z) + \epsilon$, where $\boldsymbol{\theta}$ are the model parameters. Second, the measurement noise is independent, identically distributed and can be approximated by a Gaussian distribution $\epsilon \sim \mathcal{N}(0, \sigma^2)$. Third, all observations are independent. Under these assumptions, the log likelihood to be maximized can be written as

$$\ln(\mathrm{L}) = -\sum_{j=1}^{N} \left(\frac{(w_j - M(\boldsymbol{\theta}, z_j))^2}{\sigma_M^2} \right) \tag{4.7}$$

The models used in our approach will be described in more detail in section 4.3.2 and the estimation of the measurement error (σ^2) in section 4.3.3.

4.2.3. Numerical examples for model selection

In this section, we give three numerical examples to demonstrate how various model selection criteria perform in identifying the true model under various conditions.

Several models which differed in the number of parameters were considered. The models were defined as follows:

$$M(\boldsymbol{\theta}, z) = \sum_{i=1}^{k} a_i \exp\left(-\frac{(z - l_i)^2}{2\sigma_i^2} \right) \tag{4.8}$$

Table 4.1: Percentage of selection of each model based on different model selection criteria for three different signal realizations. $M_1(\boldsymbol{\theta},z)$, $M_2(\boldsymbol{\theta},z)$ and $M_3(\boldsymbol{\theta},z)$ represent models composed of one, two and three Gaussians, respectively.

	$M_1(\boldsymbol{\theta},z)$	$M_2(\boldsymbol{\theta},z)$	$M_3(\boldsymbol{\theta},z)$
Example 1 - Two well-separated Gaussians			
AIC	0%	**98%**	2%
BIC	0%	**99%**	1%
ICOMP	0%	**97%**	3%
ICOMP$_R$	0%	**92%**	8%
Example 2 - Two overlapping Gaussians			
AIC	45%	**50%**	6%
BIC	**55%**	43%	2%
ICOMP	16%	**73%**	12%
ICOMP$_R$	12%	**72%**	16%
Example 3 - Three Gaussians			
AIC	33%	**37**%	30%
BIC	**51%**	33%	17%
ICOMP	15%	42%	**44%**
ICOMP$_R$	6%	30%	**64%**

where k indicates the number of the Gaussian functions, $\boldsymbol{\theta} = (\boldsymbol{\theta}_1, \ldots, \boldsymbol{\theta}_k)$ and $\boldsymbol{\theta}_i = (a_i, l_i, \sigma_i)$ with $i \in 1, \ldots, k$ in which a_i, l_i and σ_i are respectively the amplitude, position and width of the Gaussian with index i.

In the first two examples, data was generated from the true model which has two Gaussian functions and for two sets of model parameters. In the third example, data was generated from a true model which consists of three Gaussian functions. Examples of the simulated data are shown in Figure 4.2. To the simulated signal, Gaussian distributed random noise was added to result in a signal-to-noise (SNR) ratio of 10 dB.

In the first example, the simulated data had two Gaussian functions clearly separated from each other. In the second example, the two Gaussian functions partially overlapped. In the final example, the simulated data contained a Gaussian function with a small amplitude and two partially overlapping Gaussians. For each example, one thousand noisy realizations were generated for the same 20 z - coordinates. Three models were considered for the fitting procedure: $M_1(\boldsymbol{\theta},z)$ (composed of one Gaussian function), $M_2(\boldsymbol{\theta},z)$ (composed of two Gaussian functions) and $M_3(\boldsymbol{\theta},z)$ (composed of three Gaussian functions). Simulated data for all three examples was fitted to all three models. Afterwards, for each fit, the corresponding criteria values were calculated by using the expressions given in 4.2.1.

Table 4.1 shows the ability of the various model selection criteria to identify the true underlying model by stating how often each model was selected. In the first experiment, all model selection criteria perform equally well and were able to

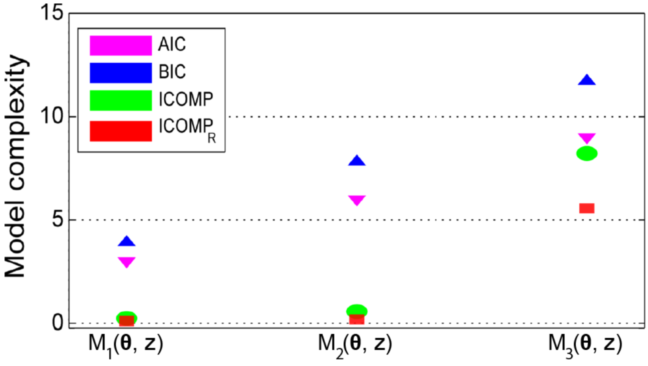

Figure 4.3: Values of complexity measurement for different criterion for one simulated dataset from the example with two overlapping Gaussians. $M_1(\boldsymbol{\theta}, z)$, $M_2(\boldsymbol{\theta}, z)$ and $M_3(\boldsymbol{\theta}, z)$ represent models composed of one, two and three Gaussians, respectively.

identify the true underlying model in over 92% of the cases. The results become more interesting in the second and third example where it becomes more difficult to distinguish the true model for all model selection criteria. However, ICOMP and ICOMP_R perform better than AIC or BIC. By modelling complexity in a more advanced way, in the second example, they are able to select the correct model in a larger number of cases (approximately 20% more). In the final and third example, the benefit of using ICOMP_R was illustrated, as it is able to recognize the correct model in 64% of the cases, whereas other criteria selected it in less than 50% of the cases.

Furthermore, in Figure 4.3 we show for one simulated dataset from the second example, how the calculated complexity varies between different model selection criteria. For AIC and BIC, as expected, we see a linear increase in complexity with the increase of the number of model parameter (the number of parameters is three, six and nine for $M_1(\boldsymbol{\theta}, z)$, $M_2(\boldsymbol{\theta}, z)$ and $M_3(\boldsymbol{\theta}_, z)$, respectively). For ICOMP and its normalized version, the complexity also increases with the number of parameters, however, no longer in a linear fashion. With ICOMP, the complexity value remains low for $M_1(\boldsymbol{\theta}, z)$ (the simplest model) and $M_2(\boldsymbol{\theta}, z)$ (the true model) and steeply increases for $M_3(\boldsymbol{\theta}_3, z)$, which would indeed lead to overfitting. ICOMP_R shows the same behaviour as ICOMP, however the complexity is smaller than for ICOMP.

As shown from our experiments, when Gaussian functions are clearly separated, all model selection criteria perform approximately equally well. However, when Gaussian functions are no longer clearly separable or when a Gaussian function with a small amplitude is present, as is often the case in the outer retina, both the ICOMP and ICOMP_R outperform AIC and BIC. Furthermore, ICOMP_R, as a results of its theoretical advantages (scale-invariance and less affected by improper model specification), performs better than ICOMP. Thus, in the following section, model selection was performed only with ICOMP_R.

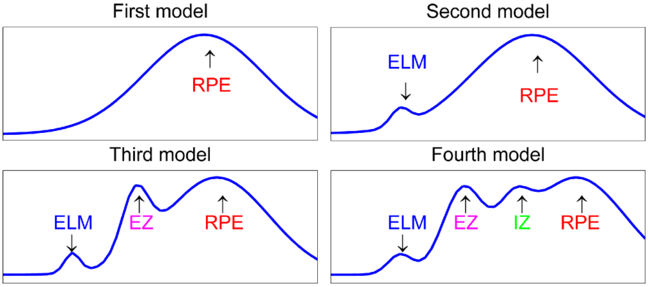

Figure 4.4: Graphical representation of the used models of the outer retina and corresponding layers in each model.

4.3. Outer retina layer segmentation

Several processing steps are performed to segment the layers in the outer retina: pre-processing, fitting the candidate models, model selection and layer identification. First, the pre-processing step detects the region of interest (the location of the outer retina). Second, the parameters of the various models for the outer retina are calculated for every A-scan by using MLE. Third, the model selection procedure based on ICOMP_R is applied to select the model best supported by the data. Fourth, the labels are assigned to the detected layers.

4.3.1. Pre-processing

The raw OCT data is converted to attenuation coefficients after which the loosely coupled level sets (LCLS) framework [15] is applied to the converted data to detect the location of the outer retina. Next, each B-scan is filtered with an 1D Gaussian filter [33] steered along the orientation obtained by a 2D structure tensor [34] with a gradient and tensor scale of $\sigma_g = 25$ µm and $\sigma_t = 120$ µm, respectively. The standard deviation of the Gaussian filter was equal to the spacing between subsequent B-scans. Afterwards, each B-scan was sub-sampled such that the obtained spacing along a B-scan matched the spacing between B-scans. Finally, the region of interest for the parameter estimation and model selection procedure was set to be between the *posterior RPE boundary* and the lower of the two following boundaries: the *OPL-ONL* interface or 40 µm above the *anterior EZ boundary*.

4.3.2. Representation of layers and models

In case of a thin reflecting layer (i.e., thin in comparison to the coherence length of the used light source), the response of the OCT system corresponds to a weighted and shifted version of the system's point spread function (PSF), which can be approximated by a Gaussian function. Since some of the outer retinal layers originate from structures thinner than the PSF of an OCT system [7], we modelled each of the layers in the outer retina as a Gaussian function. Furthermore, we considered several models of the outer retina, each with a different number of layers and composed of different tissues. These models are created by a superposition of shifted, scaled and compressed/stretched Gaussian functions and can be written, by redefining the models from section 4.2.3, as follows:

$$M(\boldsymbol{\theta}, z) = \sum_{i=1}^{k} a_i \exp\left(-\frac{(z - l_i)^2}{2\sigma_i^2}\right) + c \tag{4.9}$$

where c is the signal offset (noise floor) and a_i, l_i and σ_i are the model parameters corresponding to respectively the amplitude, location and standard deviation of the Gaussian function representing layer i. The variable k indicates the number of Gaussians in a certain model. In our framework, four models of the outer retina were considered, hence k varied from 1 to 4. The models were created such that they reflected previously published work on the visibility of the outer retinal layers [7] and their deterioration [3] and are illustrated in Figure 4.4. In the single layer model, the only visible layer corresponds to the *RPE*. In the dual layer model, the *ELM* becomes visible in addition to the *RPE*. The triple layer model contains the *ELM*, *EZ* and *RPE*. The quadruple layer model assumes that all layers in the outer retina are visible and adds the *IZ* to the set of visible layers. Finally, although a layer is defined as a Gaussian function, the final segmentation result is extracted as the location parameters of the selected model which result in a surfaces that passes through the corresponding outer retinal layer.

4.3.3. Model fitting and model selection

The model parameters for each model were estimated by maximizing the likelihood function of equation 4.7. The assumptions mentioned in the section 4.2.2, apply here as well and the same statistical model is used ($w = M(\boldsymbol{\theta}, z) + \epsilon; \epsilon \sim \mathcal{N}(0, \sigma^2)$) where the data points ($w(z)$) in equation 4.7 were natural logarithm values of the anisotropically filtered attenuation coefficients along an A-scan. The logarithmic transform of the data was taken because the noise appeared to be multiplicative (i.e. the noise increased with increasing attenuation coefficients). The measurement error (σ_M in equation 4.7) was estimated from the filtered and sub-sampled volumes of the retina which were first flattened based on the available segmentation of the *posterior RPE boundary* as obtained by the LCLS method. Then, corresponding A-scans from neighboring B-scans were subtracted from each other and the variance was calculated for every pair of A-scans. The average of the calculated variances was computed and its square root used as measurement error for the entire B-scan. Finally, the signal offset (c), which represents the background signal, in equation 4.9 was chosen to be fixed, as the parameter had the tendencies to be overestimated when fitted which lead to incorrect estimation of the Gaussian function that represents *ELM*. The value was set to the 5th percentile value present in an A-scan (within the region of interest).

To improve the robustness of the proposed approach, prior knowledge about the outer retinal layers was incorporated into the optimization procedure by constraining the possible values for the the model parameters (a_i, l_i, σ_i). The constraints were imposed to provide guidance to the fitting procedure, however they were still weak enough such that they do not interfere with the outcome of the fitting procedure in diseased eyes. The location of *ELM* was restricted to the area between the *OPL-ONL*

Table 4.2: Amplitude constraint for different layers (mm^{-1}).

	Minimal	Maximal
ELM	0.01	0.2
EZ	0.5	10
IZ	0.1	2
RPE	3	80

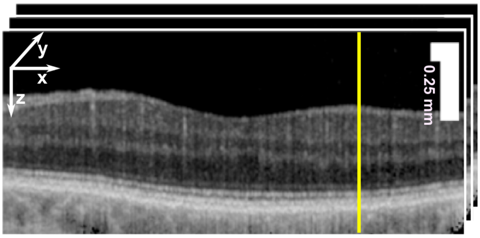

Figure 4.5: An few consecutive macular B-scans forming the retina. The yellow line indicates an A-scan. The used coordinate system is indicated with arrows in the top left corner.

interface and the *anterior EZ boundary* (as detected with the LCLS method) and the other layers had to be within the region bounded by the *anterior EZ boundary* and the *posterior RPE boundary* (also detected with the LCLS method). The standard deviation of the Gaussians, that represent the layers, was constrained to the range of 2-40 µm. An additional constraint was put on the amplitude of different layers, based on prior knowledge of the attenuation coefficients of the different layers as reported in Table 4.2. This constraint was determined experimentally by using data from healthy subjects (independent from those used for accuracy evaluation). Finally, the predefined order of the layers was enforced.

4.3.4. Post-processing specific for retinitis pigmentosa

To improve spatial consistency of the segmented layers, a post processing step specific for eyes affected by RP is proposed. For this, the number of visible layers for every A-scan is projected onto a 2D en face image on which further processing is performed. The en face image is decomposed into four binary images each showing area in which either one, two, three or four layers are visible. Each image is processed by two morphological filtering steps: a morphological opening (to remove possible noise present as small and isolated structures) followed by a dilation operation (to connect discontinuities in layers smaller than the structuring element and create a more continuous result), both using a disk-shaped filter with a radius of 60 µm). The radius was based on the clinical need (as determined by the scan protocol for RP patients), which indicates that information smaller that 120 µm are not relevant. The individual images are then summed together to create an updated en face image. Finally, segmentation of retinal layers is extracted as the position parameter (l) of the fitted Gaussian model with the number of layers that corresponds to the value obtained from the updated en face image.

4.3.5. Data

The OCT data for this study was obtained from the Rotterdam Eye Hospital (Rotterdam, the Netherlands) and contained 20 macular scans of healthy subjects and 10 macular scans of RP patients. All scans were acquired with a Spectralis OCT system (Heidelberg Engineering, Germany). The scan protocol for healthy eyes combined 143 B-scans composed of 384 A-scans of 496 pixels into one volume for 17 eyes. For three healthy subjects, the scan protocol combined 193 B-scans composed of 512 A-scans of 496 pixels into one volume. For RP affected eyes, the volume contained 37 B-scans composed of 512 A-scans of 496 pixels. The system employed an eye-tracker and was set to average 5/35 B-scans before moving to the next B-scan for scans of healthy/RP subjects. The field-of-view was $15°x15°$ and $20°x15°$ for 17 healthy and all diseased retinas, respectively. For three healthy retinas, the field of view was $20°x20°$. The scanned data was strongly anisotropic with a spacing of approximately 3.9x11.3x30 μm^3 for healthy eyes and 3.9x11.3x121 μm^3 for RP affected eyes in the z, x and y direction which correspond to the axial, the fast lateral and the slow lateral scanning axes, respectively. The used coordinate system is depicted in Figure 4.5.

4.4. Experiments and results

Two sets of experiments were done to evaluate the presented method. In the first experiment, the performance of the method was evaluated on healthy retinas, along with the reproducibility analysis. In the second experiment, the performance of the method on RP affected retinas was examined.

Each volumetric scan was converted to attenuation coefficients and one B-scan was randomly selected for manual annotations. Manual segmentation was performed by a medical doctor using ITK-SNAP (publicly available on `http://www.itksnap.org/`). The expert was asked to delineate all visible outer retinal layers. Although a single slice was extracted for annotation, the expert had access to the whole volume scan and could use it as an aid when determining the visibility of the layers and performing the annotations.

For every layer, both the accuracy of the layer's localization and the layer's visibility (detectability) was examined. The accuracy of how well the two segmentations agreed in determining the visibility was expressed in a measure of agreement (defined as the ratio of the true positives and true negatives over the number of A-scans). Furthermore, we present a measure of sensitivity (defined as the true positive rate), and negative predictive value. Additionally, the localization accuracy was determined by measuring differences between the results of our method and the manually segmented data. The mean-signed-deviation (MSD) and the mean-unsigned-deviation (MUD) were considered. The reproducibility of manual and automatic segmentation was also evaluated by the same error measures.

Finally, to eliminate a possible bias, in the localization accuracy, due to different criteria in automatic and manual segmentation (e.g. the automatic method might

Table 4.3: Agreement, sensitivity and negative predictive value of the automated method for determining the visibility of several layers for different model selection criteria on 20 healthy eyes.

	ELM	*EZ*	*IZ*	*RPE*
Agreement				
AIC	90%	96%	55%	99%
BIC	90%	95%	47%	99%
ICOMP	91%	97%	68%	99%
ICOMP_R	91%	97%	70%	99%
Sensitivity				
AIC	98%	96%	28%	100%
BIC	98%	95%	18%	100%
ICOMP	99%	97%	55%	100%
ICOMP_R	100%	97%	56%	100%
Negative predictive value				
AIC	72%	33%	39%	NaN%
BIC	63%	30%	38%	NaN%
ICOMP	56%	65%	48%	NaN%
ICOMP_R	74%	61%	48%	NaN%

have always segmented the peak of the Gaussian, whereas the manual annotator might have segmented one of the sides), the systematic error was estimated by using 5-fold cross-validation, after which the error was then subtracted from the automatic segmentation and MSD and MUD were recomputed. This systematic error represents a difference that may occur across all retinal images due to different criteria that a manual annotator and the automated method might have used to segment the interfaces.

4.4.1. Performance and reproducibility anaylsis on healthy retinas

The first evaluation of the presented segmentation method was done on macular scans of healthy subjects. The scans of 20 subjects (one eye per subject) were used to estimate the performance of the method. For 10 out of those 20 subjects, the reproducibility of both the manual and automatic segmentation was obtained by measuring the difference between the segmentation results of two successive volume scans. Before the second scan was made, the subject was asked to stand up, after which the OCT system was again aligned with the subject's head and eyes. Afterwards, the two scans were registered to each other by internal processing of the OCT system.

Table 4.3 provides information about the agreement, negative predictive value and sensitivity of the automatic segmentation in 20 healthy subjects for all model selection criteria. As seen from the Table, all model selection criteria perform similarly for *ELM*, *EZ* and *RPE*. Larger difference can be seen for *IZ*, in which AIC and

Table 4.4: Performance analysis of the automatic segmentation with MSD and MUD before (within parentheses) and after bias correction on healthy subjects. Reproducibility analysis of the automatic method and manual segmentation.

	Performance					Reproducibility									
						Automatic					Manual				
	MSD (µm)	**MUD** (µm)	**%** AG*	**%** SEN*	**%** NPV*	**MSD** (µm)	**MUD** (µm)	**%** AG*	**%** SEN*	**%** NPV*	**MSD** (µm)	**MUD** (µm)	**%** AG*	**%** SEN*	**%** NPV*
ELM	0.1 (5.2)	3.1 (5.3)	91	100	74	0.1	2.5	99	100	NaN	0.6	2.7	86	92	60
EZ	-0.1 (5.0)	2.8 (5.0)	97	97	61	0.4	1.7	97	98	NaN	0.1	3.7	99	100	79
IZ	-0.1 (3.1)	2.6 (3.3)	70	56	48	0.3	2.2	76	63	50	-0.8	3.1	78	77	70
RPE	-0.1 (0.1)	3.3 (3.5)	99	100	NaN	-1.5	2.3	100	100	NaN	0.6	3.6	99	100	78

*Agreement (AG), sensitivity (SEN) and negative predictive value (NPV) over which the two segmentations agreed in determining the visibility

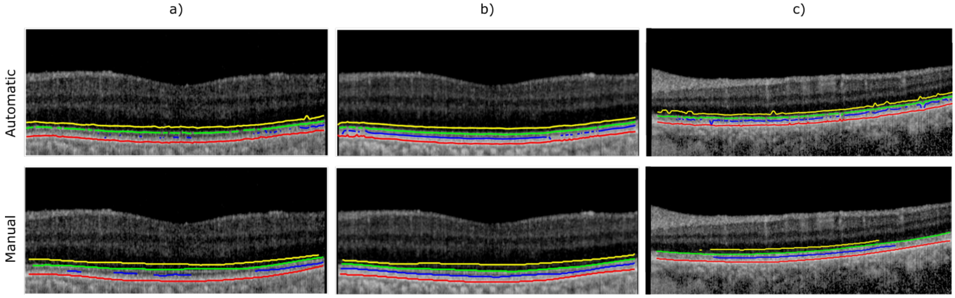

Figure 4.6: Automatic and manual segmentation results on B-scans from healthy subjects. Examples shown in a) and b) are from two successive scans of a single subject and illustrate the limited reproducibility of *IZ*. Example in c) shows disagreement in visibility of parts of *ELM* and *IZ* as determined by automatic and manual segmentation.

BIC perform worse that ICOMP and ICOMP_R. This confirms findings from section 4.2.3. Further, although with only slight difference, ICOMP_R performs better that ICOMP, thus all further evaluation will be based on ICOMP_R selection criteria.

Table 4.4 provides detailed results on the performance (including results before and after bias correction) and reproducibility of the automatic method. An error of 3.9 µm corresponded to one pixel along the recorded A-scans. The localization accuracy evaluation, after bias correction, showed a MSD ranging from -0.1 µm to 0.1 µm and a MUD ranging from 2.6 µm to 3.3 µm. The reproducibility of the automatic method had a MSD between -1.5 µm and 0.1 µm, and a MUD ranging from 1.7 µm to 2.5 µm, whereas, the reproducibility of the manual annotations resulted in a MSD between -0.8 µm and 0.6 µm and a MUD ranging from 2.7 µm to 3.6 µm.

The agreement and negative predictive value, between manual and automatic segmentation in healthy subjects varied strongly for the different layers, whereas the sensitivity analysis of the accuracy remains high. The reproducibility analysis, shows the lowest agreement and sensitivity for the *IZ* for both manual and automatic segmentation. For the *ELM*, the reproducibility of the agreement and sensibility for the manual annotations were 86% and 92%, respectively. For the automatic method these values were 99% and 100%. The negative predictive value of automatic reproducibility was undefined (reported as NaN) for all layers except *IZ*, whereas the negative predictive value of manual reproducibility varied. Undefined values are due to not having any true negatives (i.e. given the used models (described in section 4.3.2), the automatic method will always have at least one layer identified and segmented).

Figure 4.6 shows examples of the manual annotation and the segmentation results obtained with the presented method on several B-scans from different subjects. The first two examples are B-scans used for reproducibility analysis, which illustrate how the visibility of the *IZ* varies between two successive scans. In the third example, a disagreement in the visibility of parts of the *ELM* and *IZ* as annotated by manual and automatic segmentation is shown.

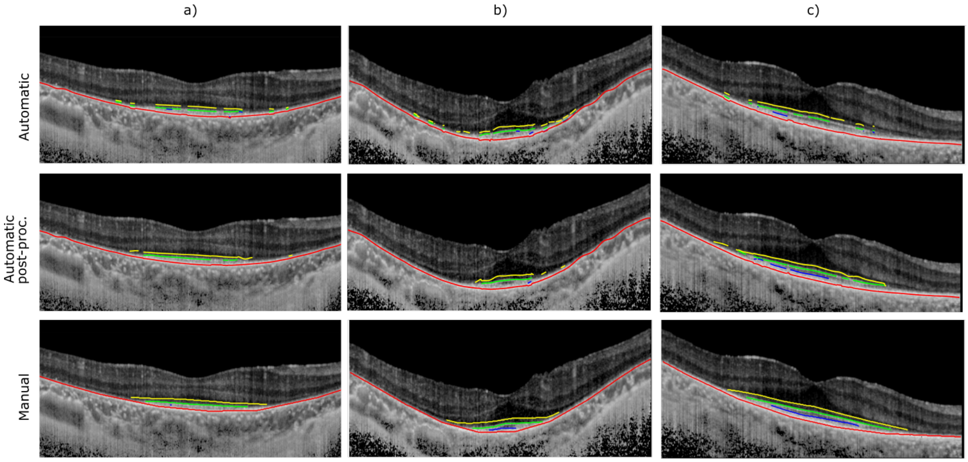

Figure 4.7: Automatic (before and after post-processing) and manual segmentation results on several B-scans from different eyes affected by RP.

Using the segmentation results obtained with the developed method one can create en face images with the number of visible layers in the retina for a concise examination. Examples of such 2D en face images for healthy eyes are shown in Figure 4.8. In these images, the number of retinal layer varied between 3 and 4, as was expected when examining a healthy retina.

4.4.2. Performance analysis on retinitis pigmentosa affected eyes

The second set of experiments was performed to assess the performance of the method on ten eyes (one eye per subject) affected by RP. For these eyes, the systematic error was estimated from all healthy subjects (from section 4.4.1). Table 4.5 provides detailed results on the agreement, negative predictive value and sensitivity before and after post-processing (as described in section 4.3.4) and on the errors of the automatic method before and after bias correction. The MSD before post-processing (and after bias correction) was ranging from -2.9 µm to 1.2 µm and the MUD was ranging from 3.4 µm to 4.9 µm, whereas after post-processing (and after bias correction) the MSD varied between -2.3 µm to 3.3 µm and the MUD ranged from 3.5 µm to 5.9 µm. The agreement in visibility of layers between two segmentation, before post-processing was 81%, 86%, 94% and 100% for *ELM*, *EZ*, *IZ* and *RPE*, respectively. The agreement after post-processing was higher (87%, 94%, 97% and 100% for *ELM*, *EZ*, *IZ* and *RPE*, respectively). The sensitivity and negative predictive value also increased after post-processing step. Figure 4.7 shows examples of the manual annotation and the automatic segmentation results before and after post-processing on B-scans of eyes affected by RP.

Again, with the obtained results, en face images with the number of visible layers can be created. Examples of such 2D en face image with the number of visible layers for RP affected eyes are shown in Figure 4.8. As can be seen from the

Table 4.5: Performance analysis of the automatic segmentation on retinitis pigmentosa affected eyes before and after post-processing (MSD and MUD are reported before (within parentheses) and after bias correction).

	Before post-processing					After post-processing				
	MSD (µm)	**MUD** (µm)	**%** AG*	**%** SEN*	**%** NPV*	**MSD** (µm)	**MUD** (µm)	**%** AG*	**%** SEN*	**%** NPV*
ELM	-0.8 (5.0)	4.0 (6.1)	81	71	79	0.1 (5.2)	3.5 (6.2)	87	84	84
EZ	-2.9 (0.9)	3.4 (3.4)	86	70	88	-2.3 (2.8)	3.2 (3.7)	94	82	94
IZ	-1.9 (0.9)	3.4 (3.1)	94	78	96	-2.0 (0.2)	2.5 (1.8)	97	82	98
RPE	1.2 (4.9)	4.9 (6.7)	100	100	NaN	3.3 (5.0)	5.9 (6.5)	100	100	NaN

*Agreement (AG), sensitivity (SEN) and negative predictive value (NPV) over which the two segmentations agreed in determining the visibility images, large parts of the retina have only one layer visible. These areas correspond to a diseased part of the retina and are in agreement with pathological changes (the peripheral rod cells are affected first) in patients suffering from RP.

4.5. Discussion and conclusion

This paper presents a method to simultaneously determine the number of visible layers in the outer retina and segment them. The method is based on a model selection approach with special attention given to balance the quality of a fit with model complexity. As such, the model selection procedure ensures that a more complex model is selected only if sufficiently supported by the data. The approach is able to cope with layers that may or may not be present within an image and provides not only the number of visible layers, but also their position and identification.

The performance of the method was evaluated on healthy and RP affected eyes. A good agreement between the manually obtained segmentation and the results obtained from the automatic segmentation was found. The MUD, after bias correction, for all layers in healthy and RP affected eyes varied between 2.6 and 5.9 μm or 0.7 - 1.5 pixels.

Reproducibility measures of the manual and automatic method are similar for all layers except for *ELM*, where the agreement in visibility and sensitivity of automatic method were better than that of manual annotations. In cases where *ELM* was poorly visible, manual annotations were not consistent, although it is highly unlikely that *ELM* would not be present in a healthy retina. This reduced agreement in visibility is also reflected in the agreement analysis of healthy subjects where these inconsistent manual annotations are compared against automatic result. Furthermore, reproducibility analysis of both manual and automatic segmentation indicates that *IZ* varied the most in its visibility. This is consistent with the known variability in visibility even in healthy retinas [7].

The localization accuracy evaluation in eyes affected by RP shows similar errors before and after post-processing, however after post-processing the agreement, sensitivity and negative predictive value increased. The agreement, after post-processing, is slightly higher for *IZ*, when compared to the corresponding agreement of healthy eyes. The reason for the higher agreement for *IZ* is due to the fact that this layer is hardly visible in the data used for the evaluation (all scans in which *IZ* was visible are given in Figure 4.7). Despite being hardly visible in RP data, the segmentation of *IZ* shows relatively high sensitivity and negative predictive value, indicating good segmentation results.

A relatively simple post-processing step largely improved the spatial consistency of the automatic method. The post-processing was made to be disease specific and could easily be modified. The amount of consistency was based on the need for local analysis (size of the structures for morphological operations was based on the the clinical need - the used scanning protocol for RP indicates that information smaller than 120 μm is not relevant). The paper provides a general tool for the segmentation of the outer retinal layers, whereas post-processing permits including disease-specific prior information, thereby adapting to a specific task (e.g. in some eye diseases large areas are expected to be affected whereas in other diseases,

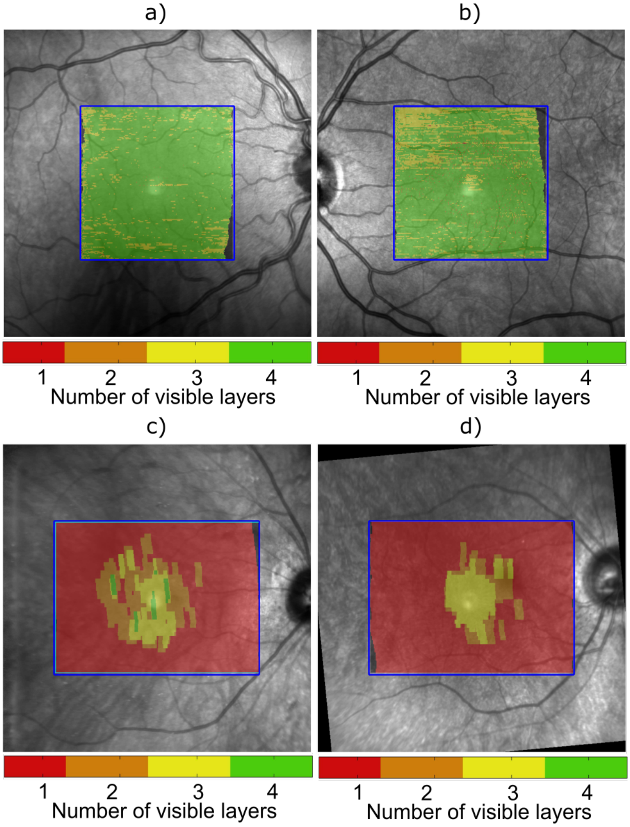

Figure 4.8: A scanning laser ophthalmoscopy (SLO) images of the retina (a blue square indicating the scan area) overlaid with an en face images with the number of visible layers in healthy eyes (a) and (b) and retinitis pigmentosa (results after post-processing) affected eyes (c) and (d).

small local changes could occur).

Our approach is among the first approaches to locally estimate the number of outer retinal layers and segment up to four of these layers. A few other segmentation approaches have been proposed to solve the problem of varying numbers of the retinal layers. Yang et al. [21] segmented outer retinal layers in RP subjects, without considering *ELM*, and reported errors ranging between 3 and 5 µm. Kafieh et al. [22] developed a cluster based approach in which, among outer retinal layers, only the visibility of *ELM* was considered. The approach was evaluated on healthy and glaucoma subjects and the reported performance, expressed as MUD, of the outer retinal layers segmentation was 4 - 7 µm. Finally, Srinivasan et al. [23] segmented the retinal layers in mouse retina. The reported MUD varied between 2 and 4 µm. However, the approach lacks in flexibility as it assumes the same number of layers across an entire B-scan. The results reported in these three approaches are in line with ours, although our approach provides a more generic solution to the outer retinal layer segmentation problem.

In Figure 4.8, an example of the possible application of the developed method is presented. One can project the number of visible layers onto a 2D image, which allows quick examination and identification of the possible pathologies. Furthermore, in case of a follow-up, one can investigate the extent of the present pathology between two visits and quickly assess disease progression or treatment efficacy.

The developed framework was applied to healthy and RP affected retinas, but could easily be extended to other retinal diseases that affect the visibility or presence of layers in the outer retina. For this, the models of the outer retina should be created such that they reflect prior knowledge about the deterioration of the retinal layers. Furthermore, the approach allows simple and intuitive modification of prior knowledge through constraints imposed during the fitting procedure. However, one should be reluctant to impose hard constraints as they may cause anomalies to be missed.

Overall, our method provides a flexible and accurate solution to the outer retinal layer segmentation problem. The approach determines the visibility of the outer retinal layers in OCT images and as such could provide valuable insights into disease progression patterns. Furthermore, it could be used as a tool for disease diagnosis and monitoring, as well as assessing and comparing the efficiency of both existing and possible new treatments.

References

[1] D. Huang, E. A. Swanson, C. P. Lin, J. S. Schuman, W. G. Stinson, W. Chang, M. R. Hee, T. Flotte, K. Gregory, C. A. Puliafito, and et al., *Optical coherence tomography,* Science **254**, 1178 (1991).

[2] A. Hagiwara, Y. Mitamura, K. Kumagai, T. Baba, and S. Yamamoto, *Photoreceptor impairment on optical coherence tomographic images in patients with retinitis pigmentosa,* British Journal of Ophthalmology **97**, 237 (2013).

[3] S. Aizawa, Y. Mitamura, A. Hagiwara, T. Sugawara, and S. Yamamoto, *Changes of fundus autofluorescence, photoreceptor inner and outer segment junction line, and visual function in patients with retinitis pigmentosa,* Clinical and Experimental Ophthalmology **38**, 597 (2010).

[4] D. C. Hood, M. A. Lazow, K. G. Locke, V. C. Greenstein, and D. G. Birch, *The transition zone between healthy and diseased retina in patients with retinitis pigmentosa,* Investigative Ophthalmology and Visual Science **52**, 101 (2011).

[5] W. Lee, K. Nõupuu, M. Oll, T. Duncker, T. Burke, J. Zernant, S. Bearelly, S. H. Tsang, J. R. Sparrow, and R. Allikmets, *The external limiting membrane in early-onset stargardt disease,* Investigative Ophthalmology and Visual Science **55**, 6139 (2014).

[6] T. R. Burke, D. W. Rhee, R. T. Smith, S. H. Tsang, R. Allikmets, S. Chang, M. A. Lazow, D. C. Hood, and V. C. Greenstein, *Quantification of peripapillary sparing and macular involvement in stargardt disease (STGD1),* Investigative Ophthalmology and Visual Science **52**, 8006 (2011).

[7] R. F. Spaide and C. A. Curcio, *Anatomical correlates to the bands seen in the outer retina by optical coherence tomography: Literature review and model,* Retina **31**, 1609 (2011).

[8] E. Ergun, B. Hermann, M. Wirtitsch, A. Unterhuber, T. H. Ko, H. Sattmann, C. Scholda, J. G. Fujimoto, M. Stur, and W. Drexler, *Assessment of central visual function in stargardt's disease/fundus flavimaculatus with ultrahigh-resolution optical coherence tomography,* Investigative Ophthalmology and Visual Science **46**, 310 (2005).

[9] A. Lang, A. Carass, M. Hauser, E. S. Sotirchos, P. A. Calabresi, H. S. Ying, and J. L. Prince, *Retinal layer segmentation of macular OCT images using boundary classification,* Biomedical Optics Express **4**, 1133 (2013).

[10] R. Kafieh, H. Rabbani, and S. Kermani, *A review of algorithms for segmentation of optical coherence tomography from retina,* Journal of Medical Signals and Sensors **3**, 45 (2013).

[11] D. C. DeBuc, *A review of algorithms for segmentation of retinal image data using optical coherence tomography,* in *Image Segmentation*, Vol. 6688, edited by P.-G. Ho (InTech, 2011) Chap. 2, pp. 14–54.

[12] K. A. Vermeer, J. van der Schoot, H. G. Lemij, and J. F. de Boer, *Automated segmentation by pixel classification of retinal layers in ophthalmic OCT images,* Biomedical Optics Express **2**, 1743 (2011).

[13] M. Mujat, R. C. Chan, B. Cense, B. Hyle Park, C. Joo, T. Akkin, T. C. Chen, and J. F. de Boer, *Retinal nerve fiber layer thickness map determined from optical coherence tomography images,* Optics Express **13**, 9480 (2005).

[14] M. A. Mayer, J. Hornegger, C. Y. Mardin, and R. P. Tornow, *Retinal nerve fiber layer segmentation on FD-OCT scans of normal subjects and glaucoma patients,* Biomedical Optics Express **1**, 1358 (2010).

[15] J. Novosel, G. Thepass, H. G. Lemij, J. F. de Boer, K. A. Vermeer, and L. J. van Vliet, *Loosely coupled level sets for simultaneous 3D retinal layer segmentation in optical coherence tomography,* Medical Image Analysis **26**, 146.

[16] H. Ishikawa, D. M. Stein, G. Wollstein, S. Beaton, J. G. Fujimoto, and J. S. Schuman, *Macular segmentation with optical coherence tomography,* Investigative Ophthalmology and Visual Science **46**, 2012 (2005).

[17] P. A. Dufour, L. Ceklic, H. Abdillahi, S. Schroder, S. De Dzanet, U. Wolf-Schnurrbusch, and J. Kowal, *Graph-based multi-surface segmentation of OCT data using trained hard and soft constraints,* Medical Imaging, IEEE Transactions on **32**, 531 (2013).

[18] A. Carass, A. Lang, M. Hauser, P. A. Calabresi, H. S. Ying, and J. L. Prince, *Multiple-object geometric deformable model for segmentation of macular OCT,* Biomedical Optics Express **5**, 1062 (2014).

[19] S. J. Chiu, X. T. Li, P. Nicholas, C. A. Toth, J. A. Izatt, and S. Farsiu, *Automatic segmentation of seven retinal layers in SD-OCT images congruent with expert manual segmentation,* Optics Express **18**, 19413 (2010).

[20] M. Garvin, M. Abramoff, R. Kardon, S. Russell, X. Wu, and M. Sonka, *Intraretinal layer segmentation of macular optical coherence tomography images using optimal 3D graph search,* Medical Imaging, IEEE Transactions on **27**, 1495 (2008).

[21] Q. Yang, C. A. Reisman, K. Chan, R. Ramachandran, A. Raza, and D. C. Hood, *Automated segmentation of outer retinal layers in macular OCT images of patients with retinitis pigmentosa,* Biomedical Optics Express **2**, 2493 (2011).

[22] R. Kafieh, H. Rabbani, M. D. Abramoff, and M. Sonka, *Intra-retinal layer segmentation of 3D optical coherence tomography using coarse grained diffusion map,* Medical Image Analysis **17** (2013).

[23] P. P. Srinivasan, S. J. Heflin, J. A. Izatt, V. Y. Arshavsky, and S. Farsiu, *Automatic segmentation of up to ten layer boundaries in SD-OCT images of the mouse retina with and without missing layers due to pathology,* Biomedical Optics Express **5**, 348 (2014).

[24] K. A. Vermeer, J. Mo, J. J. A. Weda, H. G. Lemij, and J. F. de Boer, *Depth-resolved model-based reconstruction of attenuation coefficients in optical coherence tomography,* Biomedical Optics Express **5**, 322 (2014).

[25] J. Novosel, K. Vermeer, L. Pierrache, C. Klaver, L. van den Born, and L. van Vliet, *Method for segmentation of the layers in the outer retina,* in *Engineering in Medicine and Biology Society (EMBC), 2015 37th Annual International Conference of the IEEE* (2015) pp. 5646–5649.

[26] G. Staurenghi, S. Sadda, U. Chakravarthy, and R. F. Spaide, *Proposed lexicon for anatomic landmarks in normal posterior segment spectral-domain optical coherence tomography,* Ophthalmology **121**, 1572.

[27] R. A. Fisher, *On the mathematical foundations of theoretical statistics,* Philosophical Transactions of the Royal Society of London A: Mathematical, Physical and Engineering Sciences **222**, 309 (1922).

[28] J. Neyman and E. S. Pearson, *On the problem of the most efficient tests of statistical hypotheses,* Philosophical Transactions of the Royal Society of London. Series A, Containing Papers of a Mathematical or Physical Character **231**, 289 (1933).

[29] H. Akaike, *A new look at the statistical model identification,* Automatic Control, IEEE Transactions on **19**, 716 (1974).

[30] C. M. Hurvich and T. Chih-Ling, *Regression and time series model selection in small samples,* Biometrika **76**, 297 (1989).

[31] G. Schwarz, *Estimating the dimension of a model,* The Annals of Statistics **6**, 461 (1978).

[32] H. Bozdogan, *Akaike's information criterion and recent developments in information complexity,* Journal of Mathematical Psychology **44**, 62 (2000).

[33] P. Bakker, L. J. van Vliet, and P. W. Verbeek, *Edge preserving orientation adaptive filtering,* in *Computer Vision and Pattern Recognition, 1999. IEEE Computer Society Conference on.*, Vol. 1, pp. 1–540 Vol. 1.

[34] H. Knutsson, C. F. Westin, and M. Andersson, *Representing local structure using tensors ii,* in *Image Analysis*, Lecture Notes in Computer Science, Vol. 6688, edited by A. Heyden and F. Kahl (Springer Berlin Heidelberg, 2011) Chap. 51, pp. 545–556.

5

Correlation of local glaucomatous damage in *RNFL* attenuation coefficient and thickness maps with visual field defects

Manuscript in preparation

Abstract

For glaucoma management, establishing a reliable correlation between information about structural (as assessed by means of optical coherence tomography (OCT)) and functional damage (as assessed by means of visual field (VF)) in the retina is of critical importance. Currently, VFs suffer from high variability, whereas structural examination is limited to the thickness properties of retinal nerve fiber layer (RNFL) in a narrow band. We propose to exploit the RNFL thickness over the whole OCT volume scans, as well as other optical properties of RNFL, such as attenuation coefficient (AC) to assess the relationship between structural and functional damage of the retina in glaucoma patients. We visually determined and scored correlations between local glaucomatous damage in both AC RNFL and RNFL thickness maps with areas of decreased retinal sensitivity in the corresponding VF. The agreement between the defects in the VF and the corresponding defect in the OCT derived maps was determined by a score on a scale of 1 (good correlation) to 4 (poor correlation). In total, 178 eyes of glaucoma patients were included and 374 individual correlations were scored. The percentage of correlation scores 1, 2 and 3 were somewhat higher for RNFL thickness compared to RNFL AC, with differences of 2.1%, 1.6% and 0.5%, respectively. The percentage of RNFL thickness with score 4 was 1.1% lower than for RNFL AC. In 66% of the scores, there was an optimal agreement between the correlation scores. However, in 34% of the correlations, the AC and thickness scores disagreed. In the disagreement cases, the superior performance of the RNFL thickness – VF correlation compared to the RNFL AC – VF correlation was again confirmed, however in almost half of the disagreement cases (43%) the RNFL AC – VF maps performed better. A general conclusion is that, within the used dataset, AC were not as effective in detecting glaucomatous damage as the thickness. The RNFL thickness outperformed RNFL AC. However, our results indicate that RNFL AC seem to hold additional information that may be used to improve the structure-function correlations in glaucoma.

5.1. Introduction

Today, 285 million people worldwide are either blind or have poor visual function which significantly deteriorates their quality of life [1]. A large percentage of existing visual impairments is caused by various eye diseases that can be prevented or slowed down by using existing technologies and applying current clinical practices for monitoring and treatment. Glaucoma is among the main causes of avoidable visual impairment [2] and the number of people with glaucoma is expected to increase to 76.0 million in 2020 and 111.8 million in 2040 [3]. The disease causes deterioration of the ganglion cells axons that form the optic nerve, which results in defects within the visual field. If left untreated, the disease can even lead to blindness [4].

Currently, the diagnosis and progression monitoring of glaucoma includes the assessment of functional damage in the visual field as well as examination of the structural damage in the retina. Functional damage is commonly evaluated with standard automated perimetry (SAP) which tests local retinal sensitivity by measuring responses to optical stimuli. Due to its subjective nature, SAP suffers from high variability of the results which may greatly confound the interpretation of the test [5–7] and make progression analysis very difficult [8–10]. Structural integrity of the retina is assessed by optical coherence tomography (OCT) imaging modality [11–14]. From obtained OCT scans, various properties retinal layers, such as thickness or intensity, can be extracted [15–17]. For glaucoma, the retinal nerve fiber layer (*RNFL*), which contains the ganglion cell axons, is of specific interest [18]. Current clinical practice is commonly limited to examination of peripapillary scans of the *RNFL* (*ppRNFL*) thickness, at approximately 1.7 mm from the center of the optic nerve head (ONH), to assess glaucomatous damage.

Several studies have indicated that patients can present structural changes in the *RNFL* before any detectable changes in SAP [19–21]. On the other hand, there are studies that show evidence of functional deterioration without any measurable changes in the currently performed structural tests [22]. This clearly illustrates the need for combining structural and functional information as it may provide valuable input into glaucoma detection and progression monitoring [23, 24].

Establishing a reliable correlation between information about structural and functional damage in the retina is therefore of critical importance in glaucoma management. Many studies have proven that it is challenging to combine this information into a single structure-function correlation [25–28]. Resulting structure-function correlations are generally weak and several factors, such as within and between test-variability and biological variability of the glaucomatous damage are thought to play a role [29–32]. As reduction in the variability of SAP is generally difficult (requires modifications of currently used procedure and test algorithms or acquisition of more data) [33], using more of the available information from OCT images [34, 35] may prove beneficial to improve the structure-function correlation and could help clinicians understand the fundamental changes that lead to glaucomatous damage.

Current structural examination of glaucomatous damage in the retina is limited to the thickness properties of *RNFL* in a narrow circular band around the optic nerve head (ONH). With the increase in scanning speed of modern OCT systems it has become feasible to use volumes scan and consequently create enface thickness maps that cover the entire scan area. Indeed, the benefit of examination of a larger area in the retina for glaucoma diagnosis was already indicated [36]. However, these enface maps have not yet been used in their full potential to detect glaucomatous damage resulting in a loss of clinically relevant information. Furthermore, in addition to the standard thickness measurements, other OCT-derived retinal properties may contain clinically useful information.

Several published studies introduced different techniques that extract quantitative information from the OCT signal, and showed their potential as new diagnostic methods or biomarkers for glaucoma [37–40]. In these studies, changes in the optical tissue properties are associated with the structural state of the tissue [41–44]. Pons et al. showed that the *RNFL* has a decreased reflectivity (mean OCT signal within *RNFL*) in eyes affected by glaucoma [45]. However, the interpretation of OCT signal is not straightforward and is highly dependent on many factors such as the intensity of the light beam or its shape and focus. Recent studies introduced a model that relates OCT signal to attenuation coefficient (AC) of the tissue [46–50]. The *RNFL* AC describes how much of the OCT light is scattered and/or absorbed within the *RNFL* [47] (e.g. a highly attenuating structure has a high AC). As an optical property of the tissue, ACs are easier to interpret than the raw OCT data as they are less affected by imaging artefacts [49]. The potential of using AC to detect glaucoma was shown by earlier studies in which *RNFL* AC values were reduced in eyes affected by glaucoma when compared to normal eyes [50]. In addition to showing different optical properties between diseased and healthy eyes, when presented in an enface image the AC values were shown to vary within a single scan which may or may not coincide with thickness changes [46].

In this study, we visually determined and scored correlations between local glaucomatous damage in both AC *RNFL* and *RNFL* thickness maps with areas of decreased retinal sensitivity in the corresponding visual field maps. The optical properties and thickness of the *RNFL* are exploited over the whole OCT volume scan and thus a significantly larger percentage of the available information in the volume scan was used when compared to the current clinical practice. We hypothesized that the *RNFL* AC information that we extracted from the standard OCT images may not coincide with information extracted from the *RNFL* thickness measurements. Thus, a direct comparison between the scored correlation of the defects in the *RNFL* AC and *RNFL* thickness maps with the corresponding visual fields was performed. The main goal of the paper is to determine whether AC could provide additional insight into glaucomatous damage when compared to OCT thickness maps.

5.2. Methods

Several steps were performed to analyze the correlation between OCT derived *RNFL* thickness and AC maps with corresponding visual field maps, in patients affected by glaucoma. In brief, patients first needed to be selected and both OCT scans and visual fields acquired. Second, the acquired OCT scans were processed with our previously developed segmentation software [51] to obtain the boundaries that enclose the *RNFL* after which the AC and thickness maps of the *RNFL* were created. Third, manual annotations of the visible defects in OCT derived maps as well as visual fields were performed by a medical doctor. Four, the correlation between the annotated defects in OCT derived maps and annotated defects in visual fields was scored.

The procedure of patient selection, OCT data acquisition and visual field acquisition are described in section 5.2.1, 5.2.2 and 5.2.3, respectively. Automatic processing performed on OCT scans is described in section 5.2.4. Manual annotation of defects and the correlation analysis are described in section 5.2.5.

5.2.1. Subjects and data selection

The study population consisted of glaucoma patients enrolled in a longitudinal prospective study called the Rotterdam Glaucoma Imaging Study. The patients visited the Glaucoma Service of the Rotterdam Eye Hospital every 6 or 12 months for their standard clinical checkup. Both eyes of all participants were measured with a spectral domain (SD) OCT (Spectralis OCT, Heidelberg Engineering GHmB, Heidelberg, Germany) and standard automated perimetry (Humphrey field analyzer (HFA) 24-2 SITA Standard, Carl Zeiss Meditec, Dublin CA, USA). The most recent visit of the participants was selected for this paper. If the measurements met the device specific quality criteria (described in more detail in the following two subsections), they were included in the study. If the quality of any of the most recent measurements was considered poor, the previous visit of that participant was used. Both eyes of a single participant were included if they met the inclusion criteria. There was no selection of patients based on the stage of the glaucomatous damage — very mild but also advanced glaucoma are therefore represented in this study. A total of 178 eyes was included in this study. The patients received pressure regulating drugs and if necessary surgery was performed, including implant surgery. Cataract surgery was allowed but after cataract surgery the subjects were excluded for a one year period in order to ensure that the eye has fully recovered from the procedure. Other ocular surgery or any co-morbidity in the form of other ocular or systemic diseases, such as diabetes, were not allowed. All participants in the study signed written informed consent. The study met all commitments under the Declaration of Helsinki and Good Clinical Practice (GCP) guidelines and was approved by the Medical Ethics Committee of the Erasmus Medical Center, Rotterdam, The Netherlands.

5.2.2. Optical coherence tomography data

20°x20° volumetric OCT scans were acquired with the image centered on the optic nerve head (ONH). The scanning protocol acquired a volume containing of 193 B-scans of 512 A-scans of 496. The system employed an eye-tracker and was set to average five B-scans before moving to the next B-scan. The scan was considered of poor quality if the Spectralis OCT scan quality score was below 20dB. Furthermore, each individual scan was subjected to a visual inspection and monitored for unexpected ocular pathology. Poorly centered scans (ONH not centered in the image), so-called ”cut scans” (in which a portion of the retina does not fall within the acquisition window) and scans with large intensity differences caused by differences in the scanning depth were excluded.

5.2.3. Standard automated perimetry data

Standard automated perimetry (HFA 24-2 SITA standard test algorithm) was used to measure the visual field integrity of each participant. Only measurements with fixation losses, false positives and false negatives under 20% were considered reliable. If the percentage was higher, the measurement was excluded and replaced by an earlier visit.

5.2.4. Automatic processing

The raw SD-OCT images were automatically converted into AC images [46]. Afterwards, the interfaces between retinal layers were segmented by using a previously presented level set based segmentation method developed for healthy and glaucoma affected eyes [51]. For this study, only those interfaces that enclose the *RNFL* (*vitreous - RNFL* and *RNFL - ganglion cell layer (GCL)*) interface were of interest. Based on the obtained segmentation, enface AC and thickness maps were derived. Enface *RNFL* AC maps were created from the mean AC value within the *RNFL* along every A-scan. Further, enface *RNFL* thickness maps were created by measuring the distance along each A-scan from the *vitreous - RNFL* interface to the *RNFL - GCL* interface.

5.2.5. Correlation methodology and statistics

Local glaucomatous defects in OCT derived maps (both thickness and AC) and corresponding visual fields were visually identified and manually annotated by a medical doctor. Annotations performed on OCT derived thickness and AC maps were then transformed to a standardized template, thereby masking the origin of the annotations. This made annotations from AC maps indistinguishable from those made on thickness maps. Finally, the defects on the OCT templates were matched with defects in the visual fields and vice versa and the correlation was qualitatively scored.

Within each OCT derived map the annotator searched for the local wedge shaped *RNFL* defects representative of glaucomatous damage [4, 52, 53]. Defects had to follow the trajectory of the retinal nerve fibers [54] and had to be continuous to the ONH border. Once a defect was identified, it was annotated (ITK-SNAP, freely available at `http://www.itksnap.org`). No limit was set on the number of defects that could be annotated within a single map. The scans were processed in batches of 30 scans. In each batch, first all *RNFL* AC maps were annotated, followed by the annotations on the *RNFL* thickness maps. Next, these annotations were translated into a standardized template. This template offers only information on the width and the location of the defect at 1.4 mm from the center of the optic nerve head. In this manner, the *RNFL* AC and *RNFL* thickness annotations became indistinguishable from each other and masked grading in the next step of the analysis was ensured. An example of the manual annotations and the standardized template is shown in Figure 5.1.

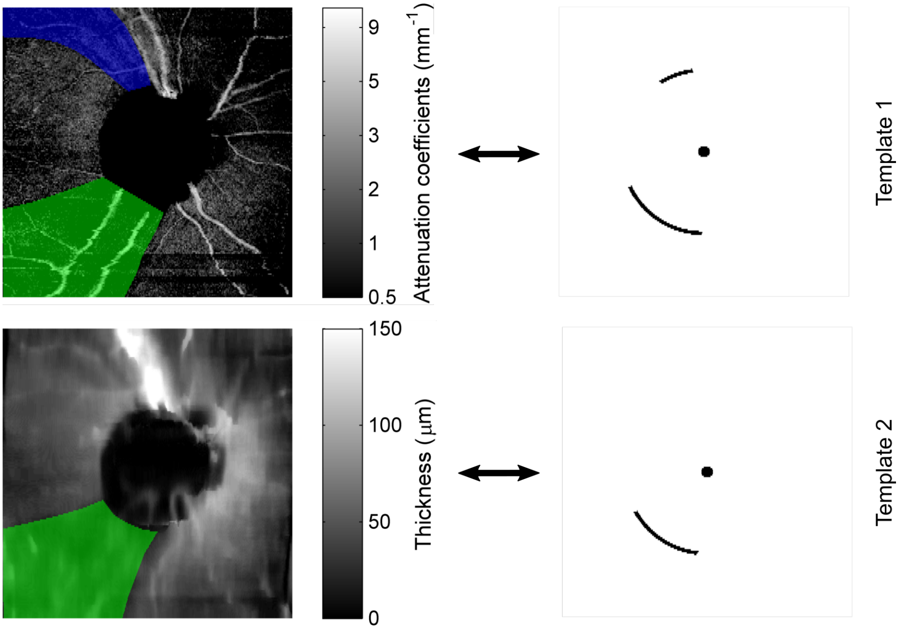

Figure 5.1: Example of the used *RNFL* AC and *RNFL* thickness maps with annotated defects. The annotations of defects were translated to a standardized template to ensure masked grading between the structural defects and those found in the visual fields. The template shows only information on the width and location of the defect at 1.4 mm from the center of the optic nerve head.

The visual field data was processed in a comparable manner. The total deviation probability map of the HFA test report was as used as a template for the annotation of local visual field defects. When performing the annotations, the medical doctor was allowed to use all the available information on the HFA report to determine the size and boundaries of the local defects. Prior knowledge of common shapes of visual field defects in glaucoma was incorporated to define the edges of the local defects [53]. If a point on the deviation probability map was $p < 0.5$, then it was marked. No limit was set on the number of defects that could be annotated within a single field. Because the annotation of structural and functional defects was done independently from each other, the number of annotated defects in the OCT maps and VF maps could differ.

Finally, each defect on the OCT templates was visually matched with a defect in the corresponding visual fields and vice versa. Each of the matches was then graded as 1: probable correlation, 2: possible correlation, 3: questionable correlation or 4: unlikely correlation. A fifth score, 'NA', was used when there was a defect present on the RNLF AC or thickness map, but no corresponding defect was found on VF. The matching and grading process resulted in two lists of graded correlations; one with the scores for the *RNFL* AC – VF correlation and another with the scores for the *RNFL* thickness – VF correlation. Additionally, to determine whether there is statistically significant difference between the graded correlation of defects found

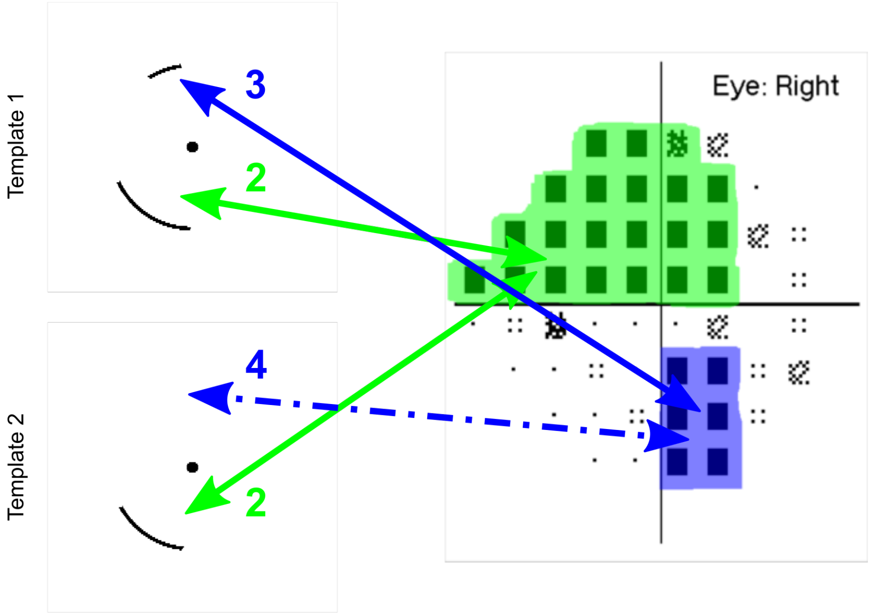

Figure 5.2: Illustration of the scoring procedure between the standarized templates and defects annoted on the visual field. The first template has two defects, whereas the second one shows only one defect. The green defect was scored as a 'possible correlation' for both templates. The defect annotated in blue has a corresponding defect only in the first templates where it was scored as 'questionable'. In the second template, no convincing defect was found thus the correlation was scored as 'unlikely'.

on AC and thickness maps, the Wilcoxon Signed Ranks test was performed. All p-values below 5% were considered as statistically significant. Finally, a confusion matrix of the correlation scores was calculated.

5.3. Results

The presented methodology allows a direct comparison between the correlation of the local *RNFL* defects in the *RNFL* AC and *RNFL* thickness maps with the defects in visual fields. For each included eye the agreement between the defects in the visual field and the corresponding defects in the OCT derived maps was determined by a score on a scale of 1 (good correlation) to 4 (poor correlation). To clarify the presented methods and outcome parameters, an individual case is illustrated in Figure 5.2. In this example, there a good agreement between one defect in visual fields and in both OCT derived maps (depicted in green) and a second defect (depicted in blue) visible only in the *RNFL* AC map. The first defect was graded by a score 'possible' (grade 2) for both the *RNFL* AC and *RNFL* thickness map defects. For the second defect, the correlation was weaker and the defect was graded by a score 'questionable' (grade 3) for the *RNFL* AC maps and score 'unlikely correlation' (grade 4) for the *RNFL* thickness map as no defect was visible there.

In total, 178 eyes of glaucoma patients were included and 374 individual correlations were scored. The mean number of defects identified and annotated in the *RNFL* thickness maps, the *RNFL* AC maps and corresponding visual fields were, 1.95, 1.89 and 2.15 respectively. The participants were not selected based on the severity of the glaucomatous damage. This resulted in a standard automated perimetry mean deviation (MD) that ranged from -31.18 to 1.40 with a mean MD of -9.81. The mean age of the participants was 69.15, and 45% of the patients were of female gender.

The results of the correlation between OCT derived maps and visual fields are presented in Figure 5.3. The figure shows the frequency of assigned scores for the correlation of defects between OCT derived maps and visual fields. The x-axis represents the 5 correlation scores and the y-axis represents the frequency of occurrence. Additionally, for each score two bars are shown; one for the *RNFL* AC map and one for the *RNFL* thickness map. Upon visual inspection of Figure 5.3, the percentage of defects assigned to each group appears similar. The data showed a decrease in frequency with an increasing score up to score 4, which comprises nearly half (45%) of the total correlation scores. This means that in almost half of the local defects that were annotated in the OCT derived maps a poor correlation with the VF defects and vice versa was found. In 2.7%, a local defect was found in the OCT derived maps, but no local defect was found in the VF. The percentage of correlation scores 1, 2 and 3 were somewhat higher for *RNFL* thickness compared to *RNFL* AC, with differences of 2.1%, 1.6% and 0.5% respectively. In contrast, the percentage of *RNFL* thickness score 4 was 1.1% lower than *RNFL* AC. These differences indicate that the overall correlation is better between the defects found in the *RNFL* thickness maps and their corresponding VF defects (mean score 2.74),

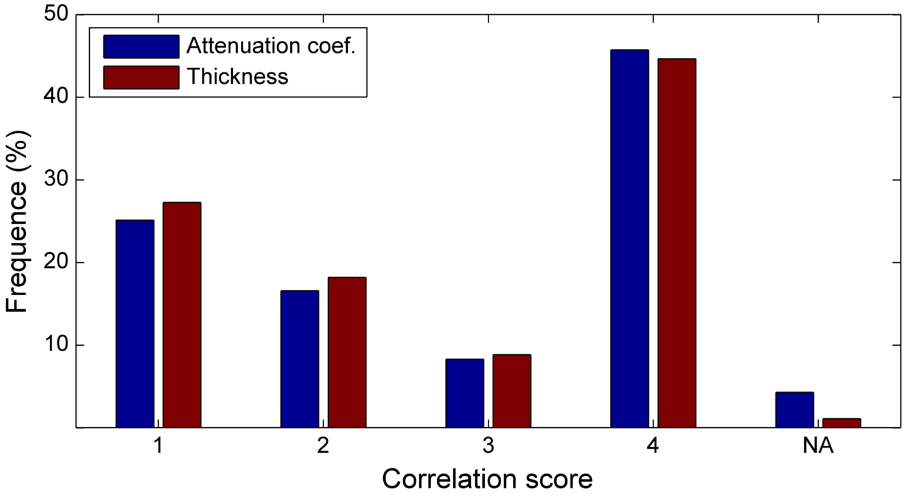

Figure 5.3: Histogram illustrating the frequency of the scores for the *RNFL* AC and *RNFL* thickness correlations with the visual field defects. The data is presented in 5 correlation score groups: 1: probable correlation, 2: possible correlation, 3: questionable correlation, 4: unlikely correlation, and NA: a defect found on either of the OCT maps with no corresponding defect in the VF available to be correlated.

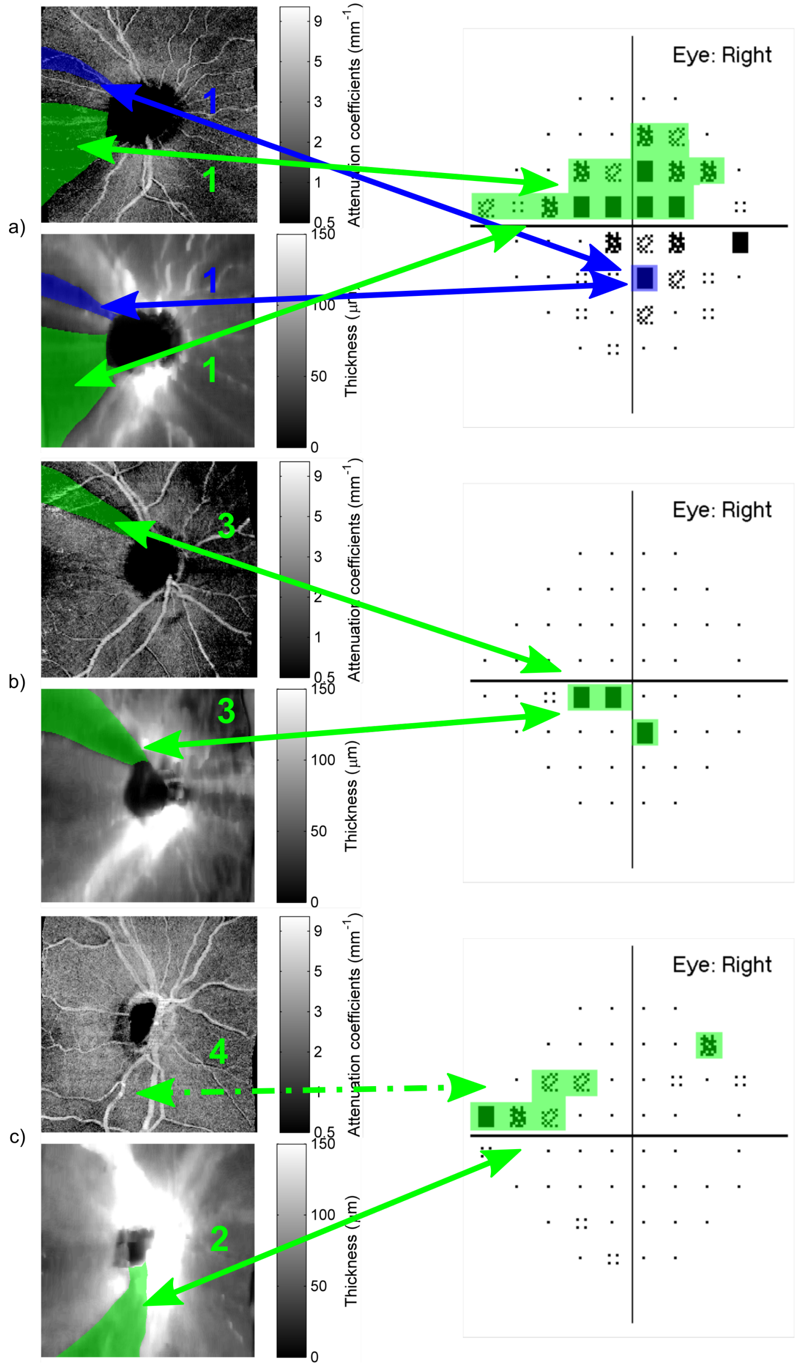
a)
b)
c)
1
1
1
1
3
3
4
2
9
5
3
2
1
0.5
150
100
50
0
Attenuation coefficients (mm^{-1})
Thickness (µm)
Eye: Right
Eye: Right
Eye: Right

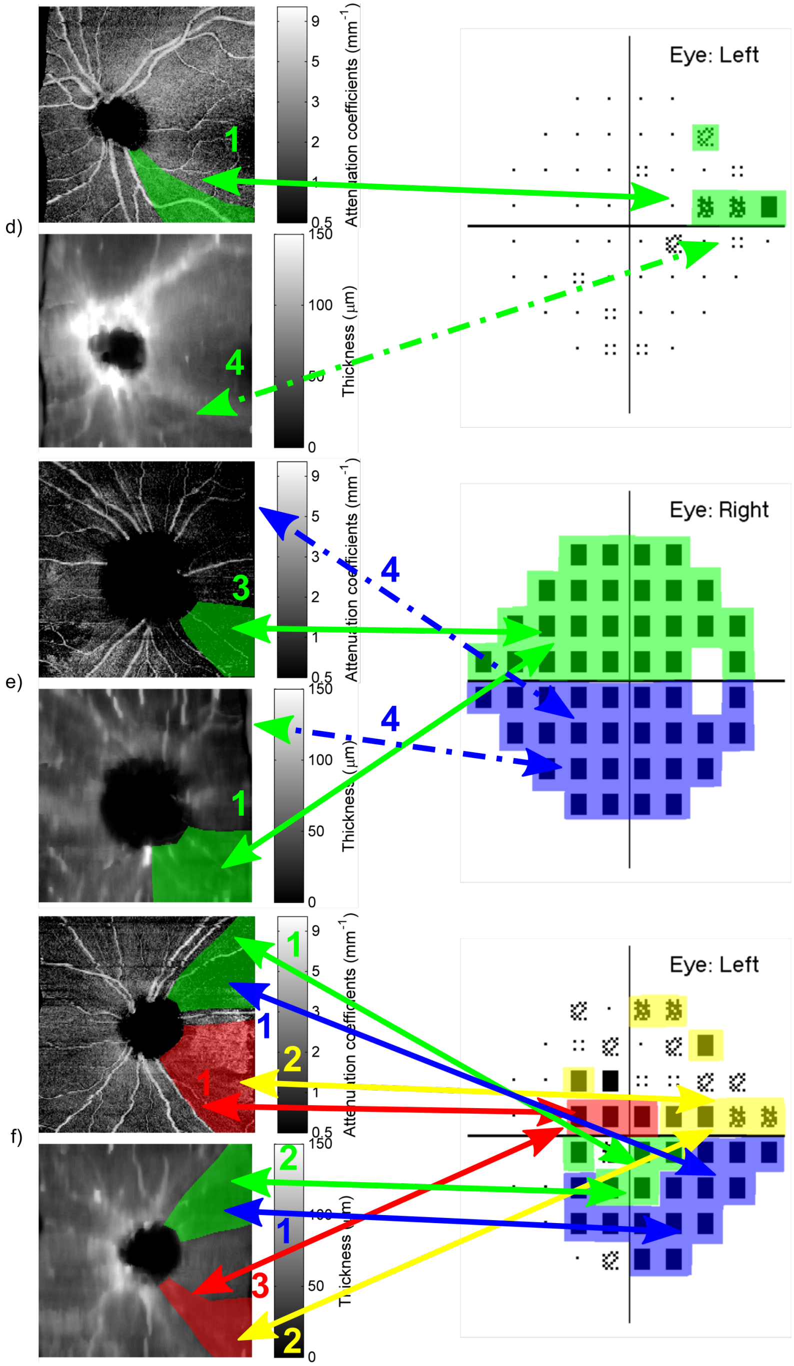
d)
e)
f)
Attenuation coefficients (mm⁻¹)
9
5
3
2
1
0.5
Thickness (µm)
150
100
50
0
Eye: Left
Eye: Right
Eye: Left
1
2
3
4

Figure 5.4: Examples of individual cases with manual annotation in different scoring scenarios (both OCT derived maps and visual fields). a) A good agreement between the structural defects in both OCT derived maps and corresponding VF defect. b) Poor agreement between a structural defect in both OCT maps and corresponding VF defects. c) Good agrement with a structural defect in *RNFL* thickness maps and no defect visible defect in *RNFL* AC maps. d) Good agreement with a structural defect in *RNFL* AC maps and no defect visible in *RNFL* thickness maps. e) Agreement in structural defects in both OCT derived maps with a higher correlation score for a 'green' defect found on the *RNFL* thickness map. f) Agreement in structural defects in both OCT derived maps with a higher correlation score for a 'green' and 'red defect' found on the *RNFL* AC map.

than the defects in the *RNFL* AC maps (mean score 2.87). The Wilcoxon signed - ranks test showed that the difference was statistically significant (p<0.05).

The differences between the two grading scores for the two OCT derived maps were summarized in Table 5.1 by means of a confusion matrix. This confusion matrix visualizes the agreement between each of the paired scores. In 66% (245/374) of the scores, there was an optimal agreement between the two correlation scores. However, in 34% (129/374) of the correlations the AC and thickness scores disagreed. Even in the disagreement cases, the superior performance of the *RNFL* thickness – VF correlation compared to the *RNFL* AC – VF correlation was confirmed (in 57% (74/129) of the disagreement cases *RNFL* thickness had a higher correlation score than the *RNFL* AC). More interesting, in almost half of the disagreement cases (43%; 55/129) the *RNFL* AC – VF maps performed better and seem to hold additional information that may be used to improve the structure-function correlations in glaucoma.

Different levels of disagreement between the correlation scores were identified. Examples of disagreement in correlation scores are presented in Figure 5.4. The most extreme mismatches occurred 20 times. In these cases, a correlation pair for *RNFL* thickness – VF was identified but either the structural or the functional defect was missing for the *RNFL* AC – VF correlation (16 cases), and vice versa (4 cases). In all other disagreement cases (109 cases), defects were found in both maps, but either *RNFL* thickness or *RNFL* AC received a higher score.

5.4. Discussion and conclusion

With the proposed approach, by visually locating and grading defects, the experimental possibilities and limitations of OCT AC images were explored leading to speculations on the clinical possibilities of this method. The correlations between defects in the OCT derived maps and the VF defects were used to assess the individual ability of *RNFL* thickness and *RNFL* AC to detect defects in the visual field.

A general conclusion is that, within the used dataset, AC were not as effective in detecting glaucomatous damage as the thickness. The *RNFL* thickness outperformed *RNFL* AC based on the mean score. However, our results indicate that *RNFL* AC may improve the structure-function correlation in glaucoma. The correlation scores were better for *RNFL* AC in 55 cases (43%) of the 129 correlations that disagreed. In other words; in 55 cases the structural defects in the OCT images were easier (or better) to identify when we used the *RNFL* AC maps. This may

Table 5.1: Confusion matrix showing the number of correlation scores for each combination of *RNFL* thickness and *RNFL* AC. In 245/374 or 66% of the scores (in bold) both correlation scores received the same grade. In 129 cases, the scores disagreed. In 57% (74/129; marked with blue) of the scores that disagreed the *RNFL* thickness did better, whereas in 43% (55/129 marked with red) of the cases, the *RNFL* AC – VF correlation performed better.

		AC score				
		1	2	3	4	NA
Thickness score	1	**66**	15	3	16	2
	2	16	**32**	4	12	4
	3	2	7	**16**	8	0
	4	10	8	8	**131**	10
	NA	0	0	0	4	

lead to a conclusion that the *RNFL* AC maps contain useful information not visible within *RNFL* thickness maps. However, future work is needed to evaluate if and how information from *RNFL* AC and *RNFL* thickness can be combined to enhance the overall structure-function correlation. The combination of thickness information with information based on the optical properties of the *RNFL* has shown to be of value before. Gardiner et al. showed that there is a correlation between the rate of damage seen on the VF of glaucoma patients and a combined value of *RNFL* thickness with the amount of specular reflectivity derived from the OCT signal [40].

Visual comparison of the *RNFL* AC and *RNFL* thickness maps indicates differences in the size and location of the annotated defects. These differences could be caused by either intra grader variability or by differences between the amount of lost *RNFL* (as represented by the *RNFL* thickness maps) and changes in optical properties of the *RNFL* (axon loss and possibly other cellular processes, as expressed by *RNFL* AC maps). Currently it is unclear what these cellular processes exactly comprise. We believe that the thinning of the *RNFL* occurs after the initial damage to the *RNFL* and that the thinning may therefore be preceded by processes that change the *RNFL* AC values. In other words; possibly *RNFL* AC visualizes the active process of local damage.

The procedure of visual identification and the subjective scoring of each of the correlations, which may be biased by intra grader variability, might be considered as a limitation of the performed study. Since all gradings, of both thickness and AC images, were performed by a single grader, the variability is expected to be approximately the same in all the images and the influence on the outcome of the correlation is assumed to be minimal. In future studies, the intra and, if applicable, inter grader variability should be addressed before making any definitive conclusions on the clinical applicability. Further, our most important finding is directly linked to the used approach (visual identification and subjective scoring); more structural defects would have been detected if we used all available information from the VF, thickness and AC maps. In 55 cases, the identification of structural defects would have been more comprehensive if the information extracted from the *RNFL* AC maps was used in addition to *RNFL* thickness data.

This explorative study paves the way for future studies. Whether *RNFL* AC images could help investigators understand the etiology of glaucoma is unclear. We speculate that that thinning of the *RNFL* due to glaucoma is preceded by changes in the optical properties within the *RNFL* and other layers of the retina. The actual loss of axons is the result of programmed cell death [55] and this loss is likely to be preceded by a loss of function. The correlation between the optical properties of the *RNFL* in a specific region of the retina and the function in this region has not yet been established. We speculate that *RNFL* AC images could detect so called pre-perimetric damage before thinning of the *RNFL* occurs [38, 40]. This should be addressed by using longitudinal data.

References

[1] WHO, *Visual impairment and blindness,* (2014).

[2] D. Pascolini and S. P. Mariotti, *Global estimates of visual impairment: 2010,* British Journal of Ophthalmology **96**, 614 (2012).

[3] X. Tham, Y.-C.and Li, T. Y. Wong, H. A. Quigley, T. Aung, and C.-Y. Cheng, *Global prevalence of glaucoma and projections of glaucoma burden through 2040,* Ophthalmology **121**, 2081 (2014).

[4] H. A. Quigley, *Glaucoma,* The Lancet **337**, 1367 (2011).

[5] A. Heijl, G. Lindgren, and J. Olsson, *Normal variability of static perimetric threshold values across the central visual field,* Archives of Ophthalmology **105**, 1544 (1987).

[6] A. V. Turalba and C. Grosskreutz, *A review of current technology used in evaluating visual function in glaucoma,* Seminars in Ophthalmology **25**, 309 (2010).

[7] P. G. D. Spry, C. A. Johnson, A. M. McKendrick, and A. Turpin, *Variability components of standard automated perimetry and frequency-doubling technology perimetry,* Investigative Ophthalmology and Visual Science **42**, 1404 (2001).

[8] S. Gardiner, S. Demirel, M. O. Gordon, and M. A. Kass, *Ocular hypertension treatment study group. Seasonal changes in visual field sensitivity and intraocular pressure in the ocular hypertension treatment study,* Ophthalmology **120**, 724 (2013).

[9] R. A. Russell, D. P. Crabb, R. Malik, and D. F. Garway-Heath, *The relationship between variability and sensitivity in large-scale longitudinal visual field datavf variability and sensitivity,* Investigative Ophthalmology and Visual Science **53**, 5985 (2012).

[10] A. Turpin and A. M. McKendrick, *What reduction in standard automated perimetry variability would improve the detection of visual field progression?* Investigative Ophthalmology and Visual Science **52**, 3237 (2011).

[11] D. Huang, E. A. Swanson, C. P. Lin, J. S. Schuman, W. G. Stinson, W. Chang, M. R. Hee, T. Flotte, K. Gregory, C. A. Puliafito, and et al., *Optical coherence tomography,* Science **254**, 1178 (1991).

[12] T. C. Chen, A. Zeng, W. Sun, M. Mujat, and J. F. de Boer, *Spectral domain optical coherence tomography and glaucoma,* International Ophthalmology Clinics **48**, 29 (2008).

[13] I. I. Bussel, G. Wollstein, and J. S. Schuman, *OCT for glaucoma diagnosis, screening and detection of glaucoma progression,* British Journal of Ophthalmology **98**, ii15 (2014).

[14] C. P. Gracitelli, R. Y. Abe, and F. A. Medeiros, *Spectral-domain optical coherence tomography for glaucoma diagnosis,* Open Ophthalmology Journal **9**, 68 (2015).

[15] C. Y. Cheung, C. K. Leung, D. Lin, C. P. Pang, and D. S. Lam, *Relationship between retinal nerve fiber layer measurement and signal strength in optical coherence tomography,* Ophthalmology **115**, 1347 (2008).

[16] J. Dwelle, S. Liu, B. Wang, A. McElroy, D. Ho, M. K. Markey, T. Milner, and I. H. G. Rylander, *Thickness, phase retardation, birefringence, and reflectance of the retinal nerve fiber layer in normal and glaucomatous non-human primates,* Investigative Ophthalmology and Visual Science **53**, 4380 (2012).

[17] D. C. Hood and A. S. Raza, *On improving the use of OCT imaging for detecting glaucomatous damage,* The British Journal of Ophthalmology **98**, ii1 (2014).

[18] H. L. Rao, L. M. Zangwill, R. N. Weinreb, P. A. Sample, L. M. Alencar, and F. A. Medeiros, *Comparison of different spectral domain optical coherence tomography scanning areas for glaucoma diagnosis,* Ophthalmology **117**, 1692 (2010).

[19] R. S. Harwerth, A. S. Vilupuru, N. V. Rangaswamy, and E. L. Smith, III, *The relationship between nerve fiber layer and perimetry measurements,* Investigative Ophthalmology and Visual Science **48**, 763 (2007).

[20] J. W. Jeoung, T.-W. Kim, R. N. Weinreb, S. H. Kim, K. H. Park, and D. M. Kim, *Diagnostic ability of spectral-domain versus time-domain optical coherence tomography in preperimetric glaucoma,* Journal of Glaucoma **23**, 299 (2014).

[21] R. Lisboa, M. T. Leite, L. M. Zangwill, A. Tafreshi, R. N. Weinreb, and F. A. Medeiros, *Diagnosing preperimetric glaucoma with spectral domain optical coherence tomography,* Ophthalmology **119**, 2261 (2012).

[22] F. A. Medeiros, L. M. Zangwill, C. A. Girkin, J. M. Liebmann, and R. N. Weinreb, *Combining structural and functional measurements to improve estimates of rates of glaucomatous progression,* American Journal of Ophthalmology **153**, 1197 (2012).

[23] F. A. Medeiros, M. T. Leite, L. M. Zangwill, and R. N. Weinreb, *Combining structural and functional measurements to improve detection of glaucoma progression using bayesian hierarchical models,* Investigative Ophthalmology and Visual Science **52**, 5794 (2011).

[24] F. A. Medeiros, L. M. Zangwill, C. A. Girkin, J. M. Liebmann, and R. N. Weinreb, *Combining structural and functional measurements to improve estimates of rates of glaucomatous progression,* American Journal of Ophthalmology **153**, 1197 (2012).

[25] A. Anton, N. Yamagishi, L. Zangwill, P. A. Sample, and R. N. Weinreb, *Mapping structural to functional damage in glaucoma with standard automated perimetry and confocal scanning laser ophthalmoscopy,* American Journal of Ophthalmology **125**, 436 (1998).

[26] C. Y. Mardin, A. Peters, F. Horn, A. G. Junemann, and B. Lausen, *Improving glaucoma diagnosis by the combination of perimetry and HRT measurements,* Journal of Glaucoma **15**, 299 (2006).

[27] R. Lisboa, R. N. Weinreb, and F. A. Medeiros, *Combining structure and function to evaluate glaucomatous progression: Implications for the design of clinical trials,* Current opinion in pharmacology **13**, 115 (2013).

[28] A. S. Raza, X. Zhang, C. G. V. De Moraes, C. A. Reisman, J. M. Liebmann, R. Ritch, and D. C. Hood, *Improving glaucoma detection using spatially correspondent clusters of damage and by combining standard automated perimetry and optical coherence tomography,* Investigative Ophthalmology and Visual Science **55**, 612 (2014).

[29] D. C. Hood, S. C. Anderson, M. Wall, A. S. Raza, and R. H. Kardon, *A test of a linear model of glaucomatous structure–function loss reveals sources of variability in retinal nerve fiber and visual field measurements,* Investigative Ophthalmology and Visual Science **50**, 4254 (2009).

[30] J. R. Lee, J. W. Jeoung, J. Choi, J. Y. Choi, K. H. Park, and Y. Kim, *Structure–function relationships in normal and glaucomatous eyes determined by time- and spectral-domain optical coherence tomography,* Investigative Ophthalmology and Visual Science **51**, 6424 (2010).

[31] S. K. Gardiner, B. Fortune, and S. Demirel, *Signal-to-noise ratios for structural and functional tests in glaucoma,* Translational Vision Science and Technology **2**, 6424 (2013).

[32] M. Araie, *Test-retest variability in structural parameters measured with glaucoma imaging devices,* Japanese Journal of Ophthalmology **57**, 1 (2013).

[33] A. Turpin and A. M. McKendrick, *What reduction in standard automated perimetry variability would improve the detection of visual field progression?* Investigative Ophthalmology and Visual Science **52**, 3237 (2011).

[34] C. K. Leung, N. Choi, R. N. Weinreb, S. Liu, C. Ye, L. Liu, G. W. Lai, J. Lau, and D. S. Lam, *Retinal nerve fiber layer imaging with spectral-domain optical coherence tomography: pattern of RNFL defects in glaucoma.* Ophthalmology **117**, 2337 (2010).

[35] D. C. Hood, B. Fortune, M. A. Mavrommatis, J. Reynaud, R. Ramachandran, R. Ritch, R. B. Rosen, H. Muhammad, A. Dubra, and T. Y. P. Chui, *Details of glaucomatous damage are better seen on OCT en face images than on OCT retinal nerve fiber layer thickness maps,* Investigative Ophthalmology and Visual Science **56**, 6208 (2015).

[36] H. Simavli, C. J. Que, A. Akduman, J. L. Rizzo, E. Tsikata, J. F. de Boer, and T. C. Chen, *Diagnostic capability of peripapillary retinal thickness in glaucoma using 3D volume scans,* American Journal of Ophthalmology **159**, 545 (2015).

[37] R. W. Knighton and X. R. Huang, *Directional and spectral reflectance of the rat retinal nerve fiber layer,* Investigative Ophthalmology and Visual Science **40**, 639 (1999).

[38] B. Fortune, C. F. Burgoyne, G. Cull, J. Reynaud, and L. Wang, *Onset and progression of peripapillary retinal nerve fiber layer (RNFL) retardance changes occur earlier than RNFL thickness changes in experimental glaucoma,* Investigative Ophthalmology and Visual Science **54**, 5653 (2013).

[39] S. Liu, B. Wang, B. Yin, T. E. Milner, M. K. Markey, S. J. McKinnon, and H. G. Rylander, III, *Retinal nerve fiber layer reflectance for early glaucoma diagnosis,* Journal of glaucoma **23**, 5653 (2014).

[40] S. K. Gardiner, S. Demirel, J. Reynaud, and B. Fortune, *Changes in retinal nerve fiber layer reflectance intensity as a predictor of functional progression in glaucoma,* Investigative Ophthalmology and Visual Science **57**, 1221 (2016).

[41] R. W. Knighton and Q. Zhou, *The relation between the reflectance and thickness of the retinal nerve fiber layer,* Journal of Glaucoma **4**, 117 (1995).

[42] F. J. van der Meer, D. J. Faber, M. C. Aalders, A. A. Poot, I. Vermes, and T. G. van Leeuwen, *Apoptosis- and necrosis-induced changes in light attenuation measured by optical coherence tomography,* Lasers in Medical Science **25**, 259 (2010).

[43] X. R. Huang, Y. Zhou, W. Kong, and R. W. Knighton, *Change of retinal nerve fiber layer reflectance correlated with cytostructural change in glaucoma,* Investigative Ophthalmology and Visual Science **52**, 2442 (2011).

[44] X.-R. Huang, Y. Zhou, W. Kong, and R. W. Knighton, *Reflectance decreases before thickness changes in the retinal nerve fiber layer in glaucomatous retinas,* Investigative Ophthalmology and Visual Science **52**, 6737 (2011).

[45] M. E. Pons, H. Ishikawa, R. Gürses-Ozden, J. M. Liebmann, H. L. Dou, and R. Ritch, *Assessment of retinal nerve fiber layer internal reflectivity in eyes with and without glaucoma using optical coherence tomography,* Archives of Ophthalmology **118**, 1044 (2000).

[46] K. A. Vermeer, J. van der Schoot, H. G. Lemij, and J. F. de Boer, *RPE-normalized RNFL attenuation coefficient maps derived from volumetric OCT imaging for glaucoma assessment,* Investigative Ophthalmology and Visual Science **53**, 6102 (2012).

[47] K. A. Vermeer, J. Mo, J. J. A. Weda, H. G. Lemij, and J. F. de Boer, *Depth-resolved model-based reconstruction of attenuation coefficients in optical coherence tomography,* Biomedical optics Express **5**, 322 (2014).

[48] S. Kaushik, S. Mulkutkar, S. S. Pandav, N. Verma, and A. Gupta, *Comparison of event-based analysis of glaucoma progression assessed subjectively on visual fields and retinal nerve fibre layer attenuation measured by optical coherence tomography,* International Ophthalmology **35**, 95 (2015).

[49] K. A. Vermeer, J. van der Schoot, H. G. Lemij, and J. F. de Boer, *Retinal nerve fiber layer attenuation maps derived from volumetric OCT data,* Investigative Ophthalmology and Visual Science **53**, 798 (2012).

[50] J. van der Schoot, K. A. Vermeer, J. F. de Boer, and H. G. Lemij, *The effect of glaucoma on the optical attenuation coefficient of the retinal nerve fiber layer in spectral domain optical coherence tomography images,* Investigative Ophthalmology and Visual Science **53**, 2424 (2012).

[51] J. Novosel, G. Thepass, H. G. Lemij, J. F. de Boer, K. A. Vermeer, and L. J. van Vliet, *Loosely coupled level sets for simultaneous 3D retinal layer segmentation in optical coherence tomography,* Medical Image Analysis **26**, 146 (2015).

[52] K. H. Mok, V. W. Lee, and K. F. So, *Retinal nerve fiber loss pattern in high-tension glaucoma by optical coherence tomography.* Journal of Glaucoma **12**, 255 (2003).

[53] R. R. Allingham, K. F. Damji, S. Freedman, S. E. Moroi, and D. J. Rhee, *Shields Textbook of Glaucoma* (Wolters Kluwer/Lippincott Williams and Wilkins, 2011).

[54] N. M. Jansonius, J. Schiefer, J. Nevalainen, J. Paetzold, and J. Schiefer, *A mathematical model for describing the retinal nerve fiber bundle trajectories in the human eye: Average course, variability, and influence of refraction, optic disc size and optic disc position,* Experimental Eye Research **105**, 70 (2012).

[55] H. A. Quigley, *Neuronal death in glaucoma,* Progress in Retinal and Eye Research **18**, 39 (1999).

6

Discussion and conclusion

An efficient way to prevent, diagnose or treat eye diseases includes examination of the retina and the extraction of quantitative imaging biomarkers. By means of optical coherence tomography (OCT), the retina can be visualized and investigated in vivo. Three-dimensional structural information about the thickness of a certain layer, its presence or attenuation coefficient values as well as presence or absence of lesions provide valuable input for disease diagnosis, prognosis and/or monitoring. Manual extraction of these image-based biomarkers is time consuming and tedious. Thus, in this thesis we present and evaluate automatic techniques for segmentation of retinal structure.

6.1. Technical developments

In **Chapter 2**, a loosely coupled level set method that simultaneously segments multiple interfaces between layers of the retina is described. The method is based on a level set approach which uses Bayesian inference and through which image data is combined with prior knowledge about the retina. Within the method a novel coupling approach is presented, which exploits anatomical knowledge about the order of the layers in the retina to ensure anatomically correct segmentation results. Both the accuracy and reproducibility of the method were evaluated, as well as the robustness to segment different data types. A good agreement between manual and automatic segmentation was found: the mean unsigned error (MUD) for all interfaces in all data types varied between 1.9 and 8.5 µm. The reproducibility of automatic segmentation was in the same ranges as the reproducibility of manual annotators. Finally, the developed segmentation method performs at least as good as the manual annotator, as the accuracy of the automatic segmentation was similar to the reproducibility of a manual annotator.

In **Chapter 3**, a method to jointly segment retinal layers and lesions in eyes with topology-disrupting retinal diseases is presented. The method extends and generalizes the existing loosely coupled level set framework, as it can handle local intensity variations as well as the presence or absence of pathological structures in the retina. In this generic framework, lesions are modelled as an additional space-variant layer delineated by auxiliary interfaces and the segmentation of interfaces is steered by local differences in the signal between adjacent retinal layers. The accuracy of both interfaces and lesion segmentation was evaluated on eyes affected by central serous retinopathy and age-related macular degeneration. Additionally, accuracy of interface segmentation was evaluated on eyes without topology-disrupting retinal diseases. The developed approach performed well with a MUD between 3.0 and 12.5 µm for interface segmentation in all data types and a Dice coefficient of 0.73 for drusen segmentation and 0.92 for fluid pockets segmentation.

In **Chapter 4**, a method to simultaneously determine the number of visible layers in the outer retina and segment them is presented. The method is based on a model selection approach with a special attention to balance the quality of the fit with model complexity. Layers in the outer retina are modelled as Gaussian functions and several models of the outer retina are considered. The considered models reflect previously reported work on the visibility of layers and their deterioration. The accuracy of the method was evaluated on healthy and retinitis pigmentosa affected eyes. Further, the reproducibility of both automatic method and manual annotations was evaluated on healthy eyes. Overall, a good agreement was found between manual and automatic segmentation with the agreement in determining the number of visible layers over 70 % and a MUD that varied between 2.7 and 6.7 µm. The reproducibility of automatic segmentation was similar to that of manual annotator.

6.2. Clinical application

In **Chapter 5**, the loosely coupled level sets framework from **Chapter 2** was used to obtain segmentation of the interfaces that surround the *retinal nerve fiber layer* (*RNFL*). By using the obtained segmentation, attenuation coefficient and thickness maps of the *RNFL* were created, in which local glaucomatous damage was visually determined. Afterwards, correlations between the local damage in the obtained maps and areas of decreased retinal sensitivity in the corresponding visual fields were scored and a difference between the correlation of visual fields with either attenuation coefficient or thickness maps was evaluated. The overall correlation scores of attenuation coefficients and thickness appear to be similar, however, they differ in a large number of cases and seem to provide complementary information.

6.3. General discussion

This thesis describes automatic segmentation methods for both inner and outer retinal layer and lesion segmentation which were applied to scans of the retina obtained by optical coherence tomography (OCT). The first method, a loosely coupled level set framework, focuses on segmentation of interfaces between retinal layers. The second method, extends the original loosely coupled level set framework to eyes affected by topology-disrupting diseases. The third and final method focuses on the segmentation of outer retinal layer. Finally, an example of clinical application of the loosely coupled level set framework is shown.

The developed methods provide robust and accurate solutions for segmentation of both inner and outer retinal layers and lesions. The approaches were developed such that they combine image data with anatomical knowledge about the retina. During the development of the methods, special attention was given to ensure all imposed prior (anatomical) knowledge was rather simple, intuitive and easily changeable. This is best illustrated within **Chapter 3** where prior knowledge about attenuation coefficients was changed for several layers which clearly indicates how the proposed loosely coupled level set framework can be flexible and adaptable.

Throughout the thesis, the proposed methods were applied to various types of data (diseased and healthy, different area of the eyes and different imaging devices). Overall, the methods were applied to over 300 retinal OCT scans. Not all of the segmented scans were evaluated in a quantitative manner, however, qualitative evaluation indicates that most of the scans were segmented well. Errors may occur in approximately 5 out of 100 volume scans, e.g. in parts of B-scans the *inner nuclear layer - outer plexiform layer* and *outer plexiform layer - outer nuclear layer* interfaces may be segmented higher or the *RNFL - ganglion cell layer* interface lower. This often occured in B-scans which were tilted (in which retinal layers extend over the entire depth range). In such a case, although the roll-off correction was performed, the attenuation coefficients of layers varied considerably within a B-scan which may be the cause of these errors.

There are several potential clinical applications of the proposed methods. For example, by using the segmentation obtained by the original or extended loosely coupled level set framework, retinal surfaces could be visualized and renderings of the retina with highlighted lesion regions obtained. Additional processing of the results could also be performed to show clinical information in a simple manner (e.g. en face thickness maps of different layers). The proposed method for the outer retinal layer segmentation could be used to create en face images with the number of visible layers in the retina which would allow quick examination and detection of pathologies. Further, although thickness is among the most frequently used properties of retinal layers for disease diagnosis and monitoring, other properties may be useful. **Chapter 4** shows how the investigation of attenuation coefficients across the entire scan area provides additional information. Other properties might be useful, such as intensity values of one or more layers (both locally and globally), presence of a certain layer or orientation of the *RNFL* bundles. The proposed properties could also be useful in a case of a follow-up, where one could quickly compare the extent of pathologies and assess progression.

For better management of eye disease, extraction of image-based biomarkers is of utmost importance. To enable quick and accurate extraction, automatic image analysis plays an essential role. This thesis provides the methodology needed to facilitate the extraction of biomarkers and proposes several of them. Any of the proposed biomarkers may provide valuable input into disease progression patterns or aid the disease diagnosis and monitoring procedures.

Summary

Quantitative image-based biomarkers of retinal structures, extracted from 3D scans acquired with optical coherence tomography (OCT) systems, provide clinically useful information and enable valuable input for the diagnostics, prognostics and monitoring of retinal diseases. Manual extraction of these imaging biomarkers is time consuming and tedious. Thus, in this thesis we set out to develop and evaluate automatic techniques for the segmentation of retinal structure which then enable the extraction of image based biomarkers.

Retinal layer thicknesses are among the most frequently used image based biomarkers. To facilitate the extraction of these thickness maps, a novel loosely coupled level set (LCLS) framework is proposed to simultaneously segment interface between retinal layers. The framework employs a flexible coupling, which allows a global optimization of the entire 3D retina and thereby avoids error propagation as may occur in sequential methods. Further, the framework operates on attenuation coefficients and combines image data with prior knowledge about the retina.

Certain retinal pathologies may give raise to additional structures in the retina such as cysts or drusen, which cause serious layer deformation. The original LCLS framework is adapted to deal with such changes in the retina and to jointly segment retinal layers and lesions. In this approach, lesions are modelled as an additional space-variant layer delineated by auxiliary interfaces. In the absence of lesions, the thickness between the auxiliary interfaces reduces to (nearly) zero. Furthermore, the segmentation of interfaces is steered by local differences in signal between adjacent retinal layers thereby allowing the approach to handle local intensity variations.

Retinal diseases can also cause anatomical changes in the outer retinal layers and affect their visibility in OCT images. A method to simultaneously determine the number of visible layers in the outer retina and segment them is proposed. The developed method is based on a model selection approach with special attention given to balance the quality of the fit with model complexity. This will ensure that a more complex model is selected only if sufficiently supported by the data. The proposed approach does not only provide information about the number of visible layers, but also about their position and identification.

The proposed methodology has been developed to aid the process of clinical decision making and gain more insight into disease progression and efficiency of a treatment. An example of possible application of the developed methods is already proposed within this thesis. The correlation between local glaucomatous damage in attenuation coefficient and thickness maps of the retinal nerve fiber layer and areas of decreased retinal sensitivity in visual field maps are visually scored. Afterwards, the difference between the correlation of visual fields with either attenuation co-

efficient or thickness maps was evaluated. The overall correlation scores appear similar, however, they seem to provide complementary information.

Quantitative evaluation of the proposed methods was performed on a variety of data, which include scans of different areas of the eye, different imaging devices as well as scans of healthy and diseased eyes. Several diseases were considered including glaucoma, age-related macular degeneration, central serous retinopathy and retinitis pigmentosa. Automatically obtained results were compared to manual annotations made by medical doctors. A good agreement between the two segmentations was found on all data, with the mean unsigned difference which was mostly between 3 and 8 µm and never more than 13 µm.

Overall, the developed methods provide flexible, robust and accurate solutions for segmentation of both inner and outer retinal layers as well as lesions in both healthy and diseased eyes. The techniques show potential for clinical use and could easily be used to extract various retinal layer properties which could further be used to aid disease diagnosis, prognosis and monitoring.

Samenvatting

Kwantitatieve op afbeeldingen gebaseerde biomarkers van retinale structuren, afgeleid uit 3D scans gemaakt met optische coherentie tomografie (OCT) systemen, leveren klinisch bruikbare informatie op voor de diagnose, prognose en opvolging van retinale aandoeningen. Een handmatige extractie van zulke biomarkers uit afbeeldingen is een tijdrovend en monotoon proces. Daarom hebben we ons in dit proefschrijft de ontwikkeling en evaluatie van automatische technieken voor het segmenteren van retinale structuren tot doel gesteld, waarmee het mogelijk wordt om biomarkers uit afbeeldingen af te leiden.

De dikte van retinale lagen wordt vaak gebruikt als afbeeldings-biomarker. Om het bepalen van deze dikte-kaarten mogelijk te maken wordt een nieuw zwakgekoppeld level set framework (loosely coupled level set; LCLS) geïntroduceerd om gelijktijdig de scheidingen tussen retinale lagen te bepalen. Dit framework gebruikt een flexibele koppeling dat een globale optimalisatie van het hele netvlies in 3D mogelijk maakt en daarmee de propagatie van fouten, zoals dat bij sequentiële methoden kan voorkomen, voorkomt. Daarnaast werkt dit framework op basis van attenuatiecoëfficiënten en wordt data uit de afbeeldingen gecombineerd met voorkennis van het netvlies.

Bepaalde pathologieën kunnen resulteren in nieuwe structuren in het netvlies, zoals cysten en drusen, waardoor de lagen sterk vervormd worden. Het oorspronkelijke LCLS framework is daarom zo aangepast dat het om kan gaan met degelijke veranderingen in het netvlies zodat gelijktijdig de retinale lagen en de laesies gesegmenteerd kunnen worden. In deze methode worden laesies gemodelleerd als een extra, plaats-afhankelijke laag, afgebakend door additionele grenzen. Waar laesies afwezig zijn, nadert de afstand tussen deze additionele grenzen tot nul. Daarnaast wordt de segmentatie van de begrenzingen gedreven door lokale signaalverschillen tussen aangrenzende retinale lagen, waardoor deze methode variaties van de lokale intensiteiten kan opvangen.

Retinale aandoeningen kunnen ook anatomische veranderingen in de buitenste retinale lagen veroorzaken en de zichtbaarheid van die lagen in OCT beelden beïnvloeden. Hiervoor wordt een methode voorgesteld om tegelijkertijd het aantal zichtbare lagen in de buitenste deel van het netvlies te bepalen en deze te segmenteren. De ontwikkelde methode is gebaseerd op een modelselectie waarbij speciaal wordt gelet op het evenwicht tussen hoe goed het model de data beschrijft en de complexiteit van dit model. Hierdoor wordt ervoor gezorgd dat een complexer model uitsluitend wordt geselecteerd als dit voldoende ondersteund wordt door de data. De voorgestelde methode geeft niet alleen informatie over het aantal zichtbare lagen, maar ook over hun positie en identificatie.

De voorgestelde methodologie is ontwikkeld ter ondersteuning van de klinische besluitvorming en om meer inzicht te krijgen in de progressie van een aandoening en de effectiviteit van een behandeling. Een voorbeeld van een mogelijke toepassing van de ontwikkelde methodes wordt voorgesteld in dit proefschrift. De correlaties tussen plaatselijke glaucomateuze schade in kaarten van attenuatiecoëfficiënten en dikte van de retinale zenuwvezellaag en gebieden met afgenomen retinale sensitiviteit in gezichtsvelden werden subjectief beoordeeld. Vervolgens werd het verschil van correlatie van gezichtsvelden met attenuatiecoëfficiënt- of diktekaarten geëvalueerd. Gemiddeld zijn de correlatiescores vergelijkbaar, maar ze lijken complementaire informatie te bevatten.

Een kwantitatieve evaluatie van de voorgestelde methodes werd uitgevoerd op verschillende data sets, waaronder scans van verschillende delen van het oog, verschillende afbeeldingsapparatuur en afbeeldingen van gezonde ogen en ogen met een aandoening. Meerdere oogaandoeningen werden bekeken, waaronder glaucoom, leeftijdsgebonden maculadegeneratie, centrale sereuze retinopathie en retinitis pigmentosa. Automatisch verkregen resultaten werden vergeleken met handmatige annotaties van artsen. Er werd een goede overeenkomst tussen de twee segmentaties gevonden voor alle data sets, met een gemiddeld absoluut verschil dat meestal tussen de 3 en 8 μm was en nooit meer bedroeg dan 13 μm.

Alles overziend bieden de ontwikkelde methoden een flexibele, robuuste en nauwkeurige oplossing voor de segmentatie van lagen in zowel de binnenzijde als de buitenzijde van het nervlies en van laesies in gezonde en aangedane ogen. Deze technieken hebben de potentie voor klinische toepassingen en kunnen eenvoudig worden gebruikt om verschillende eigenschappen van retinale lagen te bepalen, die vervolgens gebruikt kunnen worden voor diagnose, prognose en opvolging van oogaandoeningen.

List of Publications

Journal papers

1. **J. Novosel**, S. Yzer, K. A. Vermeer and L. J. van Vliet, *Segmentation of locally varying numbers of outer retinal layers in OCT images*, IEEE Transactions on Medical Imaging, accepted (2017).

2. **J. Novosel**, K. A. Vermeer, Z. Wang, J. H. de Jong and L. J. van Vliet, *Joint segmentation of retinal layers and lesions in 3D OCT data of topologically disrupted retinas*, IEEE Transactions on Medical Imaging, accepted (2017).

3. **J. Novosel**, G. Thepass, H. G. Lemij, J. F. de Boer, K. A. Vermeer and Lucas J. van Vliet, *Loosely coupled level sets for simultaneous 3D retinal layer segmentation in optical coherence tomography*, Medical Image Analysis **26**, 1 (2015).

Conference papers

1. **J. Novosel**, Z. Wang, H. de Jong, M. van Velthoven, K. A. Vermeer and L. J. van Vliet, *Locally-adaptive loosely-coupled level sets for retinal layer and fluid segmentation in subjects with central serous retinopathy*, 2016 IEEE 13th International Symposium on Biomedical Imaging (ISBI), (2016).

2. **J. Novosel**, Z. Wang, H. de Jong, K. A. Vermeer, L. J. van Vliet, *Loosely coupled level sets for retinal layers and drusen segmentation in subjects with dry age-related macular degeneration*, Proceedings of SPIE **9784**, (2016).

3. **J. Novosel**, K. A. Vermeer, L. Pierrache, C. Klaver, L. van den Born, L. J. van Vliet *Method for segmentation of the layers in the outer retina*, 2015 37th Annual International Conference of the IEEE Engineering in Medicine and Biology Society (EMBC), (2015).

4. **J. Novosel**, K. A. Vermeer, G. Thepass, H. G. Lemij and L. J. van Vliet, *Loosely coupled level sets for retinal layer segmentation in optical coherence tomography*, 2013 IEEE 10th International Symposium on Biomedical Imaging, (2013).

Acknowledgements

Pursuing a PhD is a painful, enjoyable and challenging experience. It can be compared with climbing a mountain. Although it is accompanied with frustration, bitterness and hardships, once you reach the top, the view is amazing. For me, the whole process was truly a life-changing experience, which could not have been possible without the help that I received from many people. Here, I would like to give my thanks to all of them.

First and foremost, I would like to give a very big thank you to my daily supervisor dr. **Koen A. Vermeer**. It has been my honor to be among your first PhD students. I appreciate all your contributions of time and ideas to make my PhD experience productive. I am also thankful for all the patience you had teaching me and explaining concepts in many different manners. Your process of picking holes in my work has taught me to think from different perspectives and consequently made me a better researcher.

Another very big thanks, goes to my promotor prof. dr. **Lucas J. van Vliet**, for all his support and guidance over the past four years. Our weekly meetings and discussions always left me filled with new ideas and encouraged me to continue working on my PhD, even during the most difficult times.

Many thanks to **Netty** for all her help with my working permit and my position in ROI. I also thank **Jetty** and **Aletta** in ROI and **Mandy** and **Annellis** in TU Delft for assisting me in many different ways and handling the paperwork. **Ronald**, thanks for all the tech support.

I also want to thank all the medical doctors and ophthalmologists with whom I had the pleasure to work. **Gijs**, thank you for you patience to answer all my silly (and sometime basic) eye-related questions. **Henk**, **Laurance** and **Suzanne**, thank you for taking the time from your schedule to do manual segmentations. **Hans** and **Mirjam**, thanks for your medical expertise and providing me with the necessary data.

Kedir and **Babak**, it has been my pleasure knowing you. Many thanks for all the coffee breaks where we complained about the world. I also thank **Jeroen** for having the tolerance to listen to my non-stop talking. Many thanks to **Boy**, **Kari**, **Mathi**, **Max**, **Susan**, **Stijn**, and **Verena** for making our ARVO conferences fun.

Aline, **Annemiek**, **Caroline**, **Esma**, **Johannes**, **Mia**, **Marja**, **Olympia**, **Robin**, **Rene**, **Sonia**, and **Wout** thanks for making my experience in ROI enjoyable.

To housemates and regular guest of the building 22 in TU Delft, I had lots of fun during our nights out, coffee breaks and holidays dinners. Thank you **Alex**, **Anna**, **Dirk**, **Ganesh**, **Gyllion**, **Jelle**, **Jeroen**, **Jianfei**, **Joor**, **Juan**, **Lena Lennard**, **Marco**, **Milos**, **Mojtaba**, **Nadya**, **Qiaole**, both **Robert**, **Robiel**, **Richard**, **Tian** and **Tom**. To anyone else I should have thanked, thank you.

And last, but by no means least...
I want to thank my friends and family in Croatia, with a special thanks that goes to my parents, **Radoslava** and **Stjepan**, without whom this would not be possible. And to **Bruno**, thanks for doing this journey with me.

About the author

Jelena Novosel was born on June 28, 1987 in Zagreb, Croatia. From 2007 to 2009 she studied Electrical Engineering and Information Technology at University of Zagreb and obtained her Bachelor of Science (BSc) degree. Immediately after, she started her Master of Science (MSc) studies in Information and Communication Technology at the same university. During her MSc studies she gained an interest in image analysis. Her MSc thesis focused on a computer vision system for traffic speed enforcement and resulted in her MSc degree in 2011. In January 2012, she started her PhD. She was involved in a joint project between Delft University of Technology and Rotterdam Ophthalmic Hospital. Her research was in the field of ophthalmic image analysis and mainly focused on retinal layer segmentation, of which the most important findings are presented in this thesis.